UPC CTTC

Filtering in the Numerical Simulation of Turbulent Compressible Flow with Symmetry Preserving Discretizations

Centre Tecnològic de Transferència de Calor
Departament de Màquines i Motors Tèrmics
Universitat Politècnica de Catalunya

Aleix Báez Vidal
Doctoral Thesis

Filtering in the Numerical Simulation of Turbulent Compressible Flow with Symmetry Preserving Discretizations

Aleix Báez Vidal

TESI DOCTORAL

presentada al

Departament de Màquines i Motors Tèrmics
ESEIAAT
Universitat Politècnica de Catalunya

per a l'obtenció del grau de
Doctor per la Universitat Politècnica de Catalunya

Terrassa, December 2018

Filtering in the Numerical Simulation of Turbulent Compressible Flow with Symmetry Preserving Discretizations

Aleix Báez Vidal

Directors de la Tesi

Dr. Carlos David Pérez-Segarra

Dr. Assensi Oliva Llena

This thesis is dedicated to

my beloved, Laura,

my daughters, Valentina and Melissa Ghaia,

my daughters and sons to come,

the rest of my family, Maria, Nando and Mercè.

When God began to create heaven and earth, the earth being unformed and void,
with darkness over the surface of the deep and a wind from God sweeping over the water.
God said, "Let there be light"; and there was light.
God saw that the light was good, and God separated the light from the darkness.
God called the light Day, and the darkness He called Night.
And there was evening and there was morning, a first day.

God said, "Let there be an expanse in the midst of the water,
that it may separate water from water".
God made the expanse, and it separated the water which was below the expanse
from the water which was above the expanse.
And it was so. God called the expanse Sky.
And there was evening and there was morning, a second day.

Bereshit 1: 1-8

Acknowledgements

I want to express my most sincere gratitude to all the people who has contributed to the development of this thesis. Overall, it has been a long period in which times of deep concentration and progress have alternated with others in which my main occupation has been far of the thesis development. Now, looking backwards, it seems to me that the time I dedicated to lectures, to project proposals and to analyse the most variate fluid dynamics, programming and even personal challenges that have come to our research group has also helped me in the matturing process that a doctoral thesis is dedicated to. And thus, I hope that all these variate experiences will appear to the reader as a smoother writing style and a broader point of view.

So here is the personal acknowledgement to the individuals who have contributed to this complete learning and research process:

Prof. Carles David Pérez-Segarra co-director of the *Heat and Mass Transfer Technological Center* (CTTC), for depositing his trust on me as a PhD candidate, for the help along these years and for his enthusiasm for everything related to fluid mechanics. I also want to thank him for letting me focalise my work on the fields that I like the most and for giving me the freedom to decide the steps to take in most occasions.

Prof. Assensi Oliva, head of *Heat and Mass Transfer Technological Center* (CTTC) for taking me to foster in his reseach group and providing me with proper working facilities, for giving me the opportunity to be the responsible of a full Bachelor course subject and for asking and listening to my opinion in the different projects I have collaborated. Finally, I would also like to acknowledge his decisive role in keeping a general good ambient in the research center. Through these years many colleagues have come and gone, some more satisfied than the others, but in my opinion the general ambient in our everyday working place is pleasant when not enjoyable.

Dr. Xavi Trias has been a reference and an example in terms of scientific thinking, hard working, compromise and excellence pursuit. His always difficult to answer questions are the lever that turn a preliminary intuition into a well fundamented reasonement that can become an article in a scientific journal. I appreciate his good will to dedicate his attention, his everlasting patience, his profound knowledge on CFD, his supperior intelligence when dealing with all kind of problems and, in summary, some of his time, to help me along these last years.

Professors Roel Verstappen and Arthur Veldman welcomed me in their institute

in Groningen. Their ideas in treating turbulent flow are of capital influence in all the work I have done during these years. I would say that any of us would think of numerical discretisation of turbulent flow if it wasn't for their outstanding published scientific work. Later, Wybe Rozema, whom I met in Groningen when he was finishing his thesis in the late 2013, showed me his amazing developments before they were published. To me, his ideas and analysis are a turning poing in the numerical simulations of compressible flow. Dr. Rozema has developped the first rigoriously deduced scheme in this area.

My family, whom this work is dedicated to, for their patience and love despite my dry character. They have kept me happy under any circumstance.

My friends, some of whom I think I have lost forever, for sharing exciting experiences with me and warmly welcoming me when I was happy and when I was too serious or empty of any will or energy. Boaz Vilallonga has been a reference in non-conformism and together we have transited the path from young to mature individuals. Pablo Amador and Javier Sánchez for being there whatever the distance between us, Jaime García-Vaquero for showing me the ways of kindness.

My friends and colleagues in the laboratory: Lluís Jofre, Guillermo Oyarzun, Joan López, Joan Farnós, Joan Calafell, Alireza Nazeri, Nina Morozova, Firas Dabbagh, Santiago Torras, Octavi Pavón, Jordi Chivas, Juan Pedro Baptista, and Pedro Galione; who have shared parts of this track with me and for helping me with the most varied issues of the thesis.

My community, ATID, and my peoples, both the israelites and the catalans, who help me remembering the true purpose of those who study.

The Grant *Formacíon de Profesorado Universitario* (FPI) by the spanish *Ministerio de Educación, Cultura y Deporte* and the Polytechnical University of Catalonia (UPC) for their financial support.

Termo Fluids S.L. fot the technological support and allowing me to use its software during the thesis period.

Abstract

The present thesis investigates how explicit filters can be useful in numerical simulations of turbulent, compressible flow with symmetry preserving discretizations. Such explicit filters provide stability to simulations with shocks, provide stability to low-dissipation schemes on smooth flows and are used as test filters in LES turbulence models such as the Variational Multi-Scale eddy viscosity model or regularization models. The present thesis is a step forward in four main aspects.

First, a comparative study of the Symmetry Preserving schemes for compressible flow is conducted. It shows that Rozema's scheme is more stable and accurate than the other schemes compiled from the literature. A slight modification on this scheme is presented and shown to be more stable and accurate in unstructured meshes, but lesser accurate and stable in uniform, structured meshes.

Second, a theoretical analysis of the properties of filters for CFD and their consequences on the derivation of the LES equations is conducted. The analysis shows how the diffusive properties of filters are necessary for the consistency of the model.

Third, a study of explicit filtering on discrete variables identifies the necessary constraints for the fulfillment of the discrete counterpart of the filter properties. It puts emphases on the different possibilities when requiring the filters to be diffusive. After it, a new family of filters has been derived and tested in newly developed tests that allow the independent study of each property.

And last, an algorithm to couple adaptive filtering with time integration is reported and tested on the 2D Isentropic Vortex and on the Taylor-Green vortex problem. Filtering is shown to enhance stability at the cost of locally adding diffusion. This saves the simulations from being diffusive everywhere. The resulting methodology is also shown to be potentially useful for shock-capturing purposes with the simulation of a shock-tube in a fully unstructured mesh.

Contents

1

Introduction

In this introductory chapter, we describe the situations in which the simulation of compressible flow has or has had a relevant role in science and engineering. Then, the physical characteristics of turbulent compressible flow are described. After that, the models in the literature that reproduce this kind of flow and their mathematical formulation are also described and briefly analysed. Then, the scope of this thesis, i.e., the range of low dissipation numerical simulations of compressible flow is set. Finally, the main objectives of the thesis are announced and the outline of the document presented.

1.1 Scientific and industrial relevance of the simulation of compressible flow

The understanding and management of fluid flow played a crucial role in technification of the human societies occurred in western countries between the mid 18th century and the late 20th century, marked by the substitution of hand production for machine production. The energy sources the new machines required were based, during all this period, in the energy transfer between fluids and solids.

So, alongside the industrial development, the study of fluid flow gained interest and achieved great success. Unfortunately, when the equations that describe the time evolution of fluids were finally derived, it turned out that analytical solutions can be found in a minimal range of cases and that finding approximate solutions with simplified models does not provide accurate enough solutions either.

But the technological development took place and, today, accurate predictions of the behaviour of fluids enable energy savings, reductions in CO_x and NO_x emissions, better meteorological predictions and the subsequent economic benefits, new industrial production methods, more long-lasting designs of machinery or structures af-

fected by fluid loads, noise pollution reduction, higher levels of comfort with HVAC, etc. Many of these fields of application enable to make the hypothesis that fluids are incompressible (i.e. $\nabla \cdot \boldsymbol{u} = 0$) or to simplify the variations in density by means of the Boussinesq hypothesis. This thesis is dedicated to applications in which such simplification does not apply. These are, mainly, in the aerospace, turbomachinery and thermal machines fields.

In these applications of turbulent flow, the usual situation in which a prediction of a flow is required reads: "Given a geometry, a set of boundary conditions and a set of initial conditions, obtain the pressure, velocity and temperature fields of the flow in a region as functions of time and space". Sometimes the time dependence is not required and the steady or statistically steady states of the fluid fields are sufficient for the technological purposes. The vast majority of these flows are at high Reynolds numbers and Mach numbers greater than 0.3.

Since the fundamental fluid dynamics principles of lift and drag generation are well understood since the early 20th centuries and the flows are usually at high Reynolds numbers, potential flow based modellings of compressible flow were developed and used extensively in the past due to their capacity to provide fast and accurate solutions at low computational cost. This is true as long as the potential flow hypothesis applies and the geometry is simple or can be divided into simple significant parts. These approaches combined with empirical data have played a fundamental role in the design of aircraft and turbomachines in the past, but the hypotheses in which they are based are too restrictive for the State of the Art. When this happens, only more advanced experiments or numerical simulations can shed light on the fluidic behaviour that R&D engineers aim to harness to improve their designs.

Experimentation has evolved with the development of more accurate measuring equipment and wind tunnels. For example, PIV allows measuring velocity fields. But in experimental tests it is not easy to reproduce the flow conditions in full-scale machinery, its accuracy is limited and experimental campaigns are slow and expensive. Thus, when investigating a broad landscape of designs, experimental techniques are still limited. Numerical simulation, on the other side, can provide accurate data of specific flow phenomena, can better reproduce operating conditions and can reduce, depending on the studied flow, response times and costs.

The numerical simulation of fluid phenomena, or Computational Fluid Dynamics (CFD), is now a mature technique with reliable methodologies that allow to simulate most of the relevant flows. But its capacity is very strongly dependent on the available computing capacity for a simulation and there is a trade-off between

committed computational resource and available accuracy. This limitation has been overcome along the years and the numerical simulation of fluid flow has had an enormous impact on the machines that we use nowadays. For example, CFD was crucial to understanding the nacelle-wing interference drag and this allowed to situate the nacelles under the wings of Boeing 737 and all the later turbofan airliners [1].

1.2 Physical and mathematical models of gas dynamics

In this thesis, it is assumed that the kinetic theory of gases is valid for the range of situations under study. The focus of the work is the evolution of the macroscopic properties of gases and, thus, the starting point is the set of equations describing the evolution of the fluid magnitudes in an Eulerian system, i.e., density ρ, velocity $\boldsymbol{u}$, pressure p, temperature T and, in case of chemical transport, the species mass fractions x_i. These set of equations are called are the Navier-Stokes Equations (NSE). No transport of chemical species is considered in this thesis and, thus, NSE read for a single substance (see. e.g. [2]):

$$\frac{\partial \rho}{\partial t} + \nabla \cdot (\rho \boldsymbol{u}) = 0\,, \tag{1.1}$$

$$\frac{\partial (\rho \boldsymbol{u})}{\partial t} + \nabla \cdot (\rho \boldsymbol{u} \otimes \boldsymbol{u}) = \nabla \cdot (-p\mathsf{I} + \sigma) + \rho \boldsymbol{f_m}\,, \tag{1.2}$$

$$\frac{\partial \rho E_t}{\partial t} + \nabla \cdot (\rho E_t \boldsymbol{u}) = \nabla \cdot (-p\boldsymbol{u} + \sigma \cdot \boldsymbol{u} + \boldsymbol{q}) + \rho \boldsymbol{f_m} \cdot \boldsymbol{u} + \dot{q}_v\,; \tag{1.3}$$

where $E = e + \frac{1}{2}|\boldsymbol{u}|^2$ and e is the internal energy.These equations should be used together with the set of the constitutive equations of the particular gas under study. For Newtonian, calorifically perfect ideal gases, they are the ideal gases law

$$\frac{p}{\rho} = R_g T\,, \tag{1.4}$$

with R_g the gas constant, the constitutive laws of Newtonian shear stress

$$\sigma_{ij} = 2\mu \left[\frac{1}{2} \left(\frac{\partial u_i}{\partial x_j} + \frac{\partial u_j}{\partial x_i} \right) - \frac{1}{3} \frac{\partial u_k}{\partial x_k} \delta_{ij} \right]\,, \tag{1.5}$$

where μ is the dynamic viscosity and in this work it is assumed to comply with Sutherland's Law

$$\mu = \mu_{ref} T^{2/3} \frac{1 + C}{T + C}\,, \tag{1.6}$$

Joule's law for internal energy for calorifically perfect substances

$$e = c_v T\,, \tag{1.7}$$

where c_v is the specific heat capacity at constant volume and e is internal energy, Fourier's law for thermal conduction

$$q_i = -\lambda \frac{\partial T}{\partial x_i}\,, \tag{1.8}$$

where λ is the thermal conductivity of the gas.

In equations (1.1-1.3) $\boldsymbol{f_m}$ and $\dot{q}_v$ are respectively a volumetric force and a volumetric heat source that depend on the case under study. The real numbers R_g, μ_{ref}, C, and λ are the physical properties of the gas under study.

Taking the characteristic flow velocity u^*, density ρ^*, length L^*, temperature $T^* = u^{*2}/(R_g \gamma M^{*2})$, with the characteristic Mach M, Reynolds Re and Prandtl Pr numbers based on them and using the specific heat ratio γ, dividing each variable by its characteristic magnitude, the set Eqs.(1.1-1.3) become the non-dimmensional set of NSE if they are used together with the proper set constitutive laws. They read:

$$p = \frac{\rho T}{\gamma M^2}\,, \tag{1.9}$$

$$\sigma_{ij} = \frac{2\mu}{Re}\left[\frac{1}{2}\left(\frac{\partial u_i}{\partial x_j} + \frac{\partial u_j}{\partial x_i}\right) - \frac{1}{3}\frac{\partial u_k}{\partial x_k}\delta_{ij}\right]\,, \tag{1.10}$$

$$\mu = T^{2/3}\frac{1+C}{T+C}\,, \tag{1.11}$$

$$e = \frac{T}{\gamma(\gamma-1)M^2}\,, \tag{1.12}$$

and

$$q_j = -\frac{\mu}{RePrM^2(\gamma-1)}\frac{\partial T}{\partial x_j}\,. \tag{1.13}$$

Furthermore, the heat sources and volumetric forces should also be scaled accordingly.

The NSE are a set of Partial Differential Equations (PDE) for which only a few analytical solutions of cases with simple initial and boundary conditions have been found. Engineers rely on approximations, experimentation, numerical modelling

and combinations of these. For general initial and boundary conditions, there is no proof of the existence and unicity of a solution of the system. For this reason, they are object of one of the 7 millennium problems of the Clay Institute of Mathematics in their incompressible flow and periodic or vanishing at infinity version. For now, the main tools to study the physics of fluids are experimentation and numerical simulation. This thesis is focused on the second.

1.2.1 Scales of motion, computational cost and the Kolmogorov length scale

Throughout this work, the concept "scale of motion" will be used several times. It is a widespread concept in CFD that, nonetheless, has a vague meaning. The most used meaning comes from the Fourier analysis of the evolution in time of a fluid property evaluated at a point. Decomposing such signal in a Fourier series, each time frequency is associated with a characteristic geometric mode whose wavelength verifies the flow boundary conditions. In the case of isotropic turbulence, these geometric modes become Fourier modes of a 3D cube [3]. In general geometries and boundary conditions, this definition of a scale of motion does not provide means to determine the shapes of the modes. A short description of scales of motion in continuous spaces is given next. (Another definition for discrete domains is provided in chapter 4).

Let

$$\mathcal{P} = \left\{ \phi(\boldsymbol{x}) : D \subset \mathbb{R}^n \mapsto \mathbb{R} \quad | \quad a\phi + b\frac{\partial \phi}{\partial x_n} = f \quad \forall \boldsymbol{x} \in \partial D \right\}$$

the space of real continuous functions of bounded variation defined on a D subdomain of $\mathbb{R}^n$ that verify some boundary condition. Let

$$\langle \phi | \psi \rangle = \int_D \phi \psi \, d\Omega \tag{1.14}$$

be the inner product of $\mathcal{P}$.

Let

$$\mathcal{G}_{\text{inf}} = \{G_1(\boldsymbol{x}),\, G_2(\boldsymbol{x}),\, G_3(\boldsymbol{x}),\, \ldots,\, G_n(\boldsymbol{x}),\, \ldots\}$$

a sequence of the eigenfunctions of ∇^2 in D with increasing positive eigenvalues. As a result of the spectral theorem, the functions G_n of $\mathcal{G}$ form an orthogonal basis. Thus, each ϕ can be represented as a unique series in the form

$$\phi(\boldsymbol{x}) = \sum_{j=1}^{\infty} \breve{\phi}_j G_j(\boldsymbol{x}),$$

where

$$\breve{\phi}_j = \int_D \phi(\boldsymbol{x}) G_j(\boldsymbol{x})\, d\Omega.$$

Moreover, each $G_j(\boldsymbol{x})$ is related with a combination of a characteristic length scale in each space direction, e.g. , in the case of a periodic flow in $\mathbb{R}^3$, one of them is $\exp(i(k_1 x + k_2 y + k_3 z))$.

To represent the physics of continuum mechanics it is not necessary to represent ϕ with all the modes of $\mathcal{G}_{\text{inf}}$ because, if

$$\breve{\phi}_j = \int_D \phi(\boldsymbol{x}) G_j(\boldsymbol{x})\, d\Omega$$

converges everywhere, then $\breve{\phi}_j$ vanishes faster than $1/j$ and the highest modes (or smallest scales) are negligible.

Then, only a finite subset $\mathcal{G}_N \subset \mathcal{G}_{\text{inf}}$ is necessary to represent the physics with enough detail. This reduces many problems of continuum mechanics to analyzing only a small number of the modes because, as the operators in these applications are linear, the modes do not interact between them and only those with the lowest eigenvalues have interest in engineering applications. This is not the case in fluid dynamics. The non-linear convective term in equation (1.2) causes interactions between the different scales of motion, i.e. small scales affect big scales and vice-versa. This requires determinating the highest N (i.e., the smallest flow scale) so that $\mathcal{G}_N$ is sufficient to properly represent the fluid flow. This number depends on the flow under study. In the case of incompressible isotropic turbulence ruled by the Navier-Stokes equations (1.1-1.3) the ratio between the largest η_{LC} and the smallest η_{Kol} scales of motion is given by (see [4])

$$\frac{\eta_{Kol}}{\eta_{LC}} \propto Re^{-3/4} \tag{1.15}$$

that can be applied to any flow region with approximately isotropic turbulence. This implies that the number of degrees of freedom (DOF) in a cubic domain with unitary side size is $N_{DOF} \propto (1/\eta_{Kol})^3 \propto Re^{9/4}$. Other relations between flow scales exist for boundary layers and shear layers (see, e.g., [2, 5]).

The constraints on the integration time steps in a simulation have not been considered so far because they are not a main part of the scope of this thesis. Nonetheless, they also have a major influence when analyzing the computing cost of a simulation. Large scales of motion are related to low frequency phenomena and are the most relevant in engineering applications. Meanwhile, small scales of motion are related to high frequency phenomena. To properly calculate the effects of large scales, the

simulations of fluid flow should span enough in time as to capture the unsteady phenomena under study or to contain a number of cycles of the lowest frequency scale in statistically steady flows. On the other side, as it has been already mentioned, flow scales affect one another and such simulations limit the time integration steps so that the smallest scales phenomena are also accurately captured. These criteria on overall integration time and allowable time steps are independent of any time discretization and determine the maximum physically allowable time integration step and the number of time integration steps in a simulation. The ratio between the characteristic time of η_{LC} and η_{Kol} in isotropic turbulence is (see [4])

$$\frac{\tau(\eta_{Kol})}{\tau(\eta_{LC})} \propto Re^{-1/2}. \tag{1.16}$$

Therefore the total number of time steps (TS) to simulate the evolution of isotropic turbulence in a cubic domain is $N_{TS} \propto 1/\tau(\eta_{Kol}) \propto Re^{1/2}$.

Thus, from a scales of motion only point of view, for a CFD simulation to be able to capture all the physics of a fluid flow, it is required that the grid is fine enough and the time integration steps are small enough to capture all the scales of motion at every point. Furthermore, the geometrical domain must be large enough to not interfere with the physics under study and the number of iterations must be large enough to allow to capture all the largest scale transient phenomena. The total amount of DOFs multiplied by the number of fluid properties involved in a simulation and the discrete differential operators defines the total number of variables to be stored in the volatile memory of a computing architecture. Then, each operation between these variables and the memory communications between computing units requires some computing time. Finally, all the operations for a single time step should be repeated each iteration until the final integration time is reached. In the end, the size of the grid and the number of time integration steps play a fundamental role in the overall computing time and computing cost (committed facilities, maintenance, personnel, electric energy, etc.), and is determinating in the economical, scientifical and technological viability of a simulation.

Considerations of this kind lead to the conclusion that simulations of most of the flows of interest in engineering are unfeasible if all the flow scales are to be well reproduced. This handicap is overcome by modelling or not taking into account some of the flow physics. This opens the door to simulations with a level of accuracy that allows the designers to make decisions. Next, an introduction to some of the most known models in use follows.

1.3 Simplified models of compressible flow

In many situations of interest in aeronautics, the Navier-Stokes can be simplified by neglecting or modelling some of their terms. To do it, the relative order of magnitude of the terms in the Navier-Stokes equations must be studied first.

Among the of the most common simplifications, one consist in neglecting the transitory term when the boundary conditions are steady or almost steady. Another consists in neglecting viscous terms when the flow Reynolds numbers are high in the bulk of the domain and the flow is irrotational in this region. Since the Reynolds number of many interesting flows is high and the boundary layers are attached, viscous effects can be neglected in the freestream region (i.e., the whole fluid domain except boundary layers and wakes).

1.3.1 Potential flow

At high Reynolds numbers, if the flow is attached to the solid surfaces, boundary layers are thin and their exact shapes and thicknesses affect the freestream flow as small perturbations. Furthermore, if the freestream flow is irrotational, the velocity vector can be assigned to be $\boldsymbol{u} = \nabla\phi$, where ϕ is the velocity potential. The NSE (1.1-1.3) for compressible flow can then be simplified into the Prandtl-Glauert equation

$$(1 - M_\infty)^2\phi_{xx} + \phi_{yy} + \phi_{zz} = 0, \tag{1.17}$$

where x is the main flow direction and M_∞ the unperturbed stream Mach number.

Unlike the Navier-Stokes equations, Eq.(1.17) is linear and thus the superposition principle applies. This property has been used to determine the properties of the flow around objects as linear combinations of ϕ solutions of Eq.(1.17) which, all together, verify the boundary conditions of the object under analysis.

This procedure has been computationally exploited by means of the panels methods [6] to calculate airplane aerodynamics in design stages since the 1960's. Such methods are computationally light and with actual desktop computers approximate solutions of the attached flow around aircraft can be obtained within the fractions of a second.

The panels methods can include boundary layers by passing velocity and pressure distributions on the body surfaces to boundary layer solver codes and then using the result to modify the apparent body geometry. They can also calculate the

shapes of aircraft wakes and resolve unsteady flow if the boundary movement characteristic speed is orders of magnitude lower than the flows. All this for both subsonic and supersonic flows.

But the assumptions underlying in the potential flow model do not allow to predict transonic situations, nor boundary layer separations, nor interferences due to wakes, nor the effects of detached eddies, nor accurate values of friction-caused drag forces [7]. Because of these reasons, more accurate models are required at the cost of more effort in the preparation and post-processing of the case as well as higher computational resources and longer computing time.

1.3.2 Reynolds Averaged Navier Stokes (RANS)

When the potential flow model does not hold because viscous or transonic effects become too relevant in the overall flow description, the Navier-Stokes equations (1.1-1.3) can be averaged in time, thus obtaining the Reynolds Averaged Navier Stokes (RANS) [8]:

$$\frac{\partial \bar{\rho}}{\partial t} + \nabla \cdot (\bar{\rho}\hat{\boldsymbol{u}}) = 0\,, \tag{1.18}$$

$$\frac{\partial \bar{\rho}\hat{\boldsymbol{u}}}{\partial t} + \nabla \cdot (\bar{\rho}\hat{\boldsymbol{u}} \otimes \hat{\boldsymbol{u}}) = \nabla \cdot (-\bar{p}\mathsf{I} + \bar{\sigma}) - \nabla \cdot \mathsf{Sg_s} + \bar{\rho}\hat{\boldsymbol{f}}_{\boldsymbol{m}}\,, \tag{1.19}$$

$$\frac{\partial \bar{\rho}\hat{E}_t}{\partial t} + \nabla \cdot \left(\bar{\rho}\hat{\boldsymbol{u}}\hat{E}_t\right) = \nabla \cdot (-\bar{p}\hat{\boldsymbol{u}} + \hat{\boldsymbol{u}} \cdot \bar{\sigma} + \bar{\boldsymbol{q}}) + \hat{\boldsymbol{u}} \cdot \nabla \cdot (\mathsf{Sg_s}) + \nabla \cdot \left(\boldsymbol{Sg_{ht}} + \boldsymbol{Sg_{diff}}\right) + \bar{\dot{q}}_v\,; \tag{1.20}$$

where

$$\bar{\phi} = \frac{1}{t_2 - t_1}\int_{t_1}^{t_2} \phi\, dt\,;$$

and

$$\hat{\bar{\phi}} = \frac{\overline{\phi\rho}}{\bar{\rho}}\,.$$

Defining the time perturbations of the fluid magnitudes

$$\phi' = \phi - \bar{\phi} \quad \Rightarrow \quad \bar{\phi}' = 0\,;$$

and

$$\phi'' = \phi - \hat{\bar{\phi}},$$

the ideal gas law in equations (1.18-1.20) becomes

$$\bar{p} = \bar{\rho}\left((\gamma-1)\hat{\tilde{E}}_t - \frac{1}{2}\hat{\tilde{\boldsymbol{u}}}\cdot\hat{\tilde{\boldsymbol{u}}} + k_t\right), \tag{1.21}$$

where

$$k_t = \frac{1}{2}\widehat{\overline{\boldsymbol{u}''\cdot\boldsymbol{u}''}} \tag{1.22}$$

is the turbulent kinetic energy: a non-simulated property whose evolution is part of each specific RANS model. Newton's stresses tensor is approximated with

$$\bar{\sigma_{ij}} \approx 2\hat{\tilde{\mu}}\left[\frac{1}{2}\left(\frac{\partial\hat{\tilde{u}}_i}{\partial x_j} + \frac{\partial\hat{\tilde{u}}_j}{\partial x_i}\right) - \frac{1}{3}\frac{\partial\hat{\tilde{u}}_k}{\partial x_k}\delta_{ij}\right], \tag{1.23}$$

and Fourier's heat flux vector is approximated with

$$\bar{q}_i \approx -\hat{\tilde{\lambda}}\frac{\partial\hat{\tilde{T}}}{\partial x_i}. \tag{1.24}$$

Moreover, the sub-grid stress tensor

$$\mathsf{Sg_s} = \overline{\rho\boldsymbol{u}''\otimes\boldsymbol{u}''}, \tag{1.25}$$

the sub-grid diffusion and turbulent transport

$$\boldsymbol{Sg_{diff}} = \overline{\sigma\boldsymbol{u}''} - \frac{1}{2}\overline{\rho\boldsymbol{u}''\cdot\boldsymbol{u}''\otimes\boldsymbol{u}''} \tag{1.26}$$

and also the sub-grid heat transfer vector

$$\boldsymbol{Sg_{ht}} = c_p\overline{\rho T''\boldsymbol{u}''} \tag{1.27}$$

should be modelled.

There is a huge variety of models for k_t, $\mathsf{Sg_s}$, $\boldsymbol{Sg_{diff}}$ and $\boldsymbol{Sg_{ht}}$ in the literature (see, for example [8]). These models are implemented in CFD codes and have allowed to improve the designs of numerous devices operating with fluids: be it by making conclusions out of numerical simulations as in the cases reported in [9], or combined with optimization codes like in [10]. RANS models have performed accurately when simulating a broad range of flows. For example, Naseri et. al. predicted with reasonable accuracy the instability point and the performance of an axial transonic compressor [11]. For this reason, and also because they lay in the range of computationally affordable models, they have become the main CFD model in the

industry.

RANS models were originally developed to simulate flows where the scales of fluid motion consist on a big steady scale and relatively much smaller unsteady scales, i.e., turbulent scales. In this situation the transient term of the equations (1.18-1.20) should vanish. Nonetheless, transient terms are kept in the equations to allow the smooth evolution, from an initial guess to the steady state result, of the simulated fluid magnitudes. This technique is called time marching. With it, the intermediate solutions between the initial guess and the final steady state do not represent, in any sense, the transient evolution that would happen in an equivalent experiment.

Later, RANS models were also used to study transient flows consisting of a very large, slow unsteady flow motion scale and the much smaller turbulent scales in the so-called Unsteady Reynolds Averaged Navier Stokes (URANS) model. This approach splits the transient terms of equations 1.18-1.20) in two terms: one approaches the actual transient term of the variables and the other is used for time marching.

Time filtering of fluid properties inherent of RANS and URANS enables the use of implicit time integration schemes. This reduces the necessary time integration iterations to reach a solution and allows for shorter computing time and lesser computational resource. Thus, RANS and URANS are reasonably affordable in terms of response time and economical cost. But time filtering also limits the capacity of these methodologies to accurately simulate the interactions of flow motion scales. Flows composed of flow scales in two very separated size ranges, i.e., some large steady or long-period unsteady scales of motion and a range of much smaller small scales limited in near-wall regions, this is not a major drawback if there is no interest in the specific evolution of the small scales. On the contrary, when simulating flows where there is no such separation between two ranges of present flow scales or when reproducing the interactions between small, intermediate and large motion scales is necessary to capture the main behavior of the flow, using RANS or URANS is very questionable. Among the phenomena that time-filtering is inaccurate it is worth mentioning transitions of boundary layers, finding the stall angle of airfoils, flows driven by detached turbulence like the lift coefficient of an airfoil in stall, Rayleigh-Bénard convection at high Péclet numbers, etc. For such cases, using RANS or URANS provides unreliable solutions that may lead to inaccurate design decisions and undermine the credibility of CFD.

1.3.3 Large Eddy Simulations (LES)

The theoretical foundation of Large Eddy Simulations is the spatial filtering of the Navier-Stokes equations, which is in turn an implicit filtering in time as the smallest scales of motions are not simulated and only their average effect on the bigger scales is considered at each time step. Defining the spatial filter as

$$\hat{\phi}(\boldsymbol{x}) = \int_{\Omega} K_G(\boldsymbol{x}, \boldsymbol{\xi}) \phi(\boldsymbol{\xi})\, d\boldsymbol{\xi}, \tag{1.28}$$

then

$$\phi = \hat{\phi} + \phi' .$$

If filtering commutes with the differential operators, LES equations of mass and momentum conservation are straightforward while the derivation of the energy equation with the ideal gas law (1.34) is not. Altogether, the LES equations read (see [12])

$$\frac{\partial \hat{\rho}}{\partial t} + \nabla \cdot (\hat{\rho} \hat{\boldsymbol{u}}) = 0\,, \tag{1.29}$$

$$\frac{\partial \hat{\rho} \hat{\boldsymbol{u}}}{\partial t} + \nabla \cdot (\hat{\rho} \hat{\boldsymbol{u}} \otimes \hat{\boldsymbol{u}}) = \nabla \cdot (-\hat{p}\mathsf{I} + \hat{\sigma}) - \nabla \cdot \mathsf{Sg_s} + \hat{\rho} \hat{\boldsymbol{f}}_{\boldsymbol{m}}\,, \tag{1.30}$$

$$\frac{\partial \hat{\rho} \hat{E}_t}{\partial t} + \nabla \cdot \left(\hat{\rho} \hat{\boldsymbol{u}} \hat{E}_t \right) = \nabla \cdot (-\hat{p} \hat{\boldsymbol{u}} + \hat{\boldsymbol{u}} \cdot \hat{\sigma} + \hat{\boldsymbol{q}}) + \hat{\boldsymbol{u}} \cdot \nabla \cdot \mathsf{Sg_s} + S_p + S_e + S_d + \hat{q}_v\,; \tag{1.31}$$

where

$$\phi' = \phi - \hat{\phi} \quad \Rightarrow \quad \hat{\phi}' = 0 \tag{1.32}$$

and

$$\hat{\phi} = \frac{\widehat{\phi \rho}}{\hat{\rho}}\,. \tag{1.33}$$

In equations (1.29-1.31) the ideal gas law is

$$\hat{p} = \hat{\rho} \left((\gamma - 1) \hat{E}_t - \frac{1}{2} \hat{\boldsymbol{u}} \cdot \hat{\boldsymbol{u}} \right)\,, \tag{1.34}$$

the Newton's stress tensor is approximated with

$$\hat{\sigma_{ij}} \approx 2\hat{\mu} \left[\frac{1}{2} \left(\frac{\partial \hat{u}_i}{\partial x_j} + \frac{\partial \hat{u}_j}{\partial x_i} \right) - \frac{1}{3} \frac{\partial \hat{u_k}}{\partial x_k} \delta_{ij} \right] \tag{1.35}$$

and Fourier's heat flux vector is approximated with

$$\hat{q}_i \approx -\hat{\lambda} \frac{\partial \hat{T}}{\partial x_i}\,. \tag{1.36}$$

Moreover, the sub-grid stress tensor

$$\mathsf{Sg_s} = \widehat{\rho \boldsymbol{u} \otimes \boldsymbol{u}} - \frac{\widehat{\rho \boldsymbol{u}} \otimes \widehat{\rho \boldsymbol{u}}}{\hat{\rho}} = \hat{\rho} \left(\widehat{\overline{\boldsymbol{u} \otimes \boldsymbol{u}}} - \hat{\tilde{\boldsymbol{u}}} \otimes \hat{\tilde{\boldsymbol{u}}} \right) , \tag{1.37}$$

the pressure-dilatation term

$$S_p = \widehat{p \nabla \cdot \boldsymbol{u}} - \hat{p} \nabla \cdot \hat{\tilde{\boldsymbol{u}}} , \tag{1.38}$$

the sub-grid internal energy-velocity sub-grid term

$$S_e = \nabla \cdot \left(\widehat{\rho \boldsymbol{u} E_t} - \frac{\rho \widehat{\boldsymbol{u} \otimes \boldsymbol{u} \cdot \boldsymbol{u}}}{2} \right) - \nabla \cdot \left(\hat{\rho} \hat{\tilde{\boldsymbol{u}}} \hat{\tilde{E}}_t - \frac{\hat{\rho} \hat{\tilde{\boldsymbol{u}}} \otimes \hat{\tilde{\boldsymbol{u}}} \cdot \hat{\tilde{\boldsymbol{u}}}}{2} \right) \tag{1.39}$$

and the sub-grid turbulent dissipation rate

$$S_d = \widehat{\sigma : \nabla \boldsymbol{u}} - \hat{\sigma} : \nabla \hat{\tilde{\boldsymbol{u}}} \tag{1.40}$$

should be modelled.

LES allows to capture the large and part of the inertial (intermediate) scales of motion while the smallest turbulent scales are modelled after assuming they are almost independent of the largest. This allows to assume that their behaviour is statistically identical for all turbulent flows with the same constitutive equations and does not depend on the specific boundary and initial conditions. This allows to use coarser spatial discretizations and consequently larger time integration steps in areas where turbulence is reasonably isotropic.

In LES, explicit time integration schemes are of most common use because the time step restrictions inherent of these methodologies is not much more limiting than the physical maximum allowed time integration steps. With explicit time integration, for a given space discretization, the relationship between the maximum allowable time integration step Δt and the grid size Δx at each element of the geometrical discretization scales is

$$\Delta t \propto \frac{\Delta x}{u^*} \frac{M}{1 + M} , \tag{1.41}$$

where M is the local Mach number and u^* the flow-characteristic speed. Therefore, the maximum time integration step is restricted by the minimum sized element in the domain. But the models for the sub-grid terms of LES are derived for isotropic turbulence and zones with strongly anisotropic turbulence like boundary and shear layers must be resolved with almost full grid resolution. Henceforth, the smallest

elements that determine the overall maximum allowed time steps are in these relatively small regions. In LES, most grid points are near the boundary and shear layers. Since the grid spacing in these regions can not be coarsened, the overall computing costs of LES are significantly higher than those of RANS and URANS in many relevant situations (e.g. [13, 14]).

1.4 Discretizations of the Navier Stokes equations for compressible flow

Once the set of equations describing the evolution of the properties of a compressible flow is set, the methodology to simulate it with computers consists in establishing a finite set of real numbers that will represent, up to some degree of accuracy, the evolution of the fluid magnitudes in some physical domain.

First, a discretization methodology is chosen. The most known discretization methodologies are Finite Differences, Finite Elements, Finite Volumes (FV), Spectral Methods and the Discontinuous Galerkin Method. They all can be applied to any set of partial differential equations and have relative advantages and inconveniences [15]. In CFD, FV methods have gained popularity because the telescopic property inherent in their formulation ensures local and global conservation of mass, momentum and energy in all the regions of the fluid domain. Respecting conservation may not be so necessary in other fields of application like structural analysis, where other methodologies with higher local accuracy are preferred. There, the ruling equations do not need to be integrated with as much time integration steps as those necessary for the NSE. Therefore, the cumulative error committed due to non-conservation at each iteration is relatively less significant.

Next, a set of functions

$$\mathcal{N} = \{N_1(\boldsymbol{x}),\, N_2(\boldsymbol{x}),\, N_3(\boldsymbol{x}), \ldots, N_p(\boldsymbol{x})\}$$

defined in the spatial coordinates $D \subset \mathbb{R}^n$ is chosen for the representation of

$$\phi(\boldsymbol{x}) \simeq \sum_{i=1}^{p} \phi_i N_i(\boldsymbol{x})\,.$$

Hence, each fluid magnitude $\phi(\boldsymbol{x})$ is represented by the array

$$\boldsymbol{\phi} = \{\phi_1,\, \phi_2,\, \phi_3,\, \ldots \phi_n\} \in \Re^p$$

and $\mathcal{N}$ is the basis of the vector space on which the fluid variables will be represented. The basis of functions $\mathcal{N}$ is chosen in agreement with the discretization methodology. For example, in FV methods, $\mathcal{N}$ consists of piece-wise constant functions, each one evaluating 0 in all D excepting for simply connected subdomains $\Omega_o \in D$, with $\bigcup_o \Omega_o = D$ and preferably $\langle N_o | N_p \rangle = 0$. Meanwhile, in Discontinuous Galerkin methods, $\mathcal{N}$ consists of polynomials that evaluate zero in most of the domain and evaluate non-zero only in simply connected subdomains Ω_o of D.

Another choice to be made is the set of properties that will be the primary variables in the calculations. The constitutive equations provide relations between all the fluid magnitudes in a flow. This allows to calculate most of them as functions of a subset of the set of all the magnitudes. The primary variables are those in this subset. Numerical simulations approximate the evolution in time of the primary variables, which are used as parameters to calculate the others. In the case of compressible fluid flow of ideal gases 5 independent variables allow to calculate all the rest. Considering the primary variables as functions of space and time, the others become functions of the primary variables and their dependence on space and time is obtained after the constitutive equations. In compressible flow, the most common set of primary variables is the so-called conservative variables, i.e. the vector that contains

$$\begin{pmatrix} \rho \\ \rho u^1 \\ \rho u^2 \\ \rho u^3 \\ \rho E_t \end{pmatrix}_o \tag{1.42}$$

for every DOF, identified with the subindex "o". For incompressible flow, the usual primary variables are

$$\begin{pmatrix} u^1 \\ u^2 \\ u^3 \\ T \end{pmatrix}_o \tag{1.43}$$

Then, one discretizes the spatial operators of the NSE, RANS or LES. It is in this stage of the discrete modelisation process when the properties of the chosen basis of functions $\mathcal{N}$ has a paramount effect. For example, when discretizing equation (1.30) an approximation og $\nabla \cdot (\hat{\rho}\hat{\boldsymbol{u}} \otimes \hat{\boldsymbol{u}})$ is required for each DOF. Table 1.4 summarizes the differential operators in the Navier-Stokes, RANS or LES equations in continuous and discrete spaces:

Table 1.1: Differential operators in the Navier-Stokes, RANS and LES equations.

Name	Analyitical Form	Discrete Form
Divergence	$\nabla\cdot$	M
Gradient	∇	G
Convection[a]	$\boldsymbol{u}\cdot\nabla$	$\mathsf{C}(\boldsymbol{u})$
Laplacian[a]	$\nabla\cdot\nabla$	L
Curl[a]	$\nabla\times$	Rot

a Isomorphism.

The following example illustrates the discretization of a divergence operator in FV. Consider a cell (i.e., the subdomain Ω_o where a $N_o(\boldsymbol{x}$ evaluates 1)). in order to approximate $\nabla\cdot\boldsymbol{u}$ in that cell using Gauss' theorem. Thus

$$(\nabla\cdot\boldsymbol{u})_o = \frac{1}{\Omega_o}\int_{\partial\Omega_o}\boldsymbol{u}\cdot\boldsymbol{n}\,\delta\sigma \simeq \mathsf{M}_o = \frac{1}{\Omega_o}\sum_{op}\boldsymbol{u}_{op}\cdot\boldsymbol{n}_{op}S_{op} \quad \forall p\in Nb_o$$

, where Nb_o is the set of Ω_p with a non-null sized interface with Ω_o. There is some freedom to chose how $\boldsymbol{u}_{op}$ is evaluated at each interface "op" between cells "o" and "p". In the literature there are approximations like

$$\begin{aligned}\boldsymbol{u}_{op} \simeq 1/2\left(\boldsymbol{u}_o + (\nabla\boldsymbol{u})_o\cdot(\boldsymbol{r}_{op}-\boldsymbol{r}_o) + \boldsymbol{u}_p + (\nabla\boldsymbol{u})_p\cdot(\boldsymbol{r}_{op}-\boldsymbol{r}_p)\right) \simeq \\ \simeq 1/2\left(\boldsymbol{u}_o + (\mathsf{G}\boldsymbol{u})_o\cdot(\boldsymbol{r}_{op}-\boldsymbol{r}_o) + \boldsymbol{u}_p + (\mathsf{G}\boldsymbol{u})_p\cdot(\boldsymbol{r}_{op}-\boldsymbol{r}_p)\right)\end{aligned}$$

and

$$\boldsymbol{u}_{op} \simeq 1/2\left(\boldsymbol{u}_o + \boldsymbol{u}_p\right).$$

Notice that the first option requires G_o and G_p $\forall p \in Nb_o$. This increases the complexity of the discretization. A hierarchy of criteria to decide how the discretization of the equations should be undertaken is mandatory to construct discrete operators with predictable behaviour.

One of the causes of these misbehaviours when discretizing the differential operators is the non-prevalence of the product rule of differentiation in discrete spaces. E.g., while

$$\nabla\cdot(\rho\boldsymbol{u}) = \nabla\rho\cdot\boldsymbol{u} + \rho\nabla\cdot\boldsymbol{u} \quad \forall\boldsymbol{x}$$

the same is not true for discrete operators:

$$\mathsf{M}(\rho\boldsymbol{u})_o \neq \left(\mathsf{G}\rho\cdot\boldsymbol{u} + \rho\mathsf{M}\boldsymbol{u}\right)_o.$$

This implies that discretizations based on Gauss' theorem and the divergence operator do no respect the skew-symmetry of convection and that discretizations based on the convection operator are not necessarily fully conservative. The criteria used in this thesis follow the school of the Computational Mechanics and Numerical Mathematics (CMNM) at the Johann Bernoulli Institute for Mathematics and Computer Science and the Heat and Mass Transfer Technological Center that has been published in numerous scientific journal articles, e.g. [16–18]. Our approach consists in designing discrete operators for which the global properties of symmetry, skew-symmetry, conservation and normalization hold and, after these properties are ensured, focus on others like local accuracy. These concepts will be developed in chapters 2 and 3.

Finally, once the spatial operators are discretized, numerical schemes for Ordinary Differential Equations (ODEs) are used to get the relationship

$$\Psi(\boldsymbol{\phi}^{n+1}, \boldsymbol{\phi}^{n}, \boldsymbol{\phi}^{n-1}, \boldsymbol{\phi}^{n+1-q}) = 0,$$

where the superscript represents the time instant. After this is done, the system of ODEs is ready for coding and computing.

1.4.1 Classical characteristics analysis based discretisations

Classical mathematical analysis divides PDE systems into three main categories depending on the discriminant of the system if it is linear or the system's Jacobian when it is not [19]. The NSE for compressible belong, according to this criterion, in the hyperbolic-parabolic group. The hyperbolic part of the equations comes from the convective and pressure terms in equations (1.1, 1.2 and 1.3), while the parabolic part is in the diffusion terms in Eqs. (1.2 and 1.3). At high Reynolds and Péclet numbers, convection dominates over diffusion and the Navier Stokes equations can be seen as perturbed Euler equations. The perturbations are, in this approach, the diffusion terms. Since the Euler equations are hyperbolic, the discretization of the Navier Stokes equations for compressible flow is very often carried out adding diffusion terms to a characteristics-based discretization of the Euler equations (e.g. [20]).

This procedure starts writing the Euler part of the equations (1.1-1.3), or their LES or RANS equivalents in a divergence form

$$\frac{\partial}{\partial t}\boldsymbol{\phi} + \frac{\partial}{\partial x^j}\boldsymbol{f}^j = 0\,, \quad j \in [1,3]\,, \tag{1.44}$$

where $\boldsymbol{\phi}$ is an array with the primary variables and $\boldsymbol{f}^j$ is the array of fluxes of quan-

tities

$$\boldsymbol{\phi} = \begin{pmatrix} \rho \\ \rho u^1 \\ \rho u^2 \\ \rho u^3 \\ \rho E_t \end{pmatrix}, \qquad \boldsymbol{f}^j = \begin{pmatrix} \rho u^j \\ \rho u^1 u^j + p\delta^{1j} \\ \rho u^2 u^j + p\delta^{2j} \\ \rho u^3 u^j + p\delta^{3j} \\ \rho h_t u^j \end{pmatrix}. \tag{1.45}$$

Next, introducing the jacobian of the flux vector $\mathsf{J}(\boldsymbol{f}, \boldsymbol{\phi})$ with components $\frac{\partial f_p^j}{\partial \phi_q}$, one gets

$$\frac{\partial}{\partial t}\boldsymbol{\phi} + \frac{\partial \boldsymbol{f}^j}{\partial \phi_q}\frac{\partial \phi_q}{\partial x^j} = 0\,, \tag{1.46}$$

which can be diagonalized in a region if $n^j \frac{\partial f_p^j}{\partial \phi_q}$ has a complete set of eigenvectors for all $\boldsymbol{n} \in \mathbb{R}^3$. For a given $\boldsymbol{n}$,

$$\mathsf{J}_n(\boldsymbol{f}^j n^j, \boldsymbol{\phi}) = \mathsf{R}^{-1}\Lambda_{\mathsf{n}}\mathsf{R},$$

where Λ_{n} is a diagonal matrix. Thus one can study the projection of the system of equations (1.44) on $\boldsymbol{n}$ and the equations become uncoupled. The sth component then reads:

$$R_s^p \frac{\partial \phi_p}{\partial t} + R_s^p \frac{\partial f_p^j}{\partial \phi_q}\frac{\partial \phi_q}{\partial x_n} = \frac{\partial \psi_s}{\partial t} + \lambda_s \delta_{sq}\frac{\partial \psi_q}{\partial x_n} = 0, \tag{1.47}$$

where $\boldsymbol{\psi}$ are the so-called characteristic variables, x_n is the spatial coordinate in the $\boldsymbol{n}$ direction and δ_{ij} is Kronecker's delta.

Now, in a small domain around a point where Eq. (1.46) can be diagonalized, it follows from (1.47) that $\delta\psi_s = 0$ on $(x_n - \lambda_s t)$ or, in other words, ϕ_s is well approximated by

$$\psi_s(\boldsymbol{x}, t) \simeq \psi_s(\boldsymbol{x} - \lambda_s \Delta t \boldsymbol{n}, t - \Delta t);$$

i.e., a convection along x_n at λ_s velocity. Of course, the concepts "well approximated" and "small domain"are very vague here and, moreover, temporal variations of ψ_s are also affected by the information travelling in other directions. This very vague reasoning contains the main ideas behind the characteristics-based discretisations of the Euler equations.

To illustrate characteristics-based schemes we consider a 1D advection problem on a infinite spatial domain.

$$\frac{\partial \phi}{\partial t} + u\frac{\partial \phi}{\partial x} = 0 \tag{1.48}$$

$$\phi(x, t = 0) = \phi_0. \tag{1.49}$$

It is straightforward that

$$\phi(x,t) = \phi_0(x - \int_0^t u(\tau)\, d\tau, 0)$$

and ϕ is a wave travelling at u speed. The sign of u determines the direction in which the ϕ wave travels. Thus, in a numerical simulation, it seems obvious that the directionality of the information propagation should be respected. This is achieved by upwinding the numerical fluxes; i.e., using directionally-biased stencils for the approximations to the geometrical differential operators on ϕ (see, e.g. [21]). But upwinding causes undesired diffusion that smears the solutions of hyperbolic problems [22] and jeopardizes the capacity of numerical schemes to fulfill their ultimate goal, i.e., providing accurate predictions of fluid flow. High order upwind-biased numerical discretizations resolve this major drawback and allow to accurately simulate compressible flow at the cost of using larger stencils, i.e., increasing the computing cost.

1.4.2 Critique to the classical characteristics analysis

Among the motivations and influences that make researchers more prone to adopt one or another approach to their subject, some are not strictly related with the rational analysis of the scientific and technological challenges. Other social and individual factors related with ethics, finance, tradition and politics play a major role and strongly influence, not only the questions that researchers make, but also their predisposition to find positive and negative answers. These factors have a low impact in rationally pure disciplines like algebra, mathematical analysis or fundamental physics. But as a discipline becomes less fundamental and is closer to industrial applications, and as long as it combines more concepts, personal and social choices have a stronger effect on the scientific output.

CFD sits in between physics, mathematics, computing science and engineering. Moreover, it has a strong influence in the design of aircraft, vessels and a vast number of machines and devices. Thus, CFD is prone to be influenced by these elements and its development should not be analysed without considering them. This becomes apparent in the several accounts about how the fundamentals of CFD were established by different research groups ([23, 24]).

Regarding compressible flow, after the hyperbolic nature of the Euler equations and the characteristics, it seems that upwind biased schemes are the most extended methodologies to discretize the geometrical differential operators [25]. A good in-

troduction to them and other strategies to avoid the instability of numerical simulations for high speed flow (large Reynolds and Péclet numbers) can be found in [26]. It is remarkable that it is widely accepted in the litterature that central differentiation schemes do not add undesired artificial dissipation but, unfortunately, they are unstable and should be used together with some explicitly added dissipation mechanism (e.g. filtering). See, in this regard, the famous JST flux discretization [27]. This was also a common belief among the incompressible flow CFD community after the conclusions of classical authors like Patankar ([28]). But later investigations based on the properties of the operators of the NSE rather than on local approximations to derivatives or numerical fluxes showed that it is possible to build stable discretisations without any artificial dissipation or upwinding [16, 29]. These are the so-called Symmetry Preserving (SP) discretisations.

Several attempts to bring the good stability properties of SP schemes to compressible flow have been made. In his review article, Pirozzoli [26] mentions [30] and [31] as pioneers in energy-consistent schemes. Others have conducted similar works with more or less success (e.g. [32, 33]). However, as I see it, Rozema [34] established the first steps of a solidly founded discretization in this regard and the Groningen school took the lead in the theoretical study of flux discretisations.

Therefore, we now have compressible flow schemes that do not need any artificial dissipation, do not do any upwind and they are still stable when the flow is smooth (i.e. no shocks or strong discontinities), attaining the goals sought with characteristics-based upwind schemes without encompassing their drawbacks.

But the competition between the different CFD schools will never end. Many researchers have dedicated huge efforts and resources to high order and upwind-based methodologies. Now, with a very broad spectrum of discretizations to choose, the CFD researcher or user needs to identify the pros and cons of each of them to decide, on the most rational way, his/her best option.

Now it is time to go back to the reasons that hold characteristics-based high-order upwinding and check up to which degree they reproduce the nature of the flows. Here are some reasonable doubts:

- Characteristic-based high-order upwinding is derived from the advection equation, which is linear with respect to the transported magnitude. Convection in the NSE is non-linear.
- Most of the methodologies in characteristics-based high-order upwinding schemes are developed and checked in 1D Euler equations and extended to 2D and 3D

problems "straightforwardly". This is sometimes inconsistent (e.g. TVD in each dimension is not a sufficient condition for TVD in several dimmensions).

- The advantage of high-order methods over lower-order non-dissipative methods is often attributed to the reduction of aliasing error. However, the analysis that leads to this conclusion is the 1D advection at constant transport speed. This analysis has not been reproduced neither in higher dimensions spaces nor in non-linear convection. Consequently, there are no theoretical arguments that ensure that the advantage should hold under these conditions.
- High-order upwind schemes dissipate kinetic energy into internal energy in excess.
- The symmetry properties of the differential operators of the Euler equations can not be reproduced in discrete operators based on high-order upwinding.

Hence, overall, it seems that characteristics-based schemes are very well fit for linear or quasi-linear hyperbolic problems like high-velocity flows where smoothness and shock positions are more relatively important than the accurate prediction of detached turbulence and RANS is accurate. On the other side, for non quasi-linear problems that require LES or DNS, their advantages should now be reconsidered in front of SP schemes. This is the case of many of the applications of interest already described in section 1.1.

1.5 Objectives and Scope of the Thesis

This thesis is focused on the combination of Symmetry Preserving (SP) schemes for compressible flow with explicit filtering in order to eliminate wiggles and their induced instability. But doing this requires expanding the knowledge of the two elements to be combined. On one side, the existing SP schemes must be compared to identify which produce wiggles and to which extent they do. On the other, understanding of filtering in CFD has to be improved and the conclusions drawn brought to discrete filters. Finally, once the two elements are better understood, a combining methodology is described and tested. The thesis is structured in a way that each chapter can be read independently from the others or as a part of the overall work. Therefore, each of the chapters contains a more detailed introduction with a more specific scope and objectives.

To fulfill the goals, a comparison of the existing SP schemes is carried out in order to identify possible advantages of one scheme with respect to the others. This task

is reported in chapter 2. Later, before applying any filter, chapter 3 is a thorough study of the mathematical properties of the analytical filters in the CFD literature. An effort is made to summarize the defining properties of filtering and to identify mutually exclusive properties. This analysis is necessary in order to later determine which should be the criteria to design new discrete filters for CFD. To my surprise, I could not find similar published works. The theoretical work in chapter 3 is followed by another piece of text dedicated to explicit discrete filters for CFD in chapter 4. In it, I apply the findings of the previous chapter to define constraints for discrete explicit operators, to describe a new family of filters derived with these constraints and to define new tests that help assess them. After this is done, the derived filters are applied to SP discretizations of compressible flow in chapter 5. To finalize, chapter 6 summarizes and reviews the conclusions of the former.

The contents of this work will be useful to those who develop numerical methods for LES and to those who study the properties of LES equations. Meanwhile, those people who develop or use fast simulation tools in an industrial level will probably find the reasons and conclusions made here too far from their interest.

References

[1] A. Jameson. Computational Fluid Dynamics: Past, Present and Future, 2016.

[2] A. Liñán Martínez, M. Rodríguez Fernández, and F.J. Higuera Antón. *Mecánica de Fluidos (Primera Parte)*. Escuela Técnica Superior de Ingenieros Aeronáuticos, Madrid, 2005.

[3] P. Sagaut and R. Grohens. Discrete filters for large eddy simulation. *International Journal for Numerical Methods in Fluids*, 31(1997):1195–1220, 1999.

[4] A N Kolmogorov. The local structure of turbulence in incompressible viscous fluid for very large Reynolds numbers. *Proceedings of the Royal Society of London. Series A-Mathematical and Physical Sciences*, 434(1890):9–13, 1991.

[5] S. B. Pope. *Turbulent Flows*. Cambridge University Press, Cambridge, 2000.

[6] L. L. Erickson. Panel methods: An introduction. Technical report, NASA, 1990.

[7] J. Katz and A. Plotkin. *Low-speed aerodynamics*, volume 13. Cambridge university press, 2001.

[8] C. Rumsey. Langley Research Center Turbulence Modeling Resource. Implementing Turbulence Models into the Compressible RANS Equations.

https://turbmodels.larc.nasa.gov/implementrans.html, 2017. Accessed 01-10-2018.

[9] D Schwamborn, T Gerhold, and R Heinrich. The DLR tau-code: Recent applications in research and industry. *Proceedings on CD of the European Conference on Computational Fluid Dynamics ECCOMAS CDF 2006*, pages 1–25, 2006.

[10] Zhoujie Lyu and J. Martins. Aerodynamic shape optimization of a blended-wing-body aircraft. page 283, 2013.

[11] A. Naseri, M. Boroomand, and S. Sammak. Numerical investigation of effect of inlet swirl and total-pressure distortion on performance and stability of an axial transonic compressor. *Journal of Thermal Science*, 25(6):501–510, 2016.

[12] A.W. Vreman. *Direct and large-eddy simulation of the compressible turbulent mixing layer*. PhD thesis.

[13] N. Gourdain. Prediction of the unsteady turbulent flow in an axial compressor stage. Part 1: Comparison of unsteady RANS and LES with experiments. *Computers and Fluids*, 106:119–129, 2015.

[14] T. Léonard, L. Gicquel, N. Gourdain, and F. Duchaine. Steady/Unsteady Reynolds-Averaged Navier-Stokes and Large Eddy Simulations of a Turbine Blade at High Subsonic Outlet Mach Number. *Journal of Turbomachinery*, 137(4):041001, 2014.

[15] Jiyuan Tu, Guan-Heng Yeoh, and Chaoqun Liu. Chapter 4 - cfd techniques–the basics. In Jiyuan Tu, Guan-Heng Yeoh, and Chaoqun Liu, editors, *Computational Fluid Dynamics (Second Edition)*, pages 123 – 175. Butterworth-Heinemann, 2013.

[16] F. X. Trias, O. Lehmkuhl, A. Oliva, C. D. Pérez-Segarra, and R.W.C.P. Verstappen. Symmetry-preserving discretization of Navier-Stokes equations on collocated unstructured grids. *Journal of Computational Physics*, 258:246–267, 2014.

[17] L. Jofre, O. Lehmkuhl, J. Ventosa, F.X. Trias, and A. Oliva. Conservation properties of unstructured finite-volume mesh schemes for the navier-stokes equations. *Numerical Heat Transfer, Part B: Fundamentals*, 65(1):53–79, 2014.

[18] A. Báez Vidal, O. Lehmkuhl, F. X. Trias, and C. D. Pérez-Segarra. On the properties of discrete spatial filters for CFD. *Journal of Computational Physics*, 326:474–498, 2016.

[19] P.J. Olver. *Introduction to Partial Differential Equations*. Undergraduate Texts in Mathematics. Springer International Publishing, Berlin/Heidelberg, 2014.

[20] Chi-Wang Shu. Chapter 4: Essentially non-oscillatory and weighted essentially non-oscillatory schemes for hyperbolic conservation laws. *Advanced Numerical Approximation of Nonlinear Hyperbolic Equations*, 1697(97-65):325–432, 1998.

[21] B. Van Leer. Upwind and High-Resolution Methods for Compressible Flow : From Donor Cell to Residual-Distribution Schemes. *Communications in Computational Physics*, 1(2):192–206, 2006.

[22] R.J. LeVeque. Finite Volume Methods for Hyperbolic Problems. *Cambridge University Press*, 54:258, 2002.

[23] B. Van Leer. History of CFD part II, 2010.

[24] A. K. Runchal. Emergence of Computational Fluid Dynamics at Imperial College (1965-1975): A Personal Recollection. *Journal of Heat Transfer*, 135(1):011009, 2012.

[25] Robert H Nichols and Peter G Buning. User's manual for overflow 2.2. *University of Alabama and NASA Langley Research Center*, 2008.

[26] S. Pirozzoli. Numerical Methods for High-Speed Flows. *Annual Review of Fluid Mechanics*, 43:163–194, 2011.

[27] Antony Jameson, Wolfgang Schmidt, and Eli Turkel. Numerical solution of the euler equations by finite volume methods using runge kutta time stepping schemes. In *14th fluid and plasma dynamics conference*, page 1259, 1981.

[28] S. Patankar. *Numerical heat transfer and fluid flow*. CRC press (Taylor&Francis Group), New York, 1980.

[29] R. W. C. P. Verstappen and A. E. P. Veldman. Symmetry-preserving discretization of turbulent flow. *Journal of Computational Physics*, 187:343–368, 2003.

[30] W.J. Feireisen, W.C. Reynolds, and J.B. Ferziger. Numerical simulations of compressible homogeneous turbulent shear flows. *Report TF-13 (unpublished) Thesis, Stanford University*, 1981.

[31] G. A. Blaisdell, E. T. Spyropoulos, and J. H. Qin. The effect of the formulation of nonlinear terms on aliasing errors in spectral methods. *Applied Numerical Mathematics*, 21(3):207–219, 1996.

[32] A. Jameson. Formulation of kinetic energy preserving conservative schemes for gas dynamics and direct numerical simulation of one-dimensional viscous compressible flow in a shock tube using entropy and kinetic energy preserving schemes. *Journal of Scientific Computing*, 34:188–208, 2008.

[33] J. C. Kok. A high-order low-dispersion symmetry-preserving finite-volume method for compressible flow on curvilinear grids. *Journal of Computational Physics*, 228(18):6811–6832, 2009.

[34] W. Rozema. *Low-dissipation methods and models for the simulation of turbulent subsonic flow*. PhD thesis, University of Groningen, 2015.

2

Symmetry Preserving Discretizations of Compressible flow: a Comparison

2.1 Introduction

In the past, CFD simulations with centred schemes for the calculation of spatial derivatives or numerical fluxes have been considered unstable or oscillation generating by the researchers of numerical methods in both incompressible and compressible flow. The book by Patankar [1] for the simulations of incompressible flows, the pioneering work by Godunov [2] and the works by Harten, for example, [3], remark that, in order to grant stability, the numerical schemes used to compute derivatives or fluxes at interfaces should contain some degree of diffusion. Accordingly, diffusion was introduced using more or less elaborated upwind schemes. This theory was constructed on 1D hyperbolic equations and extended to 3D with structured meshes. As artificial diffusion reduces the accuracy of results, efforts were put to reduce it to the strictly necessary minimum. Examples of these approaches are the Lax-Wendroff scheme, ENO [3] and WENO [4] for compressible flows or QUICK [5] for incompressible flows.

Flow scales are eigenfunctions of the diffusion operators. As their eigenvalues are higher, smaller scales are more affected by artificial diffusion. This can also be seen

with Fourier analysis, whose function basis is precisely the set of eigenfunctions of the Laplacian operator in $\mathbb{R}^n$. Consequently, the addition of artificial diffusion was acceptable as long as the numerical simulations intended only to capture the features of the largest flow scales; i.e. as long as turbulence was modelled with Reynolds Averaged Navier Stokes (RANS). Later, due to the increase of computing capacity, transient LES and DNS have gradually become more affordable and widespread. These techniques can better predict fluid flows because more motion scales are resolved. On the other hand, artificial diffusion on small scales can distort them and their effect on larger flow scales, reducing the accuracy of the time-averaged variables. Henceforth, DNS and LES have questioned the existing upwind-biased spatial discretization schemes.

In Finite Volumes discretizations, research has led to the substitution of centered schemes where fluxes at interfaces between adjacent o and p cells are computed as

$$f_{o\,p} = \frac{f(\phi_o) + f(\phi_p)}{2} \tag{2.1}$$

and those in which variables were interpolated at interfaces to later calculate the flux funcions

$$f_{o\,p} = f(\phi_{op}(\boldsymbol{\phi})) \tag{2.2}$$

to the families of the Symmetry Preserving and Kinetic Energy Preserving schemes, where the numerical fluxes depend on neighbour cells and no interpolation of the fluid variables is required

$$f_{o\,p} = f(\phi_o, \phi_p) = f_{p\,o}\,. \tag{2.3}$$

Morinishi [6] developed equivalent methodologies for Finite Diferences discretizations. With these schemes and the imposition of some restrictions, artificial diffusion is not necessary anymore and velocities are bounded by some criterion other than monotonicity preservation.

Under incompressible flow assumptions, it seems that the first reference of this kind of scheme is due to Harlow and Welch [7], but the authors do not mention this property and, thus, do not identify the cause of the stability of their second-order scheme. Arakawa [8] showed the importance of respecting the analytical symmetries of the operators in their discrete approximation and developed schemes accordingly. Later, Morinishi et al. [6] proposed a high order KEP method and Finite Differences schemes in structured meshes. Verstappen and Veldman [9] extended the Symmetry Preserving method to 4th-order non-uniform structured staggered finite volumes aiming the conservation of kinetic energy. Perot provides a good account of this family of schemes up to 2011 in [10]. Later, KEP schemes have been adapted

to unsturctured meshes with both staggered and collocated formulations by Trias et al. [11]. Higher order symmetry preserving schemes for unstructured grids have not been reported. Even with low-order, it is commonly accepted nowadays that non dissipative schemes are the best choice to discretize NSE when simulating internal or external flows for DNS or LES [12].

After the success of SP schemes in incompressible flows, several researchers engaged in their extension to compressible flows. Feireisen [13] proposed an splitting of the convective derivatives in order to achieve a kinetic energy consistent method for compressible flows. Antony Jameson deduced a KEP scheme [14] and tested it on a 1-D Shock-tube problem, even though the shock-tube does not seem the most appropriate test for schemes designed for the prediction of turbulence. In his paper, Jameson stated that KEP schemes could be used for DNS simulations with shock waves provided that enough control volumes were used, thus requiring very large computer resources that can be expected in a relatively far future. In the Dutch school, Kok adapted the method of Verstappen and Veldman [9] to compressible flow getting a high-order, low-dispersion, SP scheme. However, this scheme requires additional filtering to avoid instabilities. Finally, Rozema et al. [15] performed an analysis based on a $\mathcal{L}_2^5$ norm from which they derived a scheme where convection preserves kinetic energy, mass, momentum, and the addition of mass and kinetic energy in a volume. They imposed a bound on the evolution of the variables that should be conserved. Therefore, perturbations are prevented from growing and simulations do not blow up. Still, a limitation in the $\mathcal{L}_\infty$ norm of fields does not imply that the solutions obtained with these schemes are physically admissible and bounded wiggles can appear with Rozema's scheme.

Meanwhile, the same family of schemes has also been derived by Kravchenko and Moin [16] and Ducros et al. [17] after identifying the necessity to use skew-symmetric convection operators for LES and DNS simulations in order to reduce aliasing errors in finite differences of finite volumes. The 2nd-order discretization in Ducros et al. [17] is, in fact, the JST scheme [18], for which the cause of its good performance was not fully understood at the time of its publication.

Symmetry preserving, kinetic energy preserving or skew-symmetric schemes belong to the Symmetry Preserving (SP) family of schemes and, abusing of language, we will call them all SP Schemes (SPS). Summarizing, SPS try to mimic the symmetry properties of their continuous counterparts and reduce aliasing errors that otherwise can affect the simulations results in a catastrophic manner. Both features seem solid enough in favor of SPS as to make them the default choice for DNS and LES simulations. If this has not already happened, it is probably because of the impossibility to

construct high-order schemes on unstructured meshes while keeping SP. The range of application of these schemes in compressible flows can be found in the 2011 review article of Pirozzoli [12]. Without entering into details, SP schemes should be used to model compressible flows when studying transient flows with a turbulent component. Shock-Boundary Layer Interactions are a typical example of application.

Once the SP theory established, numerical experimentation shows that incompressible SP schemes avoid the appearance of wiggles in a broader range of situations than compressible SP. The most notorious case is when using coarse grids. The reason for this lies on the fact that while incompressible methods imply the resolution of, at least, one Poisson equation for the calculation of pressure for every time step. Then, the velocity field is projected projection into a divergence-free space. Compressible methods do not and must not resolve any elliptic equation. This elliptic operation and the further velocity projection into a divergence-free space can be lumped into a single smoothing operator [11]

$$\boldsymbol{u}^{\boldsymbol{n+1}} = (\mathcal{I}_d + \frac{\Delta t}{\rho}\nabla(\nabla^2)^{-1}\nabla\cdot)\boldsymbol{u}^{\boldsymbol{p}} = \mathcal{P}\boldsymbol{u}^{\boldsymbol{p}}. \tag{2.4}$$

On the other hand, bounded amplitude wiggles persist in compressible SP methods if meshes are not refined enough or some action is taken. Hence, even though symmetry preserving schemes bound the $\mathcal{L}^2$ norm of velocities, wiggles can appear if a furtter condition bounding velocity variations, e.g., Total Variations Diminishing (TVD), is not imposed. As far as we know, there is not in the literature a condition in this sense that does not imply dissipation.

This chapter is dedicated to the comparison of existing explicit symmetry preserving schemes for compressible flow. These schemes are summarized in section 2.2. They are later compared on the 2D Isentropic Vortex problem in section 2.3 and on the Taylor-Green problem in section 2.4. The conclusions of the tests are reported in section 2.5.

2.2 Symmetry Preserving schemes for compressible flows

The Navier-Stokes equations for compressible flows have been introduced in Chapter 1. Here, we focus on Finite Volumes discretizations, i.e., the discretization basis is a set of piece-wise continuous distributions (see subsection 1.4) and assign their average value to each sub-domain. In the notation of this thesis, subscripts identify cells when alone and cells interfaces when in pairs and superscripts denote space dimensions. V_o stands for the volume of the o^{th} cell, S_{op} is the area of the interface

between cells o and p and $\boldsymbol{n_{op}}$ is the unit vector normal to the interface, pointing from o to p. The summation convention applies for subscripts and superscripts. Moreover, $\phi_\bullet = \{\phi_1, \phi_2, \ldots, \phi_p\}$ and $\mathcal{N} = \{N_1(\boldsymbol{x}), N_2(\boldsymbol{x}), N_3(\boldsymbol{x}), \ldots, N_p(\boldsymbol{x})\}$. With all this, let a discretization be defined by

$$\boldsymbol{x} \in D \in \mathbb{R}^n \;\Rightarrow\quad \phi(\boldsymbol{x}) \simeq \phi_i N_i(\boldsymbol{x}). \tag{2.5}$$

Then, a FV discretization is

$$D = \bigcup_o \Omega_o; \quad N_o(\boldsymbol{x}) = \begin{cases} 1 & \text{for} \quad \boldsymbol{x} \in \Omega_o \\ 0 & \text{for} \quad \boldsymbol{x} \notin \Omega_o \end{cases} \;;\quad \phi_o = \frac{1}{V_o}\int_{\Omega_o} \phi(\boldsymbol{x})\,\delta\Omega. \tag{2.6}$$

It is obvious to translate these rules into discretizations of $\mathbb{R}^1$ or $\mathbb{R}^2$.

A fundamental element that allows easy descriptions of properties in general disctretizations is the inner product

$$\langle \phi_\bullet | \psi_\bullet \rangle = \int_D \left(\phi_o N_o(\boldsymbol{x})\right)\left(\psi_p N_p(\boldsymbol{x})\right)\,\delta\boldsymbol{x}\,.$$

In FV, it reads

$$\langle \phi_\bullet | \psi_\bullet \rangle = \phi_o \Omega_o \psi_o\,.$$

then, following the Navier Stokes Equations (NSE) (1.1, 1.3, 1.3), when the domain is periodic numerical schemes should conserve

$$\begin{aligned} &\frac{d}{dt}\langle \rho_\bullet | 1_\bullet \rangle = 0 && \text{mass,} \\ &\frac{d}{dt}\langle \rho \boldsymbol{u}_\bullet | 1_\bullet \rangle = 0 && \text{momentum and} \\ &\frac{d}{dt}\langle (\rho E_t)_\bullet | 1_\bullet \rangle = 0 && \text{energy} \end{aligned} \tag{2.7}$$

in time. Furthermore, SP schemes do not generate nor destroy kinetic energy by convection. Recalling the Skew symmetry of convection in the analytic, continuous space,

$$\langle \phi | \mathsf{C}(\boldsymbol{u})\psi \rangle + \langle \mathsf{C}(\boldsymbol{u})\phi | \psi \rangle = 0\,. \tag{2.8}$$

This property holds for the discrete convective operators in NSE SP discretizations. It becomes

$$\langle \phi_\bullet | \mathsf{C}_\bullet(\boldsymbol{u}_\bullet)\psi_\bullet \rangle + \langle \mathsf{C}_\bullet(\boldsymbol{u}_\bullet)\phi_\bullet | \psi_\bullet \rangle = 0\,, \tag{2.9}$$

implying

$$\Omega_o \mathsf{C}_{op} = -\Omega_p \mathsf{C}_{po}\,. \tag{2.10}$$

The convection of momentum and kinetic energy result from the product of $\rho \boldsymbol{u} \otimes \boldsymbol{u} \cdot \boldsymbol{n}$, and 3 conservative magnitudes should be handled instead of the 2 in Eq. (2.8). This arises the question about how should $\rho \boldsymbol{u} \otimes \boldsymbol{u} \cdot \boldsymbol{n}$ be organized into the product of two quantities,e.g., $(\rho \boldsymbol{u}) \otimes (\boldsymbol{u}\boldsymbol{n})$ or $(\sqrt{\rho}\boldsymbol{u}) \otimes \sqrt{\rho}\boldsymbol{u}\boldsymbol{n})$?

The different approaches when distributing the kinetic energy product define how the magnitudes should be approximated at interfaces. Accordingly, several SPS come up. Those of 2nd order are summarized in Table 2.1, where JST refers to the classical [18] without the stabilizing additional viscosity, i.e., we consider only the base scheme without any shock capturing methodology. Furthermore, in Table 2.1 the schemes are written in the notation introduced in [19], which has been slighltly expanded and is summarized in equations (2.11).

$$\begin{aligned}
\bar{\phi}_{op} &= \frac{1}{2}(\phi_o + \phi_p) \\
\breve{\phi}_{op} &= \sqrt{\phi_o \phi_p} \\
\overline{\phi\psi}_{op} &= \frac{1}{2}(\phi_o \psi_o + \phi_p \psi_p) \\
\widetilde{\phi\psi}_{op} &= \frac{1}{2}(\phi_o \psi_p + \phi_p \psi_o)
\end{aligned} \tag{2.11}$$

Since the discretization of pressure gradients was not derived from any analysis in any of the schemes and the authors used second-order central discretizations to evaluate pressure at cell interfaces (see Table 2.1), we include in our analysis a modification of the RZM scheme in which the pressure was reconstructed with $\ddot{p}$, where

$$\ddot{\phi}_{o_{op}} = \phi_o + (\mathsf{G}\phi)_o \cdot (\boldsymbol{x_{op}} - \boldsymbol{x_o}) \,. \tag{2.12}$$

This last scheme is identified as Modified Rozema (MRZM).

2.3 2D Isentropic Vortex

The 2D isentropic vortex evolution case [21] tests the capabilities of discretization schemes in a convective flow without turbulence or shock waves. In $\mathbb{R}^2$, with perturbations vanishing at infinity, under ideal gas and Euler equations and following the parametrization of Spiegel et al. [22], the initial flow fields read:

Table 2.1: Table : KEP schemes for compressible flow in the literature.

Cons. Equation	Mass	Momentum		Energy
Flux	ρv^j	$\rho v^i v^j$	p	$\rho h_t v^j$
JST81 [18]	$\bar{\rho}\bar{v^j}$	$\overline{\rho v^i}\bar{v^j}$	$\overline{p}$	$\overline{\rho h_t}\bar{v^j}$
JKEP [14]	$\bar{\rho}\bar{v^j}$	$\bar{\rho}\bar{v^i}\bar{v^j}$	$\overline{p}$	$\bar{\rho}\bar{h_t}\bar{v^j}$
KOK [19]	$\overline{\rho v^j}$	$\overline{\rho v^j}\bar{v^i}$	$\overline{p}$	$\overline{\rho v^j}(\breve{u}+\frac{1}{2}\widetilde{v^k v^k})+\widetilde{pv^j}$
RZM [20]	$\breve{\rho}\bar{v^j}$	$\breve{\rho}\bar{v^i}\bar{v^j}$	$\overline{p}$	$(\breve{\rho}(\breve{u}+\frac{1}{2}\widetilde{v^k v^k})\bar{v^j})+\widetilde{pv^j}$
MRZM	$\breve{\rho}\bar{v^j}$	$\breve{\rho}\bar{v^i}\bar{v^j}$	$\bar{\bar{p}}$	$(\breve{\rho}(\breve{u}+\frac{1}{2}\widetilde{v^k v^k}))\bar{v^j}+\bar{\bar{p}}\bar{v^j}$

$$
\begin{aligned}
\boldsymbol{u} &= \boldsymbol{u}_\infty + \boldsymbol{\delta u}\,,\\
T &= T_\infty + \delta T\,,\\
p &= \rho^\gamma\,;
\end{aligned}
$$

where

$$
\begin{aligned}
\boldsymbol{\delta u} &= \Omega \left\{ \begin{array}{c} \eta \\ -\xi \end{array} \right\}\,,\\
\delta T &= -\frac{\gamma-1}{2}\Omega^2\,;
\end{aligned}
$$

and $\xi = (x-x_0)/R$; $\eta = (y-y_0)/R$; $\Omega = \beta\exp(-f)$; $f(x,y) = -\frac{1}{2\sigma^2}(\xi^2+\eta^2)$; $\beta = \frac{5}{2\pi\sqrt{\gamma}}\exp\frac{1}{2}$; $\sigma = 1$.

The numerical values of the parameters are also the same as Spiegel et al. [22], i.e., $R=1$; $\sigma=1$; $T_\infty=1$; $p_\infty=1$; $\rho_\infty=1$; $\gamma=1.4$ and $R_{gas}=1$.

Errors from all sources (truncation errors, artificial diffusion, dispersion) can pile up at long time integration times and the initial characteristics of the vortex are lost and eventually simulations can blow-up. Spiegel et al. [22] studied different versions of this case reported in the literature and provided recommendations to avoid boundary-induced blow-up. Specifically, they suggest to set the spatial domain to $D = \{(x,y) \in [-10R, 10R] \times [-10R, 10R]\}$ and to use characteristic non-reflecting boundary conditions for $\boldsymbol{u}_\infty = \boldsymbol{0}$, and periodic boundary conditions in the convection direction only if $\boldsymbol{u}_\infty \neq \boldsymbol{0}$. This way, perturbations can leave the simulation domain through the non-reflecting boundary conditions.

Table 2.2: Table : Meshes for the 2D Isentropic Vortex case.

Mesh	L	N_{side}	N_{tot}
str80	10	80	6400
str200	10	200	40000
unstr80	10	80	14620
unstr200	10	200	58330

Following these recommendations, we compare the discretizations in section 2.2 on uniform structured and unstructured meshes. The studied uniform Cartesian meshes have 80 and 200 divisions in each direction respectively. The corresponding unstructured meshes are made of triangles with the same size of the structured counterparts. Thus, 4 different meshes are defined (see Table 2.2). The simulations were discretized in time using the 3-steps explicit Runge-Kutta scheme in Gottlieb and Shu [23]:

$$\begin{aligned}
\phi_o^{n(+1)} &= \phi_o^n + \Delta t \mathsf{R}_o(\phi_\bullet^n) \\
\phi_o^{n(+2)} &= \frac{3}{4}\phi_o^n + \frac{1}{4}\phi_o^{n(+1)} + \frac{1}{4}\Delta t \mathsf{R}_o(\phi_\bullet^{n(+1)}) \\
\phi_o^{n(+3)} &= \frac{1}{3}\phi_o^n + \frac{2}{3}\phi_o^{n(+2)} + \frac{2}{3}\Delta t \mathsf{R}_o(\phi_\bullet^{n(+2)}) \\
\phi_o^{n+1} &= \phi_o^{n(+3)},
\end{aligned} \tag{2.13}$$

where $\mathsf{R}_\bullet(\phi_\bullet)$ is the addition of all the non-transitory terms of the system of discrete equations. The superscripts stand for the time integration step (+Runge-Kutta sub-step).

The boundary conditions are the characteristics-based 2nd-order boundary of Poinsot and Lele [24].

As it is explained in the paper of Sipegel et al. [22], the original 2D Isentropic vortex consists of a vortex travelling while spinning in a domain. From this original problem, the characteristic time of the flow is the time it takes the center of the vortex to propagate completely throughout the entire the computational domain and return back to its initial position. Here, we study the case in which $\boldsymbol{u}_\infty = \mathbf{0}$ and the vortex is steady. For this case, the definition of the characteristic should be based on the time it takes a fluid particle to complete a turn around the center of rotation. For a fluid

particle at a distance R from the center of the vortex this is $\frac{2\pi R}{u(R)}$, which gives

$$T_1 = \frac{4\pi^2\sqrt{\gamma}\exp(0.5)}{5}$$

in the present parametrization. For the sake of comparison with the results of the moving vortex, however, it is better to keep a period related with the reference paper. Thus, the characteristic period refers to the travelling vortex

$$T_2 = \frac{T_1}{M_\infty \pi \exp(1)}\,.$$

2.3.1 Stationary Vortex

The stationary vortex case shows how some of the SP schemes are more stable than others. In the str80 mesh, only RZM and MRZM schemes are stable after more than 100 T_2 periods. In the unstr80 mesh, the stability differences become more evident and only MRZM is stable after more than 100 periods.

Table 2.3: Table : Blow-Up times for the 2D Isentropic Stationary Vortex case.

Mesh	*JST*	*KEP*	*KOK*	*RZM*	*MRZM*
str80	38	26	26	529	277
str200	20	34	33	358	282
unstr80	5.8	9.3	13	76	137
unstr200	16	33	25	64	67

After these results, it seems convenient to check if the stability enhancement of RZM and MRZM is due to a possible higher numerical dissipation. To this end, the kinetic energy evolution is plotted in the range $[0, 40]$ for str80 mesh and in the range $[0, 15]$ for the unstr80 mesh.

The results in figures 2.1 - 2.3 do not show any additional dissipation for RZM and MRZM.

The errors with the different schemes are plotted in figures 2.4-2.6. RZM and MRZM do not show higher errors than the other schemes during the periods when these have not blown up. Additionally, in the str80 mesh, the errors with MRZM are higher than those of RZM. On the contrary, MRZM induces lesser errors and delays the blow-up with respect to RZM in the unstructured mesh. The conclusion is that

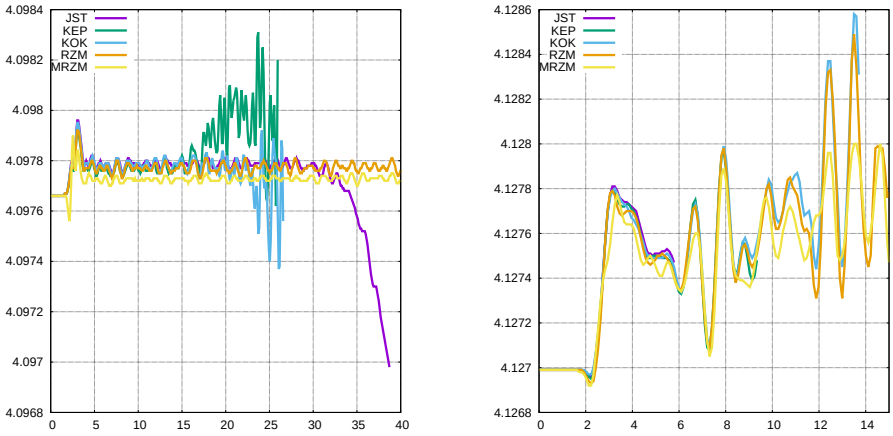

Figure 2.1: Mass evolution with time with various SP schemes in the 2D isentropic vortex case. Left: str80 mesh. Right: unstr80 mesh.

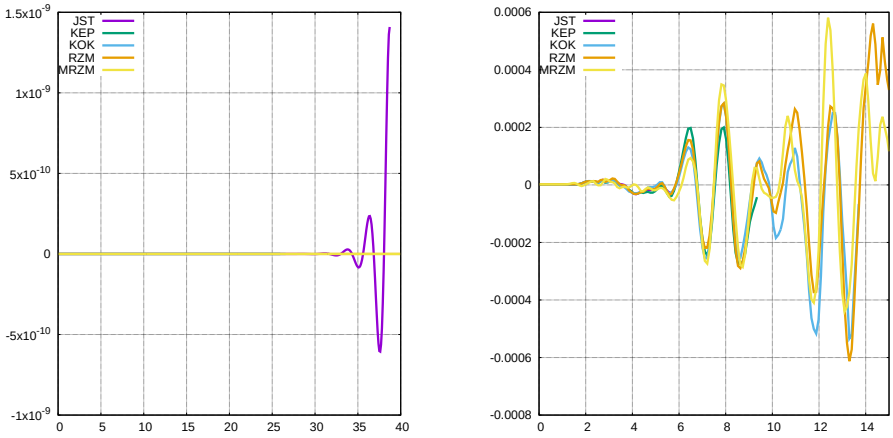

Figure 2.2: Momentum in "x" evolution with time with various SP schemes in the 2D isentropic vortex case. Left: str80 mesh. Right: unstr80 mesh.

RZM and MRZM are the most stable schemes. RZM is more accurate in uniform Cartesian meshes while MRZM shows more accurate in unstructured meshes.

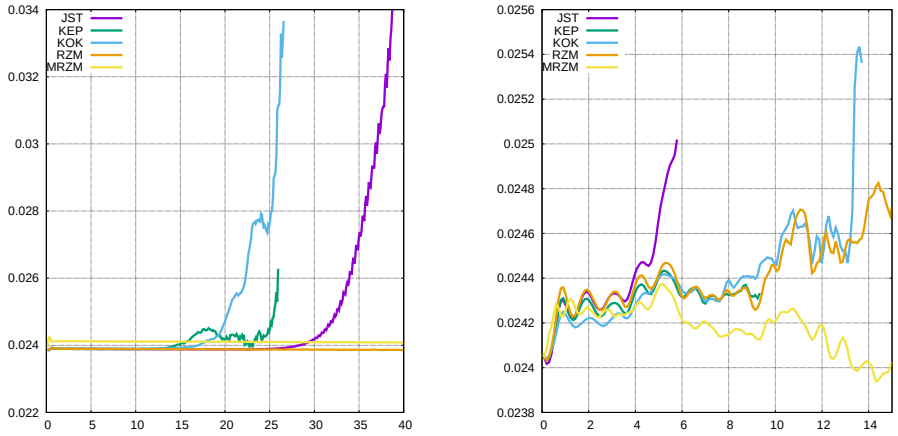

Figure 2.3: Kinetic Energy evolution with time with various SP schemes in the 2D isentropic vortex case. Left: str80 mesh. Right: unstr80 mesh.

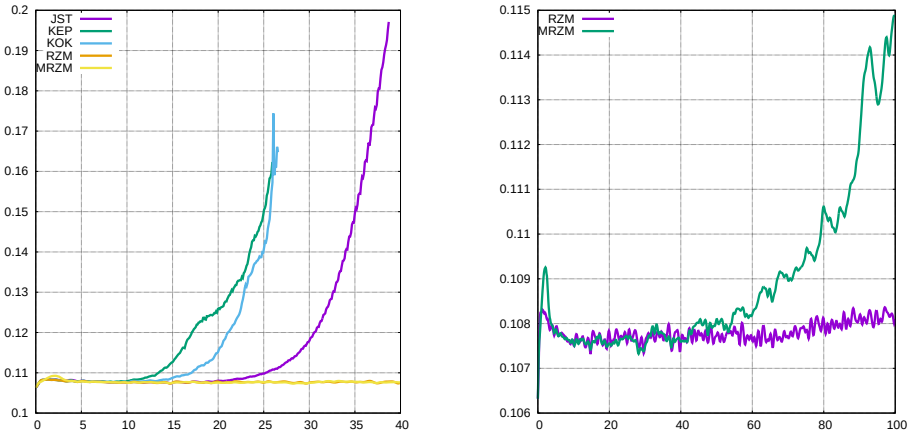

Figure 2.4: Error in velocity $\frac{\langle u_o - u(x_o) | u_o - u(x_o) \rangle}{\langle 1 | 1 \rangle}$ in the 2D isentropic vortex case and str80 mesh. Left: all schemes. Right: RZM and MRZM.

But even when simulations with RZM and MRZM remain stable at very long integration times, the errors with unstuctured meshes are one order of magnitude higher than those obtained with Cartesian meshes (see Fig. 2.6). To better illustrate the difference in accuracy with the various meshes and schemes, the distribution of

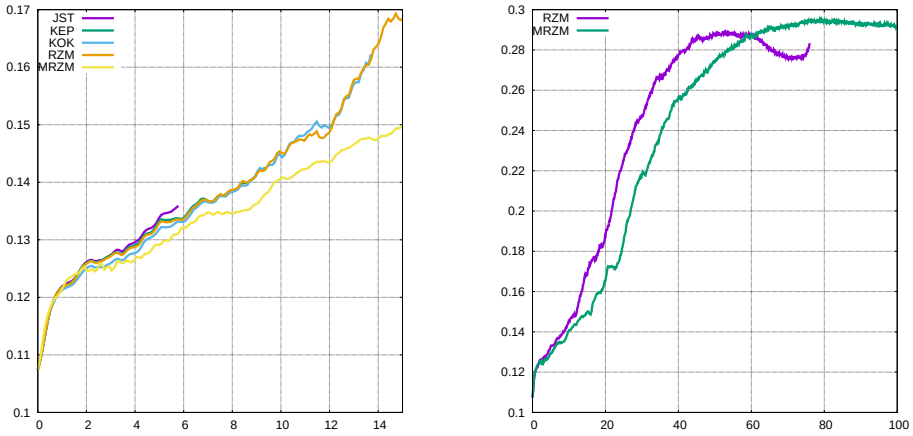

Figure 2.5: Error in velocity $\frac{\langle \boldsymbol{u}_o - \boldsymbol{u}(\boldsymbol{x}_o) | \boldsymbol{u}_o - \boldsymbol{u}(\boldsymbol{x}_o) \rangle}{\langle 1 | 1 \rangle}$ in the 2D isentropic vortex case and unstr80 mesh. Left: all schemes. Right: RZM and MRZM.

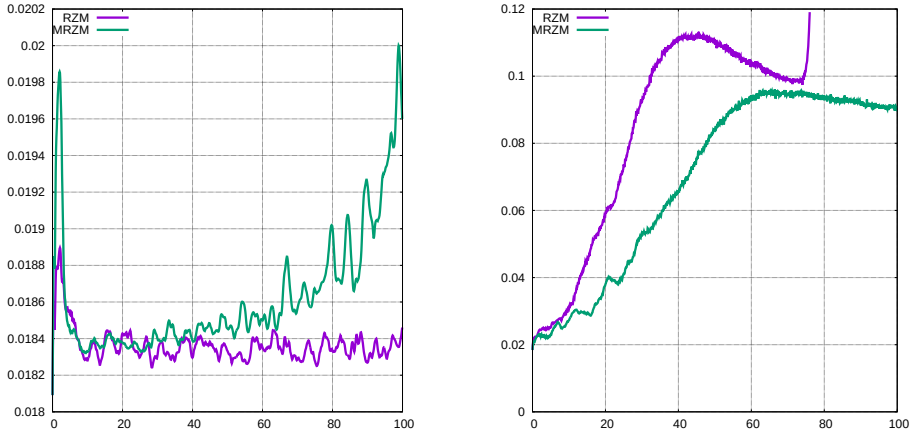

Figure 2.6: Mass error evolution with time $\frac{\langle |\rho_o - \rho(\boldsymbol{x}_o)| | 1 \rangle}{\langle 1 | 1 \rangle}$ in the 2D isentropic vortex case. *RZM* vs *MRZM* schemes. Left: str80 mesh. Right: unstr80 mesh.

density "ρ" along the line $y = 0$ has been plotted for $t = 3$ in Fig. 2.7 and for $t = 30$ in Fig. 2.8. All schemes approximate very closely the exact solution in the structured meshes and very slight differences can be observed in the unstructured meshes at $t = 3$. In contrast, at $t = 30$, JST and KOK do not appear because they have already

blown up. The remaining schemes match very well with the exact solution with str80. With str200, KEP shows oscillations in which density takes values $\rho > 1$ out of the range of the problem. Meanwhile, with the same mesh at at the same time, RZM and MRZM match very well with the exact solution. In the case of the unstructured grids, all the schemes show oscillations and density takes values out of the range of the case.

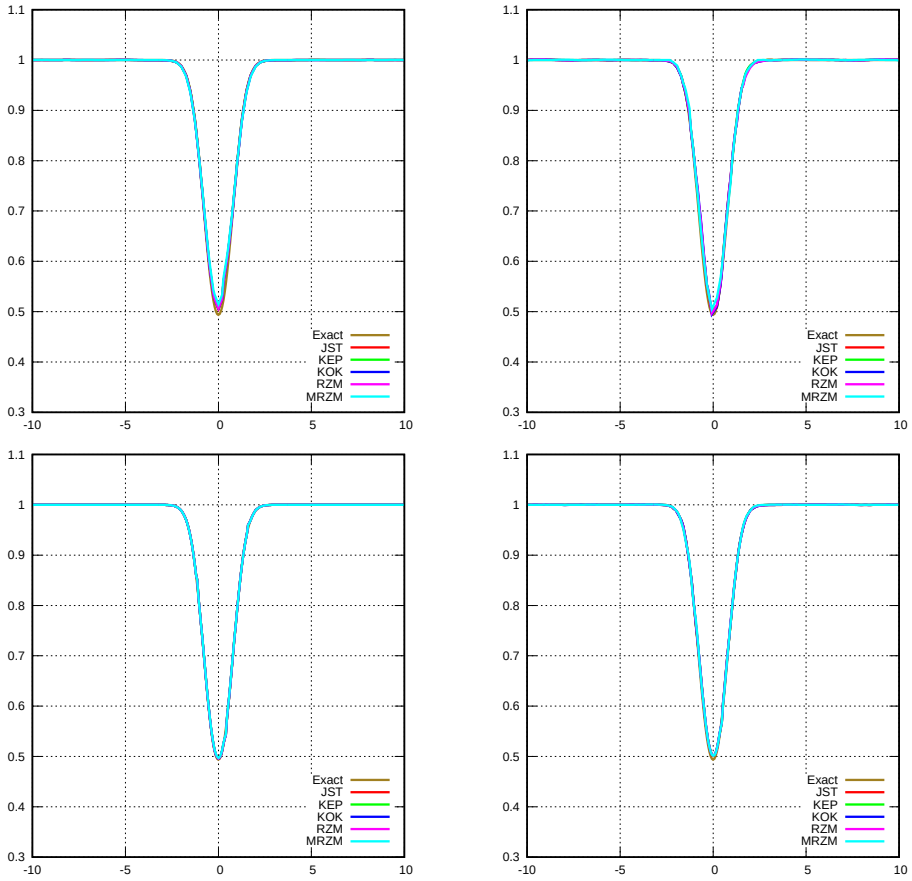

Figure 2.7: Density ρ along line $x \in [-10, 10]$; $y = 0$ at $t = 3$ in the 2D isentropic vortex case with different SP schemes on various meshes. From left to right and from top to bottom: str80, unstr80, str200 and unstr200.

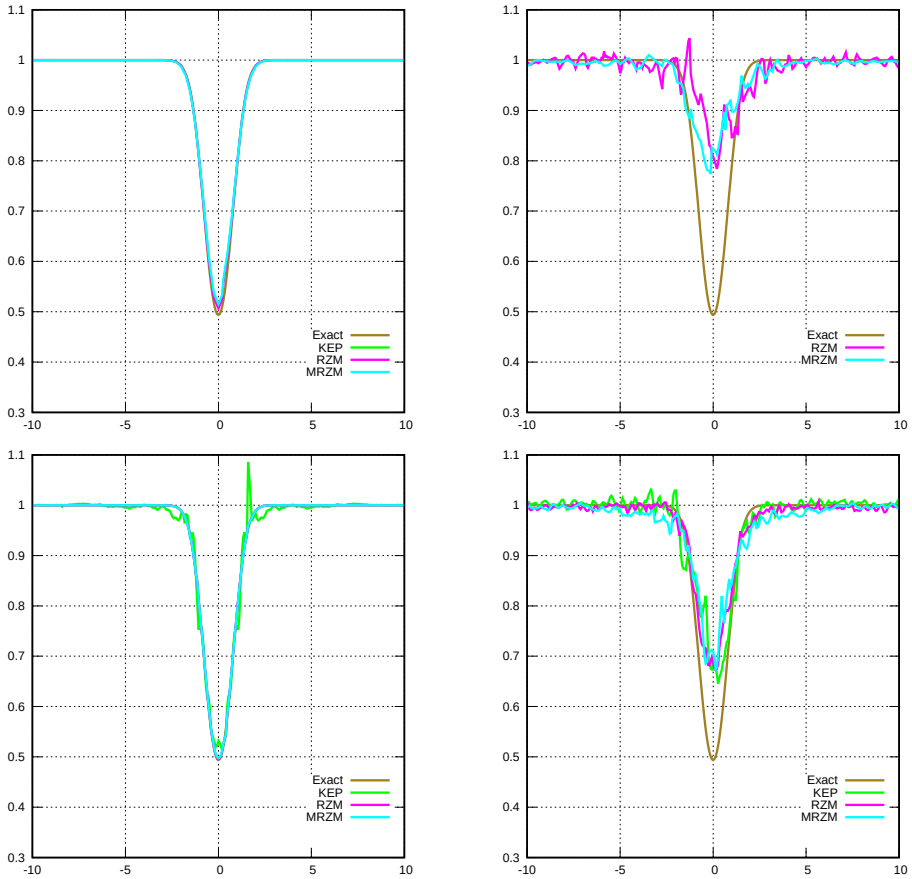

Figure 2.8: Density ρ along line $x \in [-10, 10]$; $y = 0$ at $t = 30$ in the 2D isentropic vortex case with different SP schemes on various meshes. From left to right and from top to bottom: str80, unstr80, str200 and unstr200.

To end with the stationary vortex case, the results of error in density results of the two more stable schemes are compared to those using Flux Reconstruction reported in [22]. Figure 2.9 shows how the error of RZM and MRZM does not increase with time in the uniform meshes while the Flux Reconstruction Schemes in Spiegel et al. do. Furthermore, the $P2$ schemes in Spiegel et al. require using polynomial interpolation within each control volume, i.e., they increase the overall number of degrees of freedom N_{DOF} needed to define the fluid fields. In this case, with polynomials of

second-order, $P = 2$, $N_p = (P+1)^{dim}$ control points are required in each cell. This gives 3 points per cell in each dimmension for the $P2$ polynomials and, in our 2D vortex, $N_{DOF} = 3 \times N_{cells}$ per dimension. At the end, figure 2.9 is comparing the SP schemes reported here with a flux reconstruction scheme with 9 times more degrees of freedom. The results with the lesser degrees of freedom reported in Spiegel et al. are 40×40 meshes with $P3$, i.e., $N_{DOF} = 160 \times 160$. These simulations are reported to be unstable. Finally, no evolution of kinetic energy is reported in [22] and, as the error in figure 2.9 grows in time, it can be suspected that this is due to the effect of some artificial diffusion.

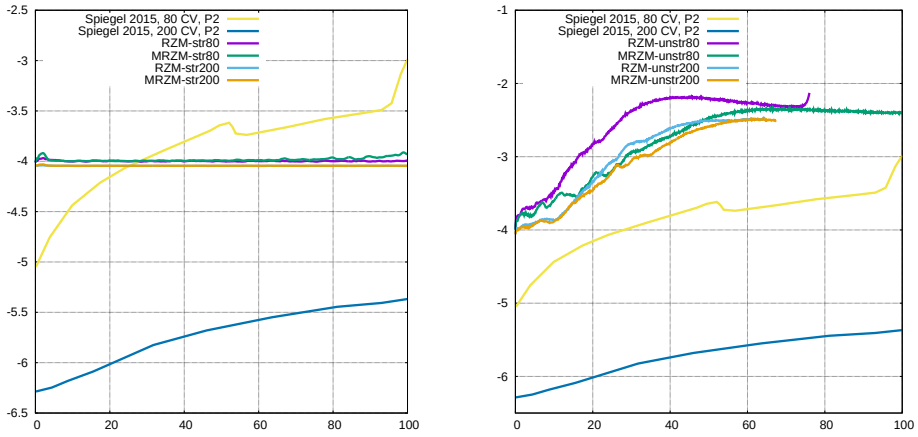

Figure 2.9: Error in mass $\frac{\langle |\rho_o - \rho(\boldsymbol{x}_o)||1\rangle}{\langle 1|1\rangle}$ in the 2D isentropic vortex case. RZM and $MRZM$ schemes vs. refference [22]. Left: Cartesian meshes. Right: SP in unstructured meshes vs. refference in Cartesian meshes.

2.4 Taylor-Green Vortex

To assess the capacity of the numerical schemes summarized in table 2.1 to accurately simulate turbulence, they are tested on the Taylor-Green vortex (TGV) [25]. This problem consists of the time evolution of the flow in a cubic box with sides of length $2\pi L$ and periodic boundary conditions where a smooth initial vorticity field is prescribed. Then, as time advances, eddies roll-up, stretch, and interact. Eventually, eddies break-up into smaller eddies and so on until a homogeneous turbulent field is reached. After this, since no energy is injected into the flow domain, turbulence

dissipates into internal energy and the fluid evolves to rest. The problem set-up is described in [26], which is the same as in the first AIAA First International Workshop on High-Order Methods in Computational Fluid-Dynamics.

The initial conditions are:

$$\boldsymbol{u} = V_0 \left\{ \begin{array}{c} \sin\left(\frac{x}{L}\right)\cos\left(\frac{y}{L}\right)\cos\left(\frac{z}{L}\right) \\ -\cos\left(\frac{x}{L}\right)\sin\left(\frac{y}{L}\right)\cos\left(\frac{z}{L}\right) \\ 0 \end{array} \right\},$$

$$p = p_0 + \frac{\rho_0 V_0^2}{16}\left(\cos\left(\frac{2x}{L}\right) + \cos\left(\frac{2y}{L}\right)\right)\left(\cos\left(\frac{2z}{L}\right) + 1\right),$$

$M = 0.1$ and $Re = 1600$.

This study is performed using the meshes in table 2.4. However, not all schemes have been run in all the meshes because this test is complementary to the isentropic vortex.

Table 2.4: Table : Meshes in the Taylor-Green case.

Name	Description	Cells
cart32	cubic cartesian	32^3
cart64	cubic cartesian	64^3
cart256	cubic cartesian	256^3
uns	extr. [a] tri. [b] 38x28 cells/edge	$1 \cdot 10^5 (114608)$
unstr64	extr. tri. 64 cells/edge	$2 \cdot 10^6$ (2028466)
unstr128	extr. tri. 128 cells/edge	$13 \cdot 10^6$ (13035735)

[a] Extruded.
[b] Triangles.

Figure 2.10 shows the results obtained with the RZM scheme and the WALE eddy viscosity model [27] on the Cartesian meshes. It shows that when refining the mesh the results of RZM approach the reference solution of [26] obtained with a cartesian mesh of 512^3 cells and a 13 points interpolation scheme.

The errors commited with RZM schemes on the 64^3 mesh are very similar to those commited in DeBonis [26] with the same mesh and 13 points interpolation scheme.

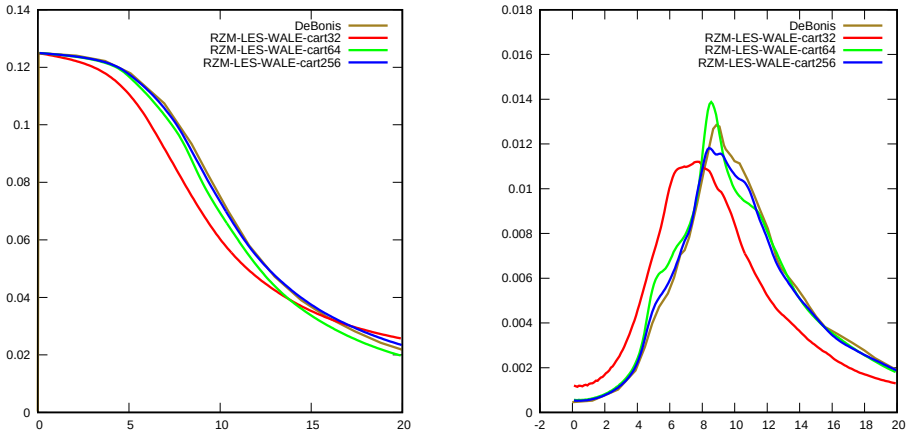

Figure 2.10: Evolution in time of magnitudes of the Taylor-Green case in cartesian meshes and refference solution [26], 513^3 Cartesian mesh, 13 points interpolation. Left: Kinetic energy evolution. Right: Dissipation $\frac{dK}{dt}$.

Taking into account that RZM is a lower order scheme, the present methodology is computationally cheaper than the one used in the reference document. With 256^3 meshes, however, the high order schemes in [26] give more accurate results than the actual implementation of RZM, always at a higher computing cost.

Figures 2.11 and 2.12 show the evolution of magnitudes obtained with KEP, MRZM and RZM on cart32 and cart64. RZM and KEP collapse to the same results while MRZM's are slightly different. After this, we will assume that these schemes give undistinguishable results in Cartesian meshes as long as they are far from blowing up.

The results of the simulations with unstructured meshes and the RZM scheme are shown in figure 2.13. The mesh refinement in this type of meshes does not make the results more accurate at the pace of what happens with cartesian meshes. This is a direct consequence of the truncantion error of the schemes in unstructured meshes, which is in this case higher (it is not my intention to conduct a truncation error analysis here). For more details about the truncation error of this type of schemes, see e.g. [28]. Figure 2.14 shows the results given by RZM and MRZM. MRZM became unstable at the beginning of the simulation.

The major source of error of the unstructured meshes simulations seems to come from an early instability on the initial flow. A shift on 1.71 time units (t.u.) on the

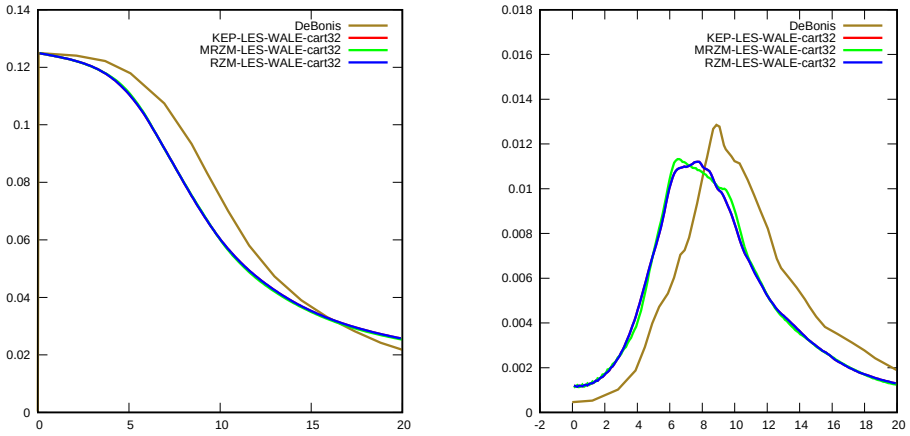

Figure 2.11: Evolution in time of magnitudes of the Taylor-Green case in cart32 with WALE and various schemes and refference solution [26], 513^3 Cartesian mesh, 13 points interpolation. Left: Kinetic energy evolution. Right: Dissipation $\frac{dK}{dt}$.

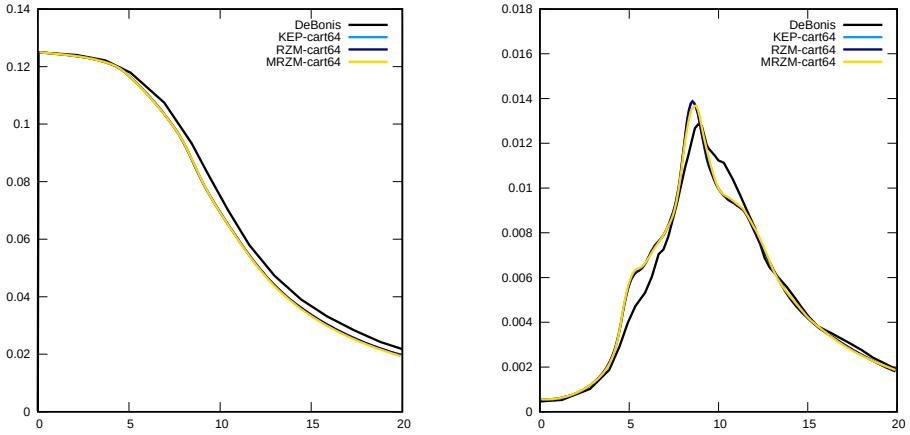

Figure 2.12: Evolution in time of magnitudes of the Taylor-Green case with WALE in cart64 and various schemes and refference solution [26], 513^3 Cartesian mesh, 13 points interpolation. Left: Kinetic energy evolution. Right: Dissipation $\frac{dK}{dt}$.

simulated results gives Figure 2.15. The time shift was chosen to make the plots coincide at the point where $dK/dt = 0.002$, which is the value where the dissipation

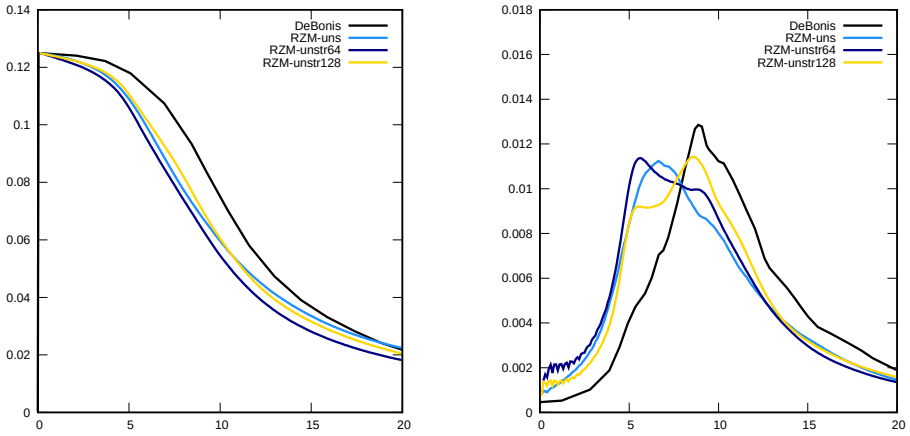

Figure 2.13: Evolution in time of magnitudes of the Taylor-Green case in unstructured meshes and refference solution [26], 513^3 Cartesian mesh, 13 points interpolation. Left: Kinetic energy evolution. Right: Dissipation $\frac{dK}{dt}$.

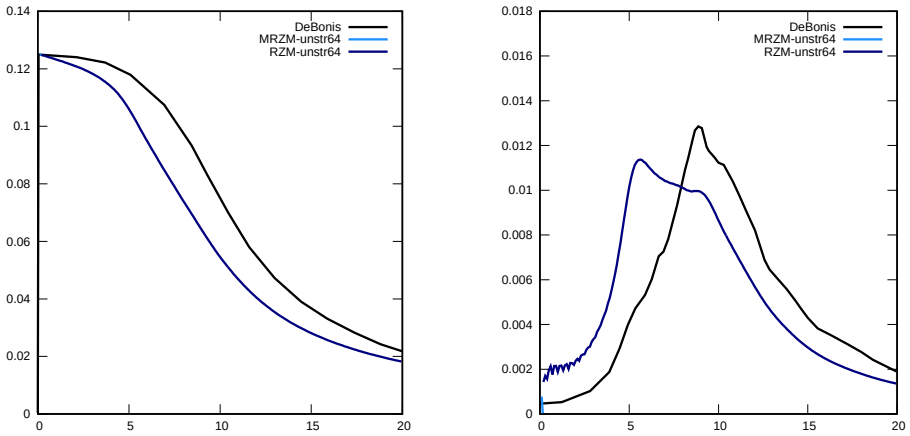

Figure 2.14: Evolution in time of magnitudes of the Taylor-Green case with WALE in unstr64 using RZM and MRZM schemes and refference solution [26], 513^3 Cartesian mesh, 13 points interpolation. Left: Kinetic energy evolution. Right: Dissipation $\frac{dK}{dt}$.

starts to steeply increase following, approximately, a straight line. I consider that this is the start of the turbulent transition. After the time shift, it seems that the main be-

havior of the flow is well reproduced with RZM scheme in the unstructured meshes. However, properly checking mesh convergence would require to simulate the flow with much finer meshes.

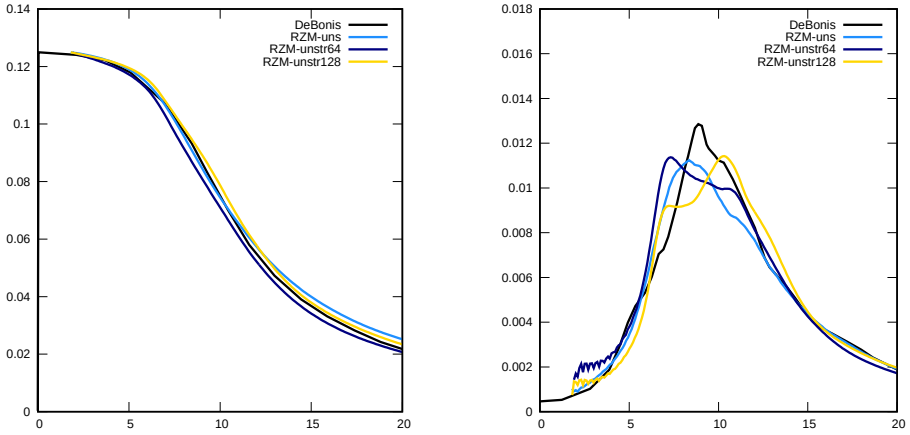

Figure 2.15: Evolution in time of magnitudes of the Taylor-Green case in unstructured meshes with a 1.71 t.u shift in time and refference solution [26], 513^3 Cartesian mesh, 13 points interpolation. Left: Kinetic energy evolution. Right: Dissipation $\frac{dK}{dt}$.

2.5 Concluding remarks

The comparison of SP schemes in this chapter shows that RZM and MRZM are more stable than the other schemes. Furthermore, RZM is more accurate in uniform meshes and MRZM is more stable in unstructured meshes in the isentropic vortex case. In the Taylor-Green vortex case, RZM is more stable than MRZM.

In the static 2D vortex, both RZM and MRZM blow-up later in the coarse mesh than in the finer, while the other schemes show an opposite behavior. It is also interesting that the slight modification to RZM originally introduced here shows a better performance in the unstructured meshes and a worse performance in the uniform ones. Yet, the conclusions obtained here attain the studied cases only and are not strong enough to make recommendations for general LES simulations. Finding a new numerical scheme is not a primary objective of this thesis but, as it comes to pass, MRZM shows better performance than any of the other studied SP schemes in

unstructured meshes in this test. This issue will be further developed later, in the isotropic turbulence simulations in chapter 5 and in the final conclusions.

If we compare the performance of the studied schemes in the isentropic vortex case to Speigel et al. [22], for low resolution meshes and long time integration, RZM and MRZM outperform any other scheme. One could argue here that these schemes are low order and they do not give good local accuracy. But their Symmetry Preserving properties imply that they do not increase the errors with excessive diffusion. In LES, some turbulent scales are represented with very few degrees of freedom because the mesh resolution is limited in turbulent zones. Thus, schemes with the capacity to handle these under-resolved scales without artificially dissipating them or blowing-up allow to conduct LES with a strict control on the added dissipation. Then, it will come only from the flow viscosity and the turbulence model. Never, in LES, one can expect to represent the turbulent scales in the inertial range with a mesh as fine with respect to the characteristic sizes of the scales as the coarsest meshes reported here (i.e. str80 and unstr80) as this would inevitably cause the meshes to be over-refined and the numerical simulations over-costly.

The simulations on the Taylor-Green case confirm that SP schemes are very well suited to simulate isotropic/homogeneous turbulence. With comparatively coarse meshes, they allow to obtain acceptable results at low computing costs. The results on the unstructured meshes are more disappointing because it does not seem that increasing the mesh density improves them enough. Furthermore, MRZM becomes unstable in unstructured meshes. However, even with these meshes, the simulated flow reproduces the main features of the reference solution.

The long-term analysis on the static vortex also shows that SP schemes need some mechanism to eliminate oscillations when used in unstructured meshes. The ideal solution would be to modify SP schemes so wiggles do not appear without adding any artificial dissipation. However, after analyzing the literature, it seems that all wiggle-eliminating methodologies add it in one or another way. In the following of the thesis, this task will be carried out by filtering the numerical solution at each time step. I consider this is the most clear and transparent way to introduce artificial dissipation.

References

[1] S. Patankar. *Numerical heat transfer and fluid flow*. CRC press (Taylor&Francis Group), New York, 1980.

[2] S. K. Godunov. A difference method for numerical calculation of discontinuous solutions of the equations of hydrodynamics. *Math. Sbornik*, 47(89):271–306, 1959.

[3] A. Harten. High Resolution Schemes for Hyperbolic Conservation Laws. *Journal of Computational Physics*, 135:260–278, 1983.

[4] Xu-Dong Liu, S. Osher, and Tony Chan. Weighted essentially non-oscillatory schemes. *Journal of Computational Physics*, 115(1):200–212, 1994.

[5] B. P. Leonard. A stable and accurate convective modelling procedure based on quadratic upstream interpolation. *Computer Methods in Applied Mechanics and Engineering*, 19(1):59–98, 1979.

[6] Y. Morinishi, T. S. Lund, O.V. Vasilyev, and P. Moin. Fully Conservative Higher Order Finite Difference Schemes for Incompressible Flow. *Journal of Computational Physics*, 143:90–124, 1998.

[7] H. F. Harlow and E. F. Welch. Numerical Calculation of Time-Dependent Viscous Incompressible Flow of Fluid with Free Surface. *Physics of Fluids*, 8(12):2182, 1965.

[8] A. Arakawa. Computational design for long-term numerical integration of the equations of fluid motion: Two dimensional incompressible flow. Part I. *J. Comput. Phys.*, 1(122):119–143, 1966.

[9] R. W. C. P. Verstappen and A. E. P. Veldman. Symmetry-preserving discretization of turbulent flow. *Journal of Computational Physics*, 187:343–368, 2003.

[10] B. J. Perot. Discrete Conservation Properties of Unstructured Mesh Schemes. *Annual Review of Fluid Mechanics*, 43(1):299–318, 2011.

[11] F. X. Trias, O. Lehmkuhl, A. Oliva, C. D. Pérez-Segarra, and R.W.C.P. Verstappen. Symmetry-preserving discretization of Navier-Stokes equations on collocated unstructured grids. *Journal of Computational Physics*, 258:246–267, 2014.

[12] S. Pirozzoli. Numerical Methods for High-Speed Flows. *Annual Review of Fluid Mechanics*, 43:163–194, 2011.

[13] W.J. Feireisen, W.C. Reynolds, and J.B. Ferziger. Numerical simulations of compressible homogeneous turbulent shear flows. *Report TF-13 (unpublished) Thesis, Stanford University*, 1981.

[14] A. Jameson. Formulation of kinetic energy preserving conservative schemes for gas dynamics and direct numerical simulation of one-dimensional viscous compressible flow in a shock tube using entropy and kinetic energy preserving schemes. *Journal of Scientific Computing*, 34:188–208, 2008.

[15] W. Rozema. *Low-dissipation methods and models for the simulation of turbulent subsonic flow*. PhD thesis, University of Groningen, 2015.

[16] A.G. Kravchenko and P. Moin. On the Effect of Numerical Errors in Large Eddy Simulations of Turbulent Flows. *Journal of Computational Physics*, 131:310–322, 1997.

[17] F. Ducros, F. Laporte, T. Soulères, V. Guinot, P. Moinat, and B. Caruelle. High-Order Fluxes for Conservative Skew-Symmetric-like Schemes in Structured Meshes: Application to Compressible Flows. *Journal of Computational Physics*, 161:114–139, 2000.

[18] Antony Jameson, Wolfgang Schmidt, and Eli Turkel. Numerical solution of the euler equations by finite volume methods using runge kutta time stepping schemes. In *14th fluid and plasma dynamics conference*, page 1259, 1981.

[19] J. C. Kok. A high-order low-dispersion symmetry-preserving finite-volume method for compressible flow on curvilinear grids. *Journal of Computational Physics*, 228(18):6811–6832, 2009.

[20] W. Rozema, J. C. Kok, R.W.C.P. Verstappen, and A.E.P. Veldman. A symmetry-preserving discretisation and regularisation model for compressible flow with application to turbulent channel flow. *Journal of Turbulence*, 15(March 2015):386–410, 2014.

[21] Chi-Wang Shu. Chapter 4: Essentially non-oscillatory and weighted essentially non-oscillatory schemes for hyperbolic conservation laws. *Advanced Numerical Approximation of Nonlinear Hyperbolic Equations*, 1697(97-65):325–432, 1998.

[22] S. C. Spiegel, H. T. Huynh, and J. R. DeBonis. A survey of the isentropic euler vortex problem using high-order methods. In *22nd AIAA Computational Fluid Dynamics Conference*, page 2444, 2015.

[23] S. Gottlieb and Chi-Wang Shu. Total variation diminishing Runge-Kutta schemes. *Mathematics of Computation*, 67(221):73–85, 1998.

[24] T. J. Poinsot and S. K. Lele. Boundary Conditions for Direct Simulations of Compressible Viscous Flows. *Journal of Computational Physics*, 101:104–129, 1992.

[25] G. I. Taylor and A. E. Green. Mechanism of the Production of Small Eddies from Large Ones. *Proceedings of the Royal Society of London A: Mathematical, Physical and Engineering Sciences*, 158(895):499–521, 1937.

[26] J. DeBonis. Solutions of the Taylor-Green Vortex Problem Using High-Resolution Explicit Finite Difference Methods. *51st AIAA Aerospace Sciences Meeting including the New Horizons Forum and Aerospace Exposition*, (February):1–9, 2013.

[27] F. Nicoud and F. Ducros. Subgrid-scale stress modelling based on the square of the velocity gradient tensor. *Flow, Turbulence and Combustion*, 62:183–200, 1999.

[28] L. Jofre, O. Lehmkuhl, J. Ventosa, F.X. Trias, and A. Oliva. Conservation properties of unstructured finite-volume mesh schemes for the navier-stokes equations. *Numerical Heat Transfer, Part B: Fundamentals*, 65(1):53–79, 2014.

3

Analytic Filters

3.1 Introduction

Computational Fluid Dynamics (CFD) is the branch of fluid dynamics that studies algorithms and performs numerical simulations of fluid flow. Low-pass spatial filtering is a conventional operation of CFD. It is applied to input scalar fields to dissipate their small wavelengths. Similar operations are performed in the field of signal analysis and image processing, but CFD has particularities that do not allow direct use of alien literature. First, spatial discretisations in CFD can be non-uniform while they are uniform in the other fields of application of discrete filtering. Second, filtered fields are often calculated at each iteration of a CFD simulation, and the evolution of the simulated variables is computed using the filtered fields while in image processing there is always a fresh input available. Hence, for some CFD applications, filtering should exactly verify properties, e.g. conservation, to preserve those of the overall simulation. Third, CFD fields can be significantly larger than high definition images, so the amount of running-time processed data is larger. Finally, filtering is not the main operation in CFD while it is in the other fields. Thus, filtering in CFD has its own particularities and should be studied separately. Additionally, the computers used for CFD are multi-purpose while the image or signal-processing ones can be fully adapted to that end. Consequently, filtering in CFD should require the lesser computer resources possible on a wide range of computer architectures.

The purposes of filtering in CFD are diverse and each of them requires the filters to accomplish a specific set of properties. The most relevant use of filters in CFD is to apply them on the Navier-Stokes Equations (NSE) and thus allow the theoretical deduction of the Large Eddy Simulations (LES) equations [1]. To this end, filters should be linear, commutative with differentiation, normalised and conservative. Low-pass convolution filters match these properties and the LES equations are consistently derived. However, in practice, convolution is not performed in actual LES with discrete

operators because it consumes too much computer effort. Hence, other analytical filter models with lesser computer intensive discrete counterparts have been proposed in the literature, e.g., [2–4]. But any of the known approaches reproduce all the characterising properties of convolution filters at the same time. Meanwhile, in other applications, these models can match all the necessary properties.

A common application for which this happens is filtering fields for the calculation of closures of Sub-Grid Scales Stresses models for LES, e.g., [5–7]. For this purpose, commutation with differentiation and conservation can be relaxed. Another application for which filters match all the required properties is filtering the fluid variables to stabilise non-dissipative or high-order numerical schemes [8–10]. In this case, conservation is relevant while commutation with differentiation is not. The same happens when filters are applied to smear sharp body forces like those of the Immersed Boundary Method (see a review of the methodology in [11]) or those producing wind-turbine wakes (e.g., [12]) that are introduced in LES.

It seems that specific filter analytical models and discretisations should be chosen depending on the specific application and it is the specific use what determines the required set of filter properties that allow keeping the overall consistency of a CFD simulation. In this sense, the global filter properties are not always explicitly mentioned or taken into account in the literature. Furthermore, there does not seem to be a compendium of filters with their global properties that would be useful for researchers when facing the choice of a filter for an application. Finally, there is not a standard minimum set of properties characterising filters. Thus, an operator can be applied as it was a filter while its properties are not taken into account or, in other words, a filter can be applied in a context for which its properties are not appropriate.

This chapter is dedicated to summarise the filter models in the literature and specify and describe their properties in order to ease application-depending selection of filters. Obvious properties are just mentioned while others are proved when estimated convenient. Afterwards, the convenience of defining a minimum set of properties characterising filtering in CFD is discussed.

In the following, we use $\phi(\boldsymbol{x})$ or simply ϕ to denote a general function $\phi : \mathbb{R}^n \rightarrow \mathbb{R}$. A filtering operator F is applied on ϕ giving

$$\hat{\phi}(\boldsymbol{x}) = \mathsf{F}(\phi)(\boldsymbol{x})$$

or, simplyfying the notation

$$\hat{\phi} = \mathsf{F}(\phi)$$

. The symbol $\boldsymbol{x}$ denotes space coordinates.

Many of the properties can be written as relationships between the inner products of the filtered and unfiltered functions. Thus, we define the inner product of two functions ϕ, $\psi : \Omega \subseteq \mathbb{R}^n \mapsto \mathbb{R}$

$$\langle \phi | \psi \rangle = \int_\Omega \phi(\boldsymbol{\xi}) \psi(\boldsymbol{\xi}) \, d\boldsymbol{\xi},$$

where $\boldsymbol{\xi}$ denotes space coordinates.

3.2 Convolution filter

The convolution filter reads:

$$\hat{\phi}(\boldsymbol{x}) = K_C * \phi = \int_\Omega K_C(\boldsymbol{\xi}) \phi(\boldsymbol{x} - \boldsymbol{\xi}) \, d\boldsymbol{\xi}, \tag{3.1}$$

where K_C is the filter kernel and is related to the cutoff scales (characteristic of the filter) through a filter characteristic length. The kernel functions K_C of convolution filters are compact supported or rapidly decaying. Next, the most common convolution filters are listed.

3.2.1 n-Dimensional Box filter

The box filter is a convolution filter with the following kernel:

$$K_{Box}(\boldsymbol{\xi}, R) = \begin{cases} \frac{1}{V_n(R)} & if \quad |\boldsymbol{\xi}| \leq R \\ 0 & if \quad |\boldsymbol{\xi}| > R \end{cases}, \tag{3.2}$$

where $R \in \mathbb{R}^+$ and $V_n(R) = \frac{\pi^{\frac{n}{2}}}{\Gamma(\frac{n}{2}+1)} R^n$ is the volume of an n-dimensional ball of radius R and Γ is the gamma function (see figure 3.1).

3.2.2 n-Dimensional Gaussian filter

The Gaussian filter is a convolution filter with the following kernel:

$$K_{Gauss}(\boldsymbol{\xi}, \sigma) = \frac{1}{\sqrt{(2\pi\sigma^2)^n}} \exp\left(-\frac{1}{2\sigma^2} \boldsymbol{\xi} \cdot \boldsymbol{\xi} \right), \tag{3.3}$$

where σ^2 is the variance (see figure 3.2).

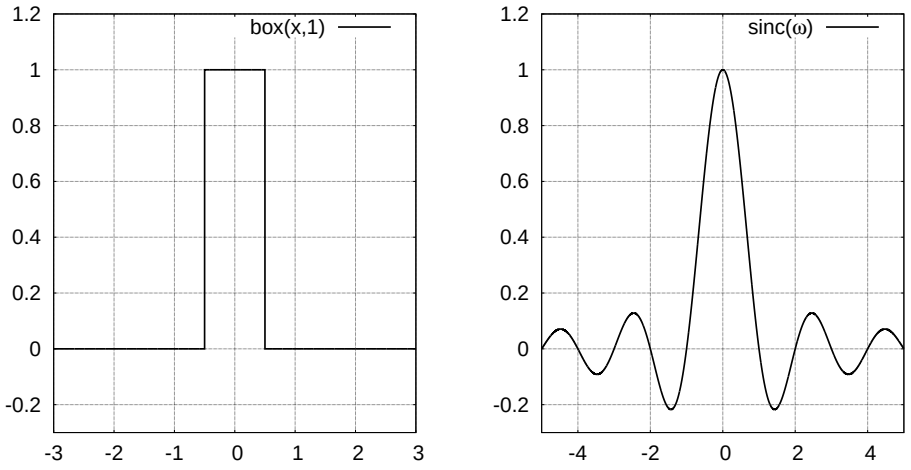

Figure 3.1: Kernel of the 1D box filter. Left:physical space, Right: Fourier space.

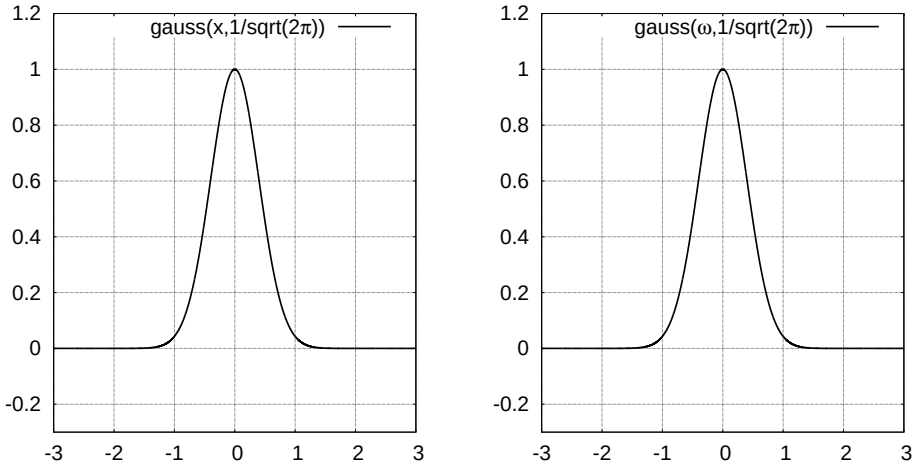

Figure 3.2: Kernel of the 1D Gaussian filter. Left:physical space, Right: Fourier space.

3.2.3 n-Dimensional sharp cut-off filter

The image in the physical space of the low-pass sharp cut-off filter in 1D is the convolution filter whose kernel is

$$K_{cut} = \frac{\sin(2k\pi x)}{\pi x} = 2k\,\mathrm{sinc}(2kx),$$

where k is the cut-off frequency (see figure 3.3). Its generalization to higher dimensions is obtained after applying the inverse Fourier transform of a sphere in the multidimensional modal space. One gets

$$K_{ncut} = \frac{J_{\frac{n}{2}}(2\pi k|\boldsymbol{\xi}|)}{\sqrt{k|\boldsymbol{\xi}|^n}}, \tag{3.4}$$

where $J_{\frac{n}{2}}$ is the Bessel function of the first kind with order $\frac{n}{2}$.

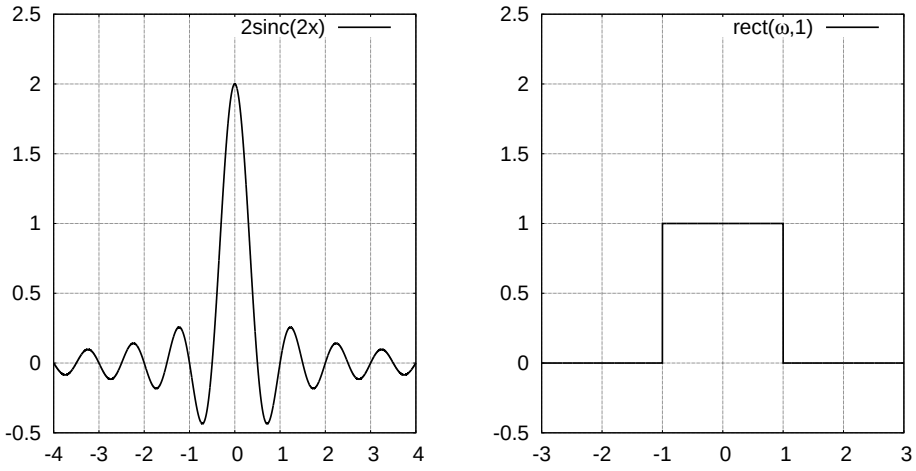

Figure 3.3: Kernel of the 1D sharp cut-off filter. Left: physical space, Right: Fourier space.

3.2.4 Properties of convolution filters

We compile here the properties of convolution filters. Furthermore, the sufficient conditions for their fulfillment in these kind of filters are also anounced. Then, assuming that convolution filters are the paradigmatic filtering operators, the degree in

which other operators will be considered filters will depend on which of these they fulfill. These properties can be divided into 2 subsets. The first set shall be required to all K_C kernels for CFD and is the common set of properties in the literature. The second set imposes that K_C should be positive and non-increasing and is not always required in the literature. The reasons for adding this second set of necessary properties for operators to be allowable filters will be given later in section 3.6. For now, let ϕ, ψ be bounded distributions defined on $\Omega \subseteq \mathbb{R}^n$ and let a, b be real numbers.

Linearity

$$\mathsf{F}(a\phi + b\psi) = a\hat{\phi} + b\hat{\psi}. \tag{3.5}$$

Sufficient condition: The convolution filter is linear after the linearity of the integral.

Normalization Let ϕ be a constant function, then

$$\hat{\phi} = \phi \quad \forall \boldsymbol{x}. \tag{3.6}$$

Sufficient condition:

$$\int_\Omega K_G \, d\boldsymbol{\xi} = 1,$$

i.e.,

$$\langle K_G | 1 \rangle = 1$$

Conservation

$$\int_\Omega \hat{\phi} \, d\boldsymbol{\xi} = \int_\Omega \phi \, d\boldsymbol{\xi}. \tag{3.7}$$

Sufficient condition: Same as normalization.

Commutation with differentiation Let D be a differential operator. Then,

$$\mathsf{D}(\mathsf{F}(\phi)) = \mathsf{F}(\mathsf{D}(\phi)). \tag{3.8}$$

3.2.5 Diffusivity properties of convolution filters

The former properties do not relate with the concept of diffusion and filters fulfilling only them can increase maxima, reduce minima, and increase the total variations of the filtered fields. In section 3.6 the interest of filters with diffusive properties that prevent these ill behaviours is discussed. Such properties are specified here whereas, for the sake of clarity, the pertinent proofs are in Appendix 3.A.

Total Variations Diminishing Taking the $\mathcal{L}_p$ norm $||\cdot||_p$ of a function ϕ

$$||\phi||_p = \left(\int_\Omega |\phi|^p d\boldsymbol{\xi} \right)^{1/p}, \tag{3.9}$$

assuming that the gradient $\nabla\phi$ exists and $|\nabla\phi|^p$ is bounded (this is true for fluid magnitudes with $p > 0$), the Total Variations of order p (TV_p) of an homeomorphism F on ϕ is defined as

$$TV_p(\mathsf{F}, \phi) = ||\nabla \mathsf{F}(\phi)||_p - ||\nabla\phi||_p. \tag{3.10}$$

If $TV_p(\mathsf{F}, \phi) \leq 0$ for all ϕ, then we say that F is TVD_p.

Suficient conditions for TVD_1: Normalization Eq. (3.6) and

$$K_C(\boldsymbol{\xi}) \geq 0 \quad \forall \boldsymbol{\xi} \in \Omega. \tag{3.11}$$

Global Extrema Diminishing Some filters can grow the local maxima or diminish the global minima. This can open the door to blow-up in iterative calculations where the newly calculated values depend on the formerly obtained. Global Extrema Diminishing GED is the property that prevents this from happening.

For GED filters,

$$\min(\phi)_\Omega \leq \hat{\phi} \leq \max(\phi)_\Omega \tag{3.12}$$

Sufficient conditions: Same as for Total Variations Diminishing. For convolution filters, $GED \Leftrightarrow TVD_1$.

Extrema Diminishing Neither GED nor TVD_1 prevent the creation of new local maxima or minima. The property that prevents this from happening is Extrema Diminishing ED, which is more restrictive.

It reads: For all maxima or minima in the filtered function $\hat{\phi}$, they come from at least, respectively, one maximum or minimum in the unfiltered function ϕ. For a more precise definition see Witkin [13]. This is:

$$\begin{aligned} \forall \boldsymbol{x}^* \mid \exists r \in \mathbb{R}^+ \mid \hat{\phi}(\boldsymbol{x}^*) > \hat{\phi}(\boldsymbol{x}) \quad \forall \boldsymbol{x} \in B(\boldsymbol{x}^*, r) \\ \Rightarrow \exists\, (\boldsymbol{x}^{**}, \delta > 0) \mid \phi(\boldsymbol{x}^{**}) > \phi(\boldsymbol{x}) \quad \forall \boldsymbol{x} \in B(\boldsymbol{x}^{**}, \delta) \end{aligned} \tag{3.13}$$

where $B(\boldsymbol{x}^*, r)$ is a ball of radius r centered at $\boldsymbol{x}^*$. Furthermore, no extremum in the filtered field "should be far" from its causing extremum(a) in the unfiltered field. Changing the inequalities directions, the same is true for minima.

Furthermore,

$$\begin{aligned} &M(\Omega, \phi) = \{\boldsymbol{x}^* \in \Omega \,|\, \exists B(\boldsymbol{x}^*, \delta) \,|\, \phi(\boldsymbol{x}^*) \lesseqgtr \phi(\boldsymbol{x})\}\,; \\ &|M(\Omega, \phi)\,| \geq |M(\Omega, \mathsf{F}(\phi))\,| \quad \forall \phi, \end{aligned} \tag{3.14}$$

where $\delta \in \mathbb{R}^+$ and $|A|$ is the cardinality of the set A.

Sufficent conditions: K_C is normalized, non-negative and non-increasing with $|\boldsymbol{\xi}|$. This is:

$$\boldsymbol{\nabla} K_C \cdot \boldsymbol{\nabla} |\boldsymbol{\xi}| \leq 0 \quad \forall \boldsymbol{\xi}. \tag{3.15}$$

3.3 The image of convolution filters in the Fourier space

Let $\boldsymbol{\omega}$ be the wave number independent variable of the Fourier space. The Fourier transform of a periodic or $\mathcal{L}^1$ function $\phi(\boldsymbol{x})$ is defined by:

$$\widetilde{\phi}(\boldsymbol{\omega}) = \int_\Omega \phi(\boldsymbol{x}) \exp\left(-2\pi i \boldsymbol{x} \cdot \boldsymbol{\omega}\right) d\boldsymbol{x}. \tag{3.16}$$

The image $\widetilde{\mathsf{F}}$ of a filter F by the Fourier transform is

$$\widehat{\widetilde{\phi}} = \widetilde{\mathsf{F}}(\widetilde{\phi}) = \widetilde{\mathsf{F}(\phi)}. \tag{3.17}$$

Taking into account

$$\widetilde{f * K_C} = \widetilde{f} \cdot \widetilde{K_C},$$

the convolution filter in the physical space becomes a product in the modal space. Next, the image of the properties of a convolution filter with a $\widetilde{K_C}$ kernel is listed.

Linearity Comes from the distributive property of the product.

$$\widetilde{K_C} \cdot (a\widetilde{f} + b\widetilde{g}) = a\widetilde{K_C}\widetilde{f} + b\widetilde{K_C}\widetilde{g}. \tag{3.18}$$

Normalization Let $\widetilde{\phi}$ be the image in the modal space of a constant field in the physical space. Then,

$$\widetilde{\phi}(\boldsymbol{\omega}) = \begin{cases} \phi_0 & \text{if} \quad \boldsymbol{\omega} = \boldsymbol{0} \\ 0 & \text{if} \quad \boldsymbol{\omega} \neq \boldsymbol{0} \end{cases}$$

then, the normalization property is:

$$\hat{\widetilde{\phi}} = \widetilde{\phi}. \tag{3.19}$$

The sufficient condition for convolution filters is:

$$\widetilde{K_C}(\mathbf{0}) = 1$$

Conservation Substituting $\boldsymbol{\omega} = \mathbf{0}$ of Eq. (3.16) and plugging the result in the conservation equation in the physical space (Eq.(3.7)) we get:

$$\widetilde{\mathsf{F}}(\widetilde{\phi}(\mathbf{0})) = \widetilde{\phi}(\mathbf{0}) \tag{3.20}$$

Sufficient condition for the image of convolution filters: Same as normalisation.

Commutation with differentiation The image of this property in the physical space

$$\mathsf{D}(\mathsf{F}(\phi)) = \mathsf{F}(\mathsf{D}(\phi)),$$

where D is a differential operator. It becomes,

$$\widetilde{\mathsf{D}}\widetilde{\mathsf{F}}(\widetilde{\phi}) = \widetilde{\mathsf{F}}\left(\widetilde{\mathsf{D}}\widetilde{\phi}\right) \tag{3.21}$$

If F is a convolution filter,

$$\widetilde{\mathsf{D}}\left(\widetilde{K_C}\widetilde{\phi}\right) = \widetilde{K_C}\left(\widetilde{\mathsf{D}}\widetilde{\phi}\right).$$

which is true by virtue of the distribution property of the product of real numbers.

Diffusivity in the Fourier space The image of a diffusion problem in the Fourier space is (see, e.g. [14])

$$\left(\frac{\partial}{\partial t} + \nu\boldsymbol{\omega}\cdot\boldsymbol{\omega}\right)\widetilde{\phi}(\boldsymbol{\omega}) = 0, \tag{3.22}$$

where $\nu \in \mathbb{R}^+$ is the diffusion coefficient. If we take Eq.(3.22) as the paradigm for diffusive filters, it can be used to derive the properties of such filters in the Fourier space. This equation can be easily integrated, giving

$$\hat{\widetilde{\phi}}(\boldsymbol{\omega}) = \widetilde{\phi}(\boldsymbol{\omega}, t) = \widetilde{\phi}(\boldsymbol{\omega}, 0)\exp\left(-\nu||\boldsymbol{\omega}||^2 t\right).$$

Which is the transfer function of a Gaussian filter in the Fourier space whose counterpart in the physical space is a convolution filter with Gaussian kernel. At the same time, if $\widetilde{\phi}$ is considered to be the initial condition of the evolution of $\hat{\widetilde{\phi}}(t)$, Eq. (3.3)

$$\hat{\widetilde{\phi}}(\boldsymbol{\omega}) = \frac{\widetilde{\phi}}{1 + \nu||\boldsymbol{\omega}||^2 t}$$

is an implicit Euler integration step of Eq. (3.3). In both cases, writing the results as $\hat{\widetilde{\phi}} = \widetilde{K_C}\widetilde{\phi}$, we observe that

$$\begin{aligned} &K_C \geq 0 \quad \forall\, \boldsymbol{\omega}; \\ &\forall\, \{\boldsymbol{\omega},\, \boldsymbol{\Delta\omega}\} \quad | \quad ||\boldsymbol{\omega}|| < ||\boldsymbol{\omega} + \boldsymbol{\Delta\omega}|| \Rightarrow \widetilde{K_C}(\boldsymbol{\omega} + \boldsymbol{\Delta\omega}) \leq \widetilde{K_C}(\boldsymbol{\omega}). \end{aligned} \tag{3.23}$$

Generalizing the obtained result,

$$\begin{aligned} &\frac{\hat{\widetilde{\phi}}}{\widetilde{\phi}} \geq 0 \quad \forall\, \boldsymbol{\omega}; \\ &\forall\, \{\boldsymbol{\omega},\, \boldsymbol{\Delta\omega}\} \quad | \quad ||\boldsymbol{\omega}|| < ||\boldsymbol{\omega} + \boldsymbol{\Delta\omega}|| \Rightarrow \frac{\hat{\widetilde{\phi}}}{\widetilde{\phi}}(\boldsymbol{\omega} + \boldsymbol{\Delta\omega}) \leq \frac{\hat{\widetilde{\phi}}}{\widetilde{\phi}}(\boldsymbol{\omega}). \end{aligned} \tag{3.24}$$

In the following, operators fulfilling Eq. (3.24) in the modal space are going to be considered diffusive problems in the modal space.

3.4 Other Models

The following filters are the approximations or extensions of Eq. (3.1) found in the literature. However, only Eq. (3.25) verifies all the properties of convolution filters.

3.4.1 Germano's differential filter

Germano's differential filter [2] is based on the fact that the convolution filter with

$$K_C(\boldsymbol{\xi}, a) = \frac{1}{4\pi a^2} \frac{\exp\left(-\frac{|\boldsymbol{\xi}|}{a}\right)}{|\boldsymbol{\xi}|}$$

is the extension to an unbounded domain of the Green function of

$$\phi = \left(1 - a^2 \nabla^2\right) \hat{\phi}, \tag{3.25}$$

where, $a^2 = \frac{\bar{\Delta}^2}{24}$ and $\bar{\Delta}$ stands for the filter width. The filter width is a magnitude with length dimensions related with the cut-off length in the spectral space of the low-pass filter. Thus, Eq. (3.25) defines Germano's differential filters, which are a particular case of positive, non-decreasing convolution filters.

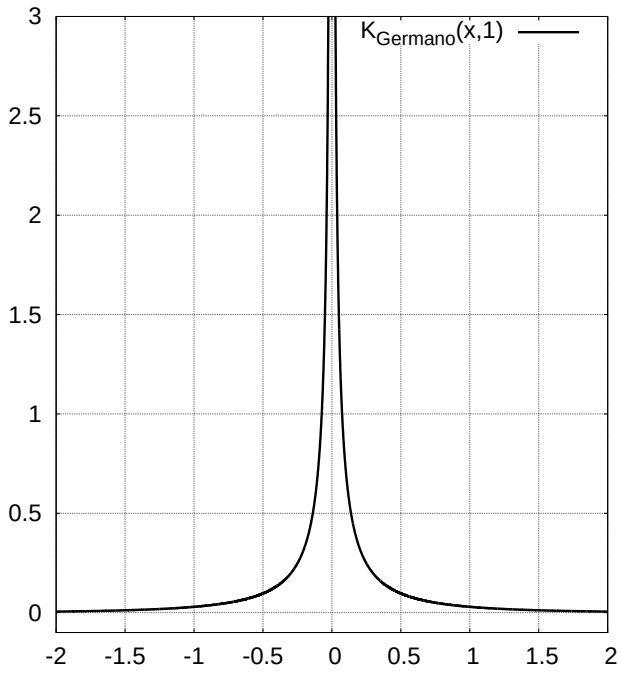

Figure 3.4: Germano's filter Kernel. It has a vertical asymptote at $\xi = 0$.

3.4.2 General kernel filters

In some situations, the filter cut-off length should vary in space. Such adaptability can be attained by means of the more general class of kernel filters:

$$\hat{\phi}(\boldsymbol{x}) = \langle \phi(\boldsymbol{\xi}) | K_G(\boldsymbol{x}, \boldsymbol{\xi}) \rangle = \int_\Omega K_G(\boldsymbol{x}, \boldsymbol{\xi}) \phi(\boldsymbol{\xi})\, d\boldsymbol{\xi}. \tag{3.26}$$

For general Kernel filters normalization does not imply conservation and vice-versa like in convolution filters. Vreman provided a good account of this fact and the

relevance of the adjoint filter in [15]. Furthermore, he showed how to construct conservative and self-adjoint filters out of normalized filters. This, as he pointed out, can be done when filter kernels are compactly supported both in $\boldsymbol{x}$ and in $\boldsymbol{\xi}$.

Another difference in the properties of this family of filters concerning convolution is that neither positivity implies TVD_1, nor positivity plus non-increasing kernels imply ED (see App. 3.B).

3.4.3 Truncated Taylor series explicit filters

If in Eq. (3.26) the filter kernel vanishes sufficiently fast, $\phi(\boldsymbol{\xi})$ near $\boldsymbol{x}$ can be locally approximated with truncated Taylor series and the filtered field can be computed from linear combination of the moments of the filter kernel function. Explicit polynomial approximations to kernel filters (see [3]) are derived with this procedure:

$$\hat{\phi}(\boldsymbol{x}) \simeq \phi(\boldsymbol{x}) + \sum_{i_1+i_2+i_3=1}^{i_1+i_2+i_3=p} \frac{\partial^p \phi}{\partial^{i_1}\xi_1 \partial^{i_2}\xi_2 \partial^{i_3}\xi_3}(\boldsymbol{x}) \frac{\int_\Omega K_G(\boldsymbol{x},\boldsymbol{\xi}) \xi_1^{i_1}\xi_2^{i_2}\xi_3^{i_3} d\boldsymbol{\xi}}{i_1! i_2! i_3!}. \tag{3.27}$$

Since convolution filters are a subset of the set of kernel filters, Eq. (3.27) can also be applied to approximate convolution filters.

Vasilyev et al. [4] and later his collaborators [16, 17] used this approximation to build commutative filters up to a certain order. This implies that all the first even moments of lower degree than the desired commutation order must vanish. Filters with vanishing even moments require their $K_G(\boldsymbol{x},\boldsymbol{\xi})$ to be non-positive. As it has been shown in section 3.2.4 , this makes this family of filters neither ED, nor TVD_1, nor GED.

When truncated Taylor series filters verify that $K_G(\boldsymbol{x},-\boldsymbol{\xi}) = K_G(\boldsymbol{x},\boldsymbol{\xi})$, all the odd moments vanish. Then, only terms with even $i_1+i_2+i_3$ remain in the right side of equation (3.27). Higher-order approximations of kernel filters improve "scales" separation [18]. However, since higher-order Taylor operators can be built by composition and linear combination of the lower-order ones, I restrict the analysis on Taylor series based filters to

$$\hat{\phi}(\boldsymbol{x}) = \left(1 + \alpha(\boldsymbol{x})\bar{\Delta}(\boldsymbol{x})^2\nabla^2\right)\phi(\boldsymbol{x}); \tag{3.28}$$

which is the expression in Sagaut [3]. A restriction on $\alpha(\boldsymbol{x})\bar{\Delta}^2(\boldsymbol{x})$ should be imposed for each ϕ^* in order to get GED. In contrast with the other filters compiled here, this diffusion-granting limitation depends on ϕ (see App 3.B for an example). Furhtermore, in Taylor filters, a ϕ^* verifying $\min(\phi^*)_\Omega \leq \hat{\phi}^* \leq \max(\phi^*)_\Omega$ is not necessarily

$TVD_1(\mathsf{F}, \phi^*)$.

Laplacian Filters

Laplacian filters [15] with anisotropic filter length read:

$$\hat{\phi}(\boldsymbol{x}) = \left(1 + \nabla \cdot \left(\mathsf{A}(\boldsymbol{x})\bar{\Delta}(\boldsymbol{x})^2 \cdot \nabla\right)\right)\phi(\boldsymbol{x}). \tag{3.29}$$

Where A is a positive semidefinite matrix. With a change on spatial cordinates $\boldsymbol{x} \to \boldsymbol{\xi}$ Eq.(3.28) is recovered (see, e.g., [19]). Consequently, Laplacian and Taylor filters are the same.

3.5 Filter Properties

The compiled properties are summarized in Table 3.1. When a filter has a property for all ϕ, it is marked as fulfilled with "Yes". When there is dependence with ϕ, then the property is marked as not fulfilled with "No". In the table, non-increasing means that the corresponding kernel verifies Eq. (3.15). Increasing means the contrary; positive means that the kernel verifies Eq. (3.11) and non-positive means the contrary.

Table 3.1: Properties and of analytical filters for CFD

Filter	Cons.	Norm.	Comm.	TVD_1	GED	ED
Positive non-inc.[a] Conv.[b]	Yes	Yes	Yes	Yes	Yes	Yes
Positive inc.[c] Conv.	Yes	Yes	Yes	Yes	Yes	No
Differential	Yes	Yes	Yes	Yes	Yes	Yes
non-Positive Conv.	Yes	Yes	Yes	No	No	No
Positive non-inc. Kernel	Yes	Yes	No	No	Yes	No
Positive inc. Kernel	Yes	Yes	No	No	Yes	No
non-Positive Kernel	Yes	Yes	No	No	No	No
Even[d] Taylor	Yes	Yes	No	No	No[e]	No
Odd[f] Taylor	Yes	Yes	No	No	No	No

[a] Non-increasing kernel.
[b] Convolution.
[c] Kernel increases with the distance to the origin at some point.
[d] Truncated Taylor series filter with even terms only.
[e] GED can not be imposed $\forall\phi$, but for each ϕ^* a limitation on F makes $\min(\phi^*)_\Omega \leq \hat{\phi}^* \leq \max(\phi^*)_\Omega$.
[f] Truncated Taylor series filter with at least one non-vanishing odd term.

3.6 Discussion

The global properties of analytical filter models that are eventually discretised and used in CFD applications have been compiled and organised. Furthermore, conditions for the fulfilment of the properties and examples and counter-examples have been provided in the appendices.

Looking at Table 3.1 it is surprising that only convolution filters with positive non-decreasing kernels (Germano's Differential filter belongs to this set) fulfill all the properties that we commonly attribute to filtering in CFD. Furthermore, all these properties are required in the derivation of LES equations from NSE (see, e.g. chapter 2 in Sagaut [14]). The diffusivity (TVD and ED) properties described here are neither enforced in Sagaut [14], nor Leonard [20], nor Pope [21], nor in most of the literature where the LES equations are derived by applying a low-pass filter to the NSE. In the following paragraphs, the convenience to require these properties to the filters in the LES deduction is discussed.

LES has two main purposes: On the one hand, LES is a mathematical model that allows providing weak solutions of NSE to study their existence and unicity properties [22]. On the other other and most widely known hand, its practical interest lies in reducing the number of necessary degrees of freedom and increasing the allowable time integration steps when performing numerical simulations of fluid flow. This more practical application was the original of the two, and was first introduced by Smagorinsky [23]. LES simulations are becoming, with the increase of computing capacity, more usually employed in the industry. When conducting numerical simulations of fluid flow, the main objective is to provide solutions with a desired level of accuracy at a low cost in a short time. Then, the mathematical consistency of the specific model put in practice is of lesser importance, specially in simulations for the industry. Very differently, mathematical consistency is fundamental in the scientific investigation of the properties of the Navier Stokes equations. Because of this, the inclusion of diffusivity in the set of properties required to the filters for LES deduction can be also attended as purpose-dependant.

In the theoretical use of LES, it is most commonly expected that all the analysis should be valid in the physical space, in the wavelengths space, and in any other variables space with bijective transform under the pertinent hypothesis ensuring convergence on ϕ. Because of this reason, when applying a filter with a set of properties in one of the possible spaces of analysis, the image of such operation should verify the images of the same set of properties in all the other spaces where LES is to be analysed. Then, the conclusions drawn in each space of study can be transferred and interpreted to the others. Regarding the diffusivity properties of filters as they have been described in section 3.2, it happens that it is not preserved when applying the Fourier transform to the box filter nor when applying the inverse Fourier transform to the spectral sharp cut-off filter. Thus, these two filters do not verify the same properties in, at least, one of the two most common spaces of study. Coletti [24] avoided this problem assuming that the filter for the derivation of LES equations is Gaussian and thus is diffusive in the both physical and the Fourier spaces (see Fig. 3.2) in a proof of existence and unicity of solutions of the LES equations.

It is not enough with the aforementioned to discard using a specific filter. However, stronger reasons for this can be found observing the behaviour of these filters in the spaces where they are not diffusive. Taking non-diffusive filters in the wavelengths space, e.g. the Fourier transform of the box filter, $\exists \omega^*$ other than 0 (the analysis is made in 1D for the sake of clarity) for which $\exists\, h > 0 \,||\widetilde{K_C}(\omega^*)| > |\widetilde{K_C}(\omega^* \pm h)|$. We would have to find a reason why that particular ω^* should not be as dumped as its neighbours and why the resulting LES equations would be a good model of the physics in the wavelengths space. All filters in the wavelengths space should tend

to zero at the infinity (we were trying to separate long wavelength from the short ones) and not affect the constant field $\widetilde{K_C}(0) = 1$. Consequently, in this space, any non-positive filter has, at least, a local maximum $|\widetilde{K_C}(\omega^*)|$ at the global minimum of $\widetilde{K_C}$. Therefore, for all non-positive filters there is, at least, a filter-dependant special wavelength ω^*. This arbitrariness to the LES model is clearly unphysical and, as I see it, invalidates, in the wavelengths space, the use of non-positive filters for the mathematical purpose of LES. Furthermore, since for this purpose of LES properties should hold independently of the space of analysis, the image in any other space of a non-diffusive filter in the wavelengths space should be discarded for the mathematical purpose.

I have not investigated the limits of how to describe diffusivity in the different usual spaces of analysis. For those interested, I think that it would be of help to understand mathematical entropy concepts (e.g. [25], [26]) and their relationship with kernel positivity. This is far out of my range of knowledge.

Focusing now on how the diffusivity properties affect the more practical numerical simulations purpose of LES, the hypothesis regarding conservation of properties in the different space of representation must be relaxed. Else, all of today's practical formulations of LES should be considered not fully consistent. For example, Finite Volumes methods lie on discretizing the domain by application of Kernel filters that, for every control volume Ω_o, read:

$$K_o(\boldsymbol{\xi}, \Omega_o) = \begin{cases} \frac{1}{V(\Omega_o)} & if \quad \boldsymbol{\xi} \in \Omega_o \\ 0 & if \quad \boldsymbol{\xi} \notin \Omega_o \end{cases} ,$$

where $V \in \mathbb{R}^+$ and $V(\Omega_o)$ is the volume of Ω_o. It results that the image of such filters in the spectral space is of non-diffusive type (see the image of the box filter in Fig. 3.1). Imposing transform-independence would not allow Finite Volumes discretizations.

After relaxing space-independence regarding diffusivity, diffusivity should nonetheless be imposed on the filter in the space where the LES equations are to be derived. In the practical purpose of LES, the ultimate goal is to reduce the amount of data needed to represent a discrete fluid magnitude in a domain and to increase the allowable time step by increasing the size of the smallest resolved flow scale, i.e., to separate small-scale phenomena from larger-scale phenomena while keeping the results within acceptable accuracy. Thus, filters for the derivation of LES with the simulation purpose should be capable of reducing the amount of data to be stored. In the spectral space, the amount of required stored data grows with the amount of

discrete wavelengths required to represent a flow, i.e., filters should be low-pass, or put otherwise, should be diffusive in this space. In the physical space, small scales are local events, i.e., local maxima and minima that increase the TV_1 of fields. Also, the number of data required to represent a field in the physical space grows with the capacity to represent TV_1. Furthermore, for a fluid in the physical space, the effect of a slight local oscillation of a fluid magnitude, does not have any remarkable effect on the evolution of the fluid at a large distance from the origin of the disturbance (see, for example, how the effect of vortices or doublets diminish with the distance in the potential flow model). In compressible flow perturbations travel at characteristic speeds and the perturbations are even more local. Hence, it seems that in the physical space filtering should be a local parabolic operation ($\mathcal{L}^1$ filter kernels) that locally smeared fields (TVD_1 and ED) instead of an elliptic operation that linked all the points of the fluid domain.

Thus, in the practical purpose, LES should be derived and executed in the same space. There, the filter used in the derivation should be diffusive. As I see it, this is often overlooked because LES equations are most commonly deduced simultaneously in the physical and in the modal space, as to show the different aspects of the model. Then, the sharp cut-off low-pass filter is introduced alongside the box filter or the Gaussian filter in the physical space (see, e.g. chapter 13 in Pope [21]). Finally, simulations with industrial interest are mostly run in discretizations of the physical space assuming that LES equations in the physical space and in the Fourier space are equivalent and drawn the conclusions exchangeable.

The reasons given here support the use of diffusive filters without prescribing any particularity on the LES sub-grid model. Vreman et al. [27] deduced that only positive filters should be used for LES models prescribing positive dissipation of turbulent kinetic energy. They also provided a numerical test that supported their theoretically derived assertion. After analyzing ED and TVD_1 in this chapter, I expand to all LES models the necessity to use diffusive filters without considering the properties of sub-grid dissipation. In the physical space, the recommendation now follows from the fact that non ED and TVD_1 operators should not be considered low-pass filters. As for filters in the modal space, those with negative or increasing transfer functions should also be avoided (see Eq. (3.24)).

These considerations are focused on the theoretical derivation of LES and the properties that filters should have for that purpose. Later, the filters with this purpose should further conditioned to force sub-grid stress Galilean invariance and some other similar properties (see, for example, Sagaut [14]). I consider them subsequent of the properties studied here and out of the scope of this thesis.

Regarding the other filter models compiled here, they are usually discretized and applied on smooth functions when brought into practical use. Then, on these functions, they most probably are Total Variations and Extrema Diminishing. Hence, in general, I think that all the filters compiled here are well fit for practical simulation purposes as long as the user is aware and respects the limitations they have. Else, one could end up creating maxima and minima, transporting energy from big scales to small scales while pretending to do the opposite or creating momentum, mass or energy.

Another remarkable conclusion of this chapter is that all the analytical filters in the CFD literature are conservative. In spite of this, it is common to find non-conservative discrete filters when explicity filtering to calculate viscous stresses in Eddy Viscosity models (see, for example, approximations for Finite Differences in [3]). Furthermore, it seems that the consequences of using non-conservative filters for such purposes have not been investigated. The use of non-conservative filters seems even more arbitrary in view of the work of Vreman in [15], where he developed a methodology to derive normalized conservative adaptive discrete filters from normalized ones.

Altogether, the filters in the theoretical derivations of LES in the physical space should verify all the properties compiled here. On the other hand, when brought to practice, discrete filters in CFD should be Normalized, Conservative, TVD_1 and ED when applied to the fields and functions of CFD, even when they would not verify them on all functions. This discards any non-positive or increasing filter kernel (Eqs.(3.11) and (3.15)). Regarding commutation, it is a necessary property for the LES derivation but it is mutually exclusive with GED in explicit Taylor filters. Hence, as I see it, filters based on explicit truncated Taylor series which eliminate commutation errors up to a certain order greater than 2 are not filters and should be avoided.

Appendix 3.A Proofs and examples of the diffusive properties of convolution filters

In the following, $\phi(\boldsymbol{x})$ or simply ϕ to denote a general function $\phi : \mathbb{R}^n \to \mathbb{R}$ and a and b positive real numbers.

Total Variations Diminishing If $TV_p(\mathsf{F}, \phi) \leq 0$ for all ϕ, then we say that F is TVD_p.

If F is a convolution filter with kernel K_C, using Young's inequality

$$||\nabla\hat{\phi}||_1 \leq ||\nabla\phi||_1 \cdot ||K_C||_1.$$

If the filter is positive, $||K_C||_1 = 1$ by virtue of normalization. Then,

$$||\nabla\hat{\phi}||_1 \leq ||\nabla\phi||_1,$$

so F is TVD_1. For non positive convolution filters like the spectral cutoff, $||K_C||_1 > 1$ and Young's inequality do not imply TVD_1.

The following example shows how the spectral cut-off filter (which is non-positive and non-$\mathcal{L}^1$) increases TV: Let

$$\phi(x) = \sin(2\pi x) + \sin(6\pi x)/9.$$

Applying the normalized spectral cut-off

$$\mathcal{F}_{spec}(\xi) = 4\frac{sin(4\pi\xi)}{4\pi\xi},$$

on it, one gets

$$\hat{\phi}(x) = \sin(2\pi x).$$

Now,

$$||\partial_x\hat{\phi}||_1 = 8\pi > ||\partial_x\phi||_1 = \frac{64}{9}\pi.$$

To check that $\mathcal{L}^1$ is not enough to ensure TVD we carry out a similar test with a $\mathcal{L}^1$, non-positive and normalised kernel. Applying the convolution filter with

$$K_C = \frac{a^2+b^2}{2b}\cos(a\xi)\exp(-b|\xi|)$$

to

$$\phi(x) = \frac{1}{a}\sin(ax)$$

one gets

$$\hat{\phi}(x) = \frac{a^2+b^2}{2b}\left(\frac{1}{b} + \frac{b}{4a^2+b^2}\right)\cos(ax).$$

With it,

$$TV_1(\mathcal{F},\phi) = \frac{a^2+b^2}{2b}\left(\frac{1}{b} + \frac{b}{4a^2+b^2}\right)\int_{-\infty}^{\infty}|\cos(ax)|dx \geq 0.$$

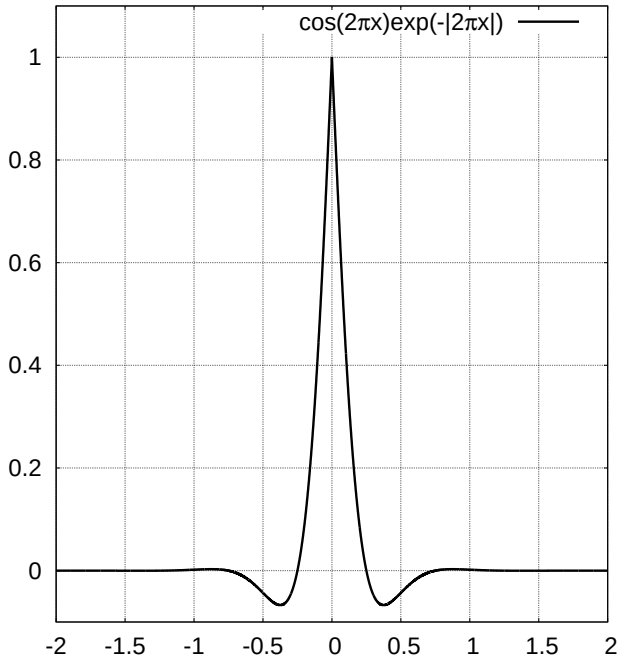

Figure 3.5: Normalized kernel filter like Eq.(3.30) with $a = 1$ and $b = 1$, $K_C(0) = 1$.

Global Extrema Diminishing Let F be a normalized convolution with positive kernel K_C. Then, suppose that $\hat{\phi}(\boldsymbol{x}^*)$ is a local maximum in the ball $B(\boldsymbol{x}^*, a)$, but $\forall\, B(\boldsymbol{x}^*, b)$ there is a $\boldsymbol{x}^{**}$ such that $\phi(\boldsymbol{x}^{**}) \geq \phi(\boldsymbol{x})\ \forall\, \boldsymbol{x} \in B(\boldsymbol{x}^*, b)$. it follows that

$$\hat{\phi}(\boldsymbol{x}) \leq \hat{\phi}(\boldsymbol{x}^*)$$

in the same ball (see [15]).

The following counter-example shows how a normalized, positive, increasing kernel, makes the number of maxima of a function grow. Consider

$$K_c(\xi) = \frac{g(\xi - a) + g(\xi + a)}{2},$$

where

$$g(\xi, \sigma) = \frac{1}{\sqrt{2\pi\sigma^2}} \exp \frac{-\xi^2}{2\sigma^2}.$$

This is, according to the definitions complied in the litterature, an allowable kernel for a convolution low-pass filter. Moreover, it is a positive kernel and, thus, the filter is TVD. Applying this filter to $g(x, \sigma)$,

$$\hat{g} = \frac{g(x-a, \sqrt{2}\sigma) + g(x+a, \sqrt{2}\sigma)}{2}.$$

The filtered Gaussian distribution has two maxima instead of one. The growth in the number of maxima or minima is a commonly undesired behavior for a low-pass filter (see Figure 3.6).

Non-positive normalized filter kernels can not be non-increasing everywhere because, after becoming negative, they should grow to vanish asymptotically. For example, applying the $\mathcal{L}^1$ filter with normalized kernel (see figure 3.5).

$$K_c = \frac{a^2 + b^2}{2b} \cos(ax) e^{-b|x|} \tag{3.30}$$

to

$$\phi = \cos(ax),$$

one obtains

$$\hat{\phi}(0) = 1 + \frac{a^2}{2b^2} > \phi(0) = 1.$$

In this case $\phi(0)$ is a global maximum and filtering increased the value of the global maximum. If the same filter is applied to the rapidly decaying

$$\phi(x) = \cos(ax) e^{-b|x|},$$

then, if $a > b\sqrt{2}$,

$$\hat{\phi}(0) = \frac{1}{4} 1 + \frac{a^2}{b^2} > 1 = \phi(0)$$

and filtering increases the value of the global maximum of the input field.

Extrema Diminishing As the Gaussian kernel is the fundamental solution of the Heat Equation and Germano's filter is the fundamental solution to Eq. (3.25), a positive non increasing kernel $K_C(\xi) = K_C(r)$ with $r = |\xi|$; $K_C \in \mathcal{C}^\infty$ is the fundamental solution to an elliptic PDE. Filtering with normalised, positive, non-increasing convolution kernel is, thus, the evolution in time of a parabolic problem. The maximum principle [28] reads that given a parabolic or elliptic PDE in a domain $D \subset \mathbb{R}^n \times [t_0, t_f]$, the extrema of all ϕ that verify the PDE are in $\partial D \times [t_0, t_f]$, i.e., the cylinder projecting the boundary of D or in $D \times t_0$.

Since the maximum principle applies to a broader class of PDE than just the Heat Equation, we can expect, at the very least, that those kernels which are Green functions of PDEs verifying the maximum principle behave similarly to the Gaussian kernel, i.e., not creating new maxima nor minima.

In computer vision, Babaud et al. [29] proved that the Gaussian kernel convolution filter is the only kernel that does not create first-order extrema (i.e. is ED) in 1D when increasing the "bandwidth", i.e. the standard deviation σ. However, to get to the proof they impose spherical symmetry, $\mathcal{C}^\infty$ and a non-zero derivative

$$\exists p > 0 \, : \, \frac{dK_C^{(2p}}{dr^{2p}} \neq 0$$

of order $2p$ at the origin. They justify the $\mathcal{C}^\infty$ requirement because any other function or distribution kernel can be arbitrarily closely approximated by linear combination of these, and as one could create a convergent series of approximations, the theorem should be valid in the limit. They, nonetheless, justify the non-zero $2p$ derivative for "technical reasons". Furthermore, it is shown that the ED property does not hold in 2D. Lindeberg [30] explained the properties of ED filters for image processing relating them to Pólya frequency functions. Also in image feature detection, Perona and Malik [31] showed that their anisotropic diffusion filtering methodology does not add maxima or minima because it belongs to a family of elliptic equations verifying the maximum principle. They, however, did not relate their method to convolution filters. In this regard, the family of ED is the family of the Green functions of the parabolic differential equations satisfying the maximum principle.

Regarding mathematical analysis, the issue of reduction of variations and extrema was addressed by Pólya in 1915 [32], defining the variations $V(\phi)$ of a 1D function as the number of zero crossings of the function. See that if ϕ was $\mathcal{C}^\infty$, the number of critical points would be exactly the number of zero-crossings of $|\boldsymbol{\nabla}\boldsymbol{\phi}|$. Later, Schoenberg in the mid 20th century [33, 34] concluded that in 1D, variation diminishing kernel filters are almost everywhere a Pólya frequency function. Schoenberg provides a counterexample to show that convolution kernels not belonging to the Pólya class are not variations diminishing in the sense of Pólya. The chosen counterexample is a box convolution filter, which is shown to increase the number of zero-crossings of a piece-wise continuous but not derivable function. If we assume that ϕ should be, at least, $\mathcal{C}^1$, we can reduce the problem of finding the conditions of ED to finding kernels that do not increase the number of zero-crossings of $\nabla\phi$. And in this case, according to Schoenberg, the conditions of ED are more strict than those provided

here. But imposing restrictions to ϕ we can maybe relax the conclusions of Schoenberg [33]. Imposing that ϕ should be $\mathcal{C}^\infty$ or, at least $\mathcal{C}^1$ agrees with the general assumptions of fluid dynamics and could open the door to box filters and similar.

In functions $\phi : \mathbb{R}^n \mapsto \mathbb{R}$ with $n > 1$, Koendernik [35] studied the behavior of extrema of differentiable functions in the space-scale in image-feature detection. The researchers in the field of image processing keep advancing in the understanding of filtering (see, e.g., [36]). However, they tend to create anisotropic diffusion equations instead of convolution kernels. For our purposes, recovering the convolution form is important in order to provide kernels that can be used to derive the LES equations. This should be addressed using functional analysis, which I am not familiar with. A functional, say E accounting for extrema and "extremity " should be built and the condition of reduction of "extremity" imposed to every kind of extremum. For example, if $\phi : \mathbb{R}^2 \mapsto \mathbb{R}$, and ϕ has a maximum plateau, *ED* should reduce the surface where ϕ is maximum. Then, the constraints on a filter F that make it *ED* should be derived from the functional. I have struggled to derive the most general *ED* property of positive, non-increasing, filters with no success. I would expect a definition more related with the concept provided in section (3.2.4) than the reduction of variations concept of Pólya. Even though a general development is not provided here, I expose some reasons that support that positive, normalised, monotonically decreasing convolution kernels are *ED* in the sense described in this work. These reasons are based on simple analysis and are not general or strong enough. This is an excessive restriction only justified by my lack of knowledge of more modern mathematics.

Take a normalized, positive convolution filter kernel $K_C(\boldsymbol{\xi})$ with more than one maximum and apply it to $\phi = K_{Gauss}(\boldsymbol{x}; \sigma)$, ϕ has only one maximum at $\boldsymbol{x} = \mathbf{0}$ and decreases monotonically with the distance to the origin. Then, when $\sigma \to 0^+$ the critical points of $\hat{\phi}$ tend to be the same as those of $K_C(\boldsymbol{\xi})$, increasing the number of maxima and minima of ϕ (see [29, 35]). Consequently, K_C should not have more than one maximum/minimum and should henceforth be weakly monotonically increasing (if $K_C(\mathbf{0}) < 0$) or decreasing with the distance from the origin in order to be *ED*. To allow normalisation, only weakly monotonic decreasing kernels should be considered. A 1D example of how a kernel with two extrema increases the number of extrema of a function is shown in Fig. 3.6. In 1D, a non-centered uni-modal filter kernel would not increase the number of extrema but would transport them. Transporting or convecting data is not among the expected result of filtering and this is why I

require the filter kernels to be weakly monotonically decreasing.

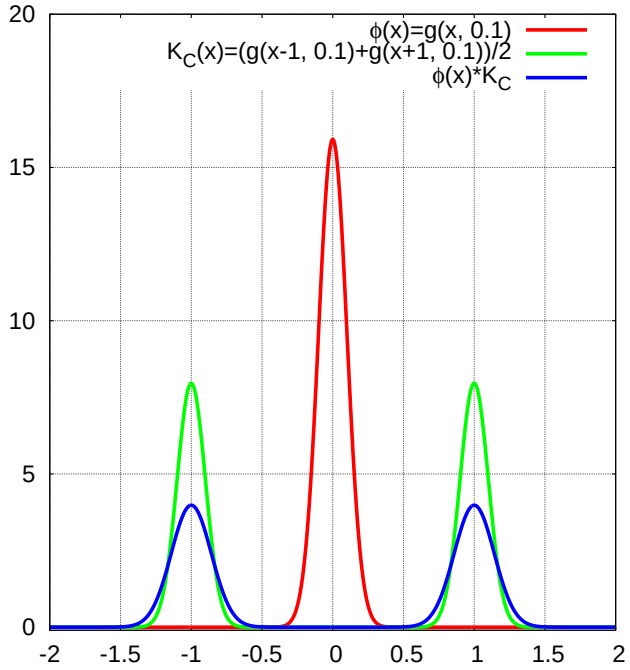

Figure 3.6: Applying the sum of 2 gaussian normalized distributions to a gaussian distributions increases the number of maxima. Yet, the convolution filter is normalized, conservative, positive, and rapidly decaying.

As it has been shown, convolution filter kernels should not have more than one extrema and should be non-increasing. Regarding saddle points $\nabla K_C(\boldsymbol{\xi}) = \mathbf{0}$ and $\exists \{\lambda_1, \lambda_2\}$ eigenvectors of the Hessian of K_C, $|H(K_C, \boldsymbol{\xi}) - \lambda I| = 0$ such that $\lambda_1 \cdot \lambda_2 < 0$. Convolution Kernels with saddle points can increase the number of saddle points of a function with only one maximum. This is straightforward from the former paragraph (take $\phi = K_{Gauss}(\boldsymbol{x}; \sigma)$ with $\sigma \to 0^+$). The extrema diminishing property should be redefined so that the only allowed process for the creation of saddle points was by reducing the number of maxima and minima. Again, this analysis is out of my capabilities and the scope of the thesis.

Requiring monotonic decrease with the distance from the unique maximum of the kernel (which should be at $\boldsymbol{\xi} = \mathbf{0}$) may seem equivalent to impose $K_C(\boldsymbol{\xi}) = K_C(|\boldsymbol{\xi}|)$. However, this last requirement is not necessary for a filter to be ED together with all the other desired properties. It seems, nonetheless, that a possible redefinition of ED taking into account what has been said regarding saddle points would lead to spherical symmetry of convolution kernels.

Appendix 3.B Proofs and examples of other models properties

3.B.1 Kernel Filters

Normalization and Conservation In Convolution filters, normalization implies conservation after Fubini's theorem. This is not generally true in the broader family of Kernel filters. These are normalized if

$$\int_{\Omega} K_G(\boldsymbol{x}, \boldsymbol{\xi}) d\boldsymbol{\xi} = 1$$

$\forall\, \boldsymbol{x}$ in Ω. Whereas the condition for conservation is

$$\int_{\Omega} K_G(\boldsymbol{x}, \boldsymbol{\xi}) d\boldsymbol{x} = 1$$

$\forall\, \boldsymbol{\xi}$ in Ω.

Total Variations Diminishing and Extrema Diminishing In Kernel filters, one might expect them to be ED or TVD when positive. The following example shows the contrary. Let

$$\phi(x) = \begin{cases} 0 & \text{if} \quad x < -a \\ 1 & \text{if} \quad -a < x < a \\ 0 & \text{if} \quad a < x \end{cases}$$

and

$$K_G(x, \xi) = \begin{cases} g(\xi - x) & \text{if} \quad x < -2a \\ g\left(\xi - (x + a)\right) & \text{if} \quad -2a < x < -a \\ g\left(\xi - (x - a)\right) & \text{if} \quad -a < x < 0 \\ g\left(\xi - (x + a)\right) & \text{if} \quad 0 < x < a \\ g\left(\xi - (x - a)\right) & \text{if} \quad a < x < 2a \\ g(\xi - x) & \text{if} \quad x > 2a \end{cases},$$

where

$$g(\xi, \sigma) = \frac{1}{\sqrt{2\pi\sigma^2}} \exp \frac{-\xi^2}{2\sigma^2}$$

is the Gaussian function for a $0 < \sigma < a$. This kernel function is conservative, rapidly decaying, normalized and positive for all (x, ξ). Yet, its effect can be to create new maxima and to increase the Total Variations (see figure 3.7). Indeed, when $\sigma \to 0^+$

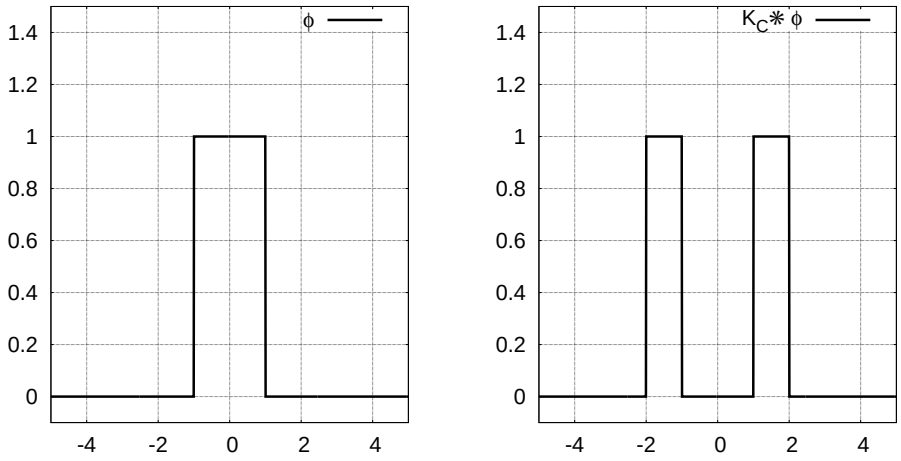

Figure 3.7: Result of filtering with a conservative and normalized positive non-increasing filter kernel. Left: ϕ, Right: $\hat{\phi}$. Filtering creates a new maximum and increases TV.

$$\hat{\phi}(x) \simeq \begin{cases} 0 & \text{if} \quad x < -2a \\ 1 & \text{if} \quad -2a < x < -a \\ 0 & \text{if} \quad -a < x < a \\ 1 & \text{if} \quad a < x < 2a \\ 0 & \text{if} \quad 2a < x \end{cases} .$$

3.B.2 Truncated Taylor series explicit filters

Taking the first and most simple Taylor filter of Eq. (3.28), and testing it on a 1D centerd Gaussian distribution

$$\phi = \frac{1}{\sqrt{2\pi\sigma^2}} \exp \frac{-x^2}{2\sigma^2}$$

it is straightforward to find:

$$\begin{aligned}
\phi' &= -\frac{x}{\sigma^2}\phi \\
\phi'' &= \left(\frac{x^2}{\sigma^4} - \frac{1}{\sigma^2}\right)\phi \\
\hat{\phi} &= \left(1 + \alpha\left(\frac{x^2}{\sigma^4} - \frac{1}{\sigma^2}\right)\right)\phi \\
\hat{\phi}' &= \left(x\left(\frac{3\alpha}{\sigma^4} - \frac{1}{\sigma^2}\right) - x^3\frac{\alpha}{\sigma^6}\right)\phi \\
\hat{\phi}'' &= \left(\left(\frac{2\alpha}{\sigma^4} - \frac{1}{\sigma^2}\right)\left(1 - \frac{x^2}{\sigma^2}\right) - \frac{\alpha}{\sigma^6}\left(3x^2 - \frac{x^4}{\sigma^2}\right)\right)\phi\,.
\end{aligned}$$

Now, the TV_1 of ϕ and $\hat{\phi}$ can be calculated.

$$TV_1(\phi) = 2\int_o^\infty \phi' dx = -2\phi\Big|_0^\infty = \frac{2}{\sqrt{2\pi\sigma^2}} \tag{3.31}$$

and $TV_1(\hat{\phi})$ depends on the values of α and σ.

$$TV_1(\hat{\phi}) = \begin{cases} \frac{2}{\sqrt{2\pi\sigma^2}}\left(1 - \frac{\alpha}{\sigma^2}\right) & \text{if} \quad \sigma^2 \geq 3\alpha \\ \frac{2}{\sqrt{2\pi\sigma^2}}\left(\frac{\alpha}{\sigma^2} - 1 + \frac{4\alpha}{\sigma^2}\exp\left(\frac{\sigma^2}{2\alpha} - \frac{3}{2}\right)\right) & \text{if} \quad \sigma^2 < 3\alpha \end{cases} \tag{3.32}$$

Total Variations Diminishing . Hence, $TV_1(\hat{\phi}) < TV_1(\phi)$ if $\sigma^2 = 4\alpha$ and $TV_1(\hat{\phi}) > TV_1(\phi)$ if $\sigma^2 = 2\alpha$. This example shows that the Taylor filter, and by extension the Taylor series based filters, are not TVD_1 but they reduce TV_1 of some ϕ functions. Another possibility would be to allow the filter parameter α to depend on ϕ to force TVD_1. Then, successive filtering with limited values of alpha $\alpha_i(\hat{\phi}^{(n)})$ could be applied until $\sum_i \alpha_i = \alpha$. Then filtering would be equivalent to resolving the heat equation. This is out of the scope of the definitions of filters found in the literature.

Extrema Diminishing Regarding ED, with the same ϕ function, $\hat{\phi}$ has 3 critical points instead of only one maximum if $\sigma^2 < 3\alpha$. These 3 critical points are a minimum at $x = 0$ and two new maxima at symmetrical positions each side of the minimum, and the filter is not ED. However, when $\sigma^2 > 3\alpha$ the filter is ED as it does not create new maxima or minima and it reduces the existing maxima.

References

[1] R.S. Rogallo and P. Moin. Numerical simulation of turbulent flows. *Annual Review of Fluid Mechanics*, 16:99–137, 1984.

[2] M. Germano. Differential filters for the large eddy numerical simulation of turbulent flows. *Physics of Fluids*, 29:1755, 1986.

[3] P. Sagaut and R. Grohens. Discrete filters for large eddy simulation. *International Journal for Numerical Methods in Fluids*, 31(1997):1195–1220, 1999.

[4] O.V. Vasilyev, T.S. Lund, and P. Moin. A general class of commutative filters for LES in complex geometries. *Journal of Computational Physics*, 146:82–104, 1998.

[5] M. Germano, U. P., P. Moin, and W. H. Cabot. A dynamic subgrid-scale eddy viscosity model. *Physics of Fluids A: Fluid Dynamics*, 3(7):1760–1765, 1991.

[6] Noma Park, Sungwon Lee, Jungil Lee, and Haecheon Choi. A dynamic subgrid-scale eddy viscosity model with a global model coefficient. *Physics of Fluids*, 18(12):125109, 2006.

[7] T.J.R. Hughes, L. Mazzei, and K.E. Jansen. Large Eddy Simulation and the variational multiscale method. *Computing and Visualization in Science*, 3:47–59, 2000.

[8] C. Bogey, N. de Cacqueray, and C. Bailly. A shock-capturing methodology based on adaptative spatial filtering for high-order non-linear computations. *Journal of Computational Physics*, 228(5):1447–1465, 2009.

[9] B. Engquist, P. Lotstedt, and B. Sjogreen. Nonlinear filters for efficient shock computation. 52(186):509–537, 1989.

[10] W Shyy, M-H Chen, R Mittal, and HS Udaykumar. On the suppression of numerical oscillations using a non-linear filter. *Journal of Computational Physics*, 102(1):49–62, 1992.

[11] R. Mittal and G. Iaccarino. Immersed Boundary Methods. *Annual Review of Fluid Mechanics*, 37:239–261, 2005.

[12] M. Calaf, C. Meneveau, and J. Meyers. Large eddy simulation study of fully developed wind-turbine array boundary layers. *Physics of Fluids*, 22(2010):015110, 2010.

[13] A. P. Witkin. Scale-space filtering. *International Joint Conference on Artificial Intelligence*, 2:1019–1022, 1983.

[14] P. Sagaut. *Large eddy simulation for incompressible flows: an introduction*. Springer Science & Business Media, New York, 2006.

[15] A. W. Vreman. The adjoint filter operator in large-eddy simulation of turbulent flow. *Physics of Fluids*, 16(6):2012–2022, 2004.

[16] A. L. Marsden, O. V. Vasilyev, and P. Moin. Construction of Commutative Filters for LES on Unstructured Meshes. *Journal of Computational Physics*, 175:584–603, 2002.

[17] A. Haselbacher and O. V. Vasilyev. Commutative discrete filtering on unstructured grids based on least-squares techniques. *Journal of Computational Physics*, 187(1):197–211, 2003.

[18] J. S. Mullen and P. F. Fischer. Filtering techniques for complex geometry fluid flows. *Communications in Numerical Methods in Engineering*, 15:9–18, 1999.

[19] R. Aris. *Vectors, Tensors, and the Basic Equations of Fluid Mechanics*. Prentice-Hall, Englewood Cliffs, NJ, 1962.

[20] A Leonard. Energy cascade in large eddy simulations of turbulent fluid flows. *Adv. Geophys.*, 18(A):237–248, 1974.

[21] S. B. Pope. *Turbulent Flows*. Cambridge University Press, Cambridge, 2000.

[22] O. A. Ladyzhenskaya. *The mathematical theory of viscous incompressible flow*. Gordon and Breach, New York, 1969.

[23] J. Smagorinsky. General circulation experiments with the primitive equations: I. the basic experiment. *Monthly weather review*, 91(3):99–164, 1963.

[24] P. Coletti. A global existence theorem for large eddy simulation turbulence model. *Mathematical Models and Methods in Applied Sciences*, 7(05):579–591, 1997.

[25] I.I. Hirschman. A note on Entropy. *American Journal of Mathematics*, 79(1):152–156, 1957.

[26] R. A. Fefferman. A theory of entropy in Fourier analysis. *Advances in Mathematics*, 30(3):171–201, 1978.

[27] B. Vreman, B. Geurts, and H. Kuerten. Realizability conditions for the turbulent stress tensor in large-eddy simulation. *Journal of Fluid Mechanics*, 278:351, 1994.

[28] P. Pucci and J. Serrin. The strong maximum principle revisited. *Journal of Differential Equations*, 196(1):1–66, 2004.

[29] J. Babaud, A. P. Witkin, M. Baudin, and R. O. Duda. Uniqueness of the Gaussian Kernel for Scale-Space Filterng. *IEEE Transactions on Pattern Analysis and Machine Intelligence*, PAMI-8(1):26–33, 1986.

[30] T. Lindeberg. Scale-Space for Discrete Signals. *IEEE Transactions on Pattern Analysis and Machine Intelligence*, 12(3):234–254, 1990.

[31] P. Perona and J. Malik. Scale-space and edge detection using anisotropic diffusion. *IEEE Transactions on Pattern Analysis and Machine Intelligence*, 12(7):629–639, 1990.

[32] G. Pólya. Algebraische Untersuchungen über ganze Funktionen vom Geschlechte Null und Eins. *Journal für die reine und angewandte Mathematik*, 145:224–249, 1915.

[33] I. J. Schoenberg. On variation-diminishing integral operators of the convolution type. *Proc Natl Acad Sci U S A*, 34(4):164–169, 1948.

[34] I. J. Schoenberg. On Smoothing Operations and Their Generating Functions. *Bulletin of the American Mathematical Society*, 59(3):199–230, 1953.

[35] J. J. Koenderink. The structure of images. *Biological Cybernetics*, 50(5):363–370, 1984.

[36] J. Weickert. Anisotropic diffusion in image processing. *Image Rochester NY*, 256(3):170, 1998.

4

Discrete Explicit Filters for CFD

4.1 Note

The contents of this chapter have been published in [1].

4.2 Introduction

The Navier-Stokes Equations (NSE) form a system of Partial Differential Equations that describes the conservation of momentum, mass and energy of a Newtonian fluid using the Eulerian formulation. Even though they were formulated over 150 years ago, NSE are still a formidable mathematical problem for which analytical solutions have been found for some simple cases only. For the vast majority of scientific or engineering problems involving fluids, empirical data or simulations results are required.

CFD is the branch of Fluid Dynamics that produces and studies the algorithms needed to numerically simulate problems involving fluid flow. Due to Kolmogorov's power law of the turbulent flow spectrum, the full resolution of most of the fluid flow problems requires unaffordable computational resources and computation times. Modeling the smallest turbulent flow scales can reduce the required computational resource and make problems affordable. Nevertheless, as the computer resource required for CFD is still large, algorithms must be efficient to allow the most accurate simulations of the most complex problems in the shortest possible time for a given

computer capacity.

Among the common operations of CFD, we focus on filtering fields on non-uniform discrete spatial domains. In this paper we gather the essential properties of this operation in the continuous field and propose constraints to transfer them to filters in discrete spaces. Spatial filtering is also common in other fields of science and technology. However doing it on non-uniform spatial domains (unstructured meshes) is very particular of CFD, so alien literature does not directly apply.

The use of spatial filtering operations on CFD has several objectives. The most important and known use of filters in CFD is filtering the NSE to obtain the Large Eddy Simulations (LES) equations [2]. This is a rather theoretical use for which filters should be low-pass, linear, normalized and commutative with differentiation. Convolution filters match these properties. In practice, LES is not often performed with explicit filtering as it is assumed that discrete differential operators have a filtering effect [2] and eliminating explicit filtering reduces computation effort. Since the computation cost of convolution filters would make explicitly filtered LES unaffordable for most of the flows of interest and implicitly filtered LES has been reported [3] to be inconsistent with the filtered NSE, alternatives to convolution filters have been investigated. One of the main difficulties when designing appropriate filters for explicit LES is that if the simulated turbulent flow is inhomogeneous and thus is the mesh, the error due to commutation between discrete filtering and differential operators can become harmful. Ghosal and Moin [4] elaborated a theory to estimate such error on non-uniform meshes and later Vasilyev et al. [5] proposed a method based on the cancellation of the filter kernel moments to derive filters that can reduce commutation error to any order desired. Based on the same theory, methods to construct filters with similar characteristics on unstructured meshes were more recently proposed [6, 7]. Even though this family of filters is shown to fulfill the commutation error reduction goal, the transfer fictions are greater than 1 [5] for some wave scales when their stencils are not symmetric and their transfer function is not positive if the order of the commutation error is greater than 2. Henceforth, reducing commutation error to less than second order results on the not fulfillment of all the realizability conditions of Vreman et al. [8]. Yet, this does not mean commutation errors reducing filters should not be used, it means that the high-order ones should not be used in conjunction with subgrid-scale models prescribing the generalized turbulent kinetic energy defined in [9] to be positive. After these considerations, up to the date and to our knowledge, there are no discrete filters able to reproduce all the properties of convolution filters with a reasonable computational cost and thus allowing for a totally consistent discretization of the LES equations with explicit filtering in the literature.

Another well-known context in which filters are used in CFD is the calculation of closures in simulations of turbulent flow with sub-grid scales models like the dynamical procedure [10], the global dynamical procedure [11, 12] or the variational multi-scale methodology [13]. These are widely employed techniques in which the filter performance has a noticeable influence on the overall results but where commutation errors do not play the important role described in the preceding paragraph. In this context, for example, the top hat filter is used to compare subgid scales models on a turbulent mixing layer flow in Vreman et al. [14]. Still in LES, spatial filters are also used in regularization models [15, 16], where filters should verify [17] specific properties.

Filters are also commonly employed in simulations with steep body forces. In these cases, filtering is used to prevent the growth of wiggles produced by large body force gradients [18, 19]. Filtering is also used for similar reasons on simulations of compressible flow with shock waves [20].

In practice, most of the current CFD discrete spatial filtering technology derives from the work of Germano [21],where a convolution filter kernel is found to be the Green function of a second order differential equation and the fundamentals to approximate other low-pass convolution-based filters (e.g. the Gaussian filter) by means of the solution of differential elliptic equations on filtered fields $\hat{\phi}$ are set. This enables computationally affordable approximations to convolution filters in a discrete variables framework, but the resolution of an implicit system of linear equations is required to obtain discrete filtered fields $\hat{\boldsymbol{\phi}}$ from the unfiltered ones $\boldsymbol{\phi}$. Sagaut and Grohens [22] applied filter kernels to Taylor approximations of the unfiltered fields to construct explicit discrete filters for arbitrary meshes. These filters were compared to their theoretical continuous equivalents and tested both on ideal von Karman spectra and within 3D eddy-viscosity LES. Results showed that filter parameters remarkably affect LES results. Vreman et al. [8] approached filters for LES from the models properties. It was shown that only positive filters achieve turbulent sub-grid tensors that always reduce kinetic energy. Vreman [23] later demonstrated that normalized conservative filters can be constructed on non-uniform meshes. To do this, he showed that the adjoint operators of normalized filters are conservative and vice versa. Then, he provided a formula to construct conservative and self adjoint operators from normalized ones and announced two smoothing properties of filters: kinetic energy dissipation and global extrema reduction. More recently, Trias et al. [16] constructed discrete explicit filters fitted for regularization models. In the field of compressible flow simulations, Engquist et al. [24] developed and tested a non-linear filter methodology to capture shocks with conservative adaptative filters

and provided a proof of convergence to the weak solution of the original Euler equations. However, the constructed non-linear solution-depending filters entangle filtering and the wiggle detection problem; adding complexity and increasing filter computation time. Also in the compressible flows field, Bogey et al. [20] used a high-order conservative filter to avoid wiggles growth and an adaptative conservative second-order filter at the shock waves. With it, they simulated shock-vortex interactions and shown the capabilities of this methodology to resolve computational aeroacoustics problems. From the results, it is seen that the adaptative filter does not affect low frequency scales on 1D problems on uniformly spaced structured meshes.

The authors notice that there is, in the literature, a wide range of applications for which the properties that filters should verify to be well fitted for differs. Analytical convolution filters are appropriate for all purposes requiring a constant filter width. However, for analytical or discrete filters approximating the effect of convolution filters, some of its properties are mutually exclusive or lost. For example, adaptative kernel filters do not exactly commute with differentiation. Then, depending on the application, discrete filters in the literature have different properties. As there is no agreement about a minimum set of properties that discrete filters should satisfy in order to be considered filters, there is also confusion about if a discrete operator is really a filter or not. For example, in Finite Volumes (FV) simulations with steep volumes size variations, some of the existing filters can locally "sharpen" fields.

The main objectives of this work are identifying the main properties of filtering, defining discrete filters as operators in concordance with them and providing constraints ensuring their fulfillment. The reader will notice that we neither consider local accuracy to continuous operators a fundamental property of discrete filters nor suppose any set of governing flow equations. This is because the accent is put on bringing the global properties of analytic filtering to discrete spaces and not to any specific application described above. From our point of view, once a spatial discretization is performed, discrete properties of the discrete operators, filters among them, should be derived and/or accomplished in the discrete space. Continuous properties of continuous operators should be translated into discrete properties of discrete operators and not to discrete approximations to continuous operators for which some continuous property is true. Of course, local errors due to discretization are important on simulations that reproduce continuous physics. But as has been shown by Verstappen and Veldman [25], Rozema et al. [26], Trias et al. [27] and other authors, preserving operator symmetries rather than making good local approximations can lead to important improvements and better understanding of physics in the CFD science. Using these methods has enabled a better understanding of the physics of fluid flow. For example, Lehmkuhl et al. put them in practice in [28] and

captured a low frequency phenomenon affecting a Laminar Separation Bubble (LSB) at the limit layer of a circular cylinder under uniform flow at Reynolds number 3900. The LSB phenomenon is correlated to two different near-wake modes leading to scattering of the results in the literature. Such low-frequency phenomena are sensitive to the numerical discretization to the point that only non dissipative methods can capture them with reasonable mesh refinements.

To reach our purposes, in section 4.3 we first discuss the analytical convolution filter and its properties. Then, other analytical models of filters are gathered. In the same section, the constraints that make discrete spatial filters satisfy the properties of the convolution filter are detailed. Among the properties, local extrema and total variations evolutions are studied alongside with entropy consistency. Their accomplishment leads to restrictions on local filter strength (filter width). After that, three filters respecting the imposed constraints are presented in Section 4.4. In Section 4.5 it is tested if the proposed filters together with some of the existing in the literature satisfy the aforementioned properties. This is done by means of the eigenvectors of the graph Laplacian matrix that is introduced in Section 4.3. Tests regarding spatial accuracy are carried out on a singularity field and on an isentropic vortex. Finally, conclusions and possible extensions of the present work are provided in Section 4.6.

4.3 Conditions for Adaptive Filtering

For the rest of the document, we use sans serif capital letters to denote matrices, bold letters to denote vectors and calligraphic letters to denote operators. The hat symbol is used to denote filtered field. Plain letters denote scalars. With this, $\hat{\phi}(\boldsymbol{x}) = \mathcal{F}(\phi(\boldsymbol{x}))$ and $\hat{\boldsymbol{\phi}} = \mathsf{F}\boldsymbol{\phi}$. Elements of arrays relative to the control volumes are identified with subscripts "o", "p" and "q" . Elements of matrices establishing relationships between arrays relative to control volumes are identified with two separated subscript indexes "$o\,p$" and the element of the oth row and pth column of a F matrix is denoted with the matrice's letter in minuscule ,i.e., $f_{o\,p}$. Elements of arrays corresponding to interfaces between control volumes are identified with the underlined letters "$\underline{op}$" of the two adjacent control volumes. This notation, together with other symbols $\overline{\text{whose}}$ meaning will be described at first appearance, is used for the rest of the document.

4.3.1 The Analytical Convolution Filter

Most of the theory on filters for CFD has been derived as a part of the LES theory, where filtering is generally approximated as a convolution operation. Following the

notation used in [29]:

$$\hat{\phi}(\boldsymbol{x}) = G * \phi(\boldsymbol{x}) = \int_{\Omega} K_C(\boldsymbol{x} - \boldsymbol{\xi})\phi(\boldsymbol{\xi})\, d\boldsymbol{\xi}, \tag{4.1}$$

where ϕ is a generic function, K_C is the filter kernel and is related to the cutoff scales (characteristic of the filter) through a filter characteristic width. The kernel functions K_C of convolution filters are compact supported or rapidly decaying and normalized, i.e. $\int_{\Omega} K_C(\boldsymbol{\xi})\, d\boldsymbol{\xi} = 1$. Normalization and conservation, i.e. $\int_{\Omega} \phi\, d\boldsymbol{\xi} = \int_{\Omega} \hat{\phi}\, d\boldsymbol{\xi}$ are equivalent for convolution operators. Moreover, these filters commute with differentiation and are not dispersive. Additionally, convolution filters can smoothen fields, i.e. be dissipative. This last point is disputed because filtering can also be regarded in the sense of eliminating high Fourier frequencies. Taking into account the applications of filters in CFD and considering that the dissipative property is necessary to smoothen sharp fields, it is not contrary to the LES model and it is in agreement with the realizability conditions in [8], we conclude that dissipation is a commonly necessary property of filters for CFD. Unfortunately, dissipation is not always measured in the same way and, thus, some operators can be considered dissipative according to one criterion while they are not according to another. To us, dissipating is equivalent to reducing a norm on a field gradient and avoiding growth of local maxima and decrease of local minima. If "local" means a ball of radius the support of K_C, normalized positive, i.e. $K_C \geq 0$, filters with compact support verify the first property for all bounded test functions (see [23]). If the filter kernel is not compact supported, the accomplishment of the first property depends on the test functions. For the second property we use the Total Variations Diminishing on the p norm (TVD_p) criterion to quantify the reduction of gradient norm:

Taking the p norm $||\cdot||_p$ of a function ϕ

$$||\phi||_p = \left(\int_{\Omega} |\phi|^p d\xi \right)^{1/p}, \tag{4.2}$$

assuming that $\nabla\phi$ exists and $|\nabla\phi|$ is bounded (this is true for fluid magnitudes), the Total Variations of order p (TV_p) o an operator $\mathcal{F}$ on ϕ is defined as

$$TV_p(\mathcal{F}, \phi) = ||\nabla\mathcal{F}(\phi)||_p - ||\nabla\phi||_p. \tag{4.3}$$

If $TV_p(\mathcal{F}, \phi) \leq 0$ for all ϕ, then we say that $\mathcal{F}$ is TVD_p. If $\mathcal{F}$ is a convolution filter with kernel K_C, using Young's inequality $||\nabla\hat{\phi}||_1 \leq ||\nabla\phi||_1 \cdot ||K_C||_1$. If the filter is positive, $||K_C||_1 = 1$ by virtue of normalization. Then, $||\nabla\hat{\phi}||_1 \leq ||\nabla\phi||_1$, so $\mathcal{F}$ is TVD_1. For non positive convolution filters like the spectral cutoff, $||K_C||_1 > 1$ and Young's inequality does not imply TVD_1.

4.3.2 Other Analytical Filter Models

The following analytical filter models (4.4-4.8) justify discrete approximations of (4.1) in the literature. However, they do not fulfill all of its properties, e.g. commutation with differentiation is lost in all of them. A detailed analysis of all the properties of each model is out the scope of this paper and is not carried out here. They are included to allow for a smooth and more comprehensible transition from (4.1) to the discrete filters.

The differential filter described in Germano [21] is defined by

$$\phi = (1 - \frac{\bar{\Delta}^2}{24}\nabla^2)\hat{\phi}, \tag{4.4}$$

where $\bar{\Delta}$ is the filter width. It corresponds to (4.1) if an exponential filter kernel is used. Using (4.4) is, for simulations with a large number of nodes, less computationally costly than using (4.1).

In some cases, the filter cutoff length should vary in space or according to some dependence on the simulated evolving flow. Such adaptability can be obtained by means of the more general class of kernel filters:

$$\hat{\phi}(\boldsymbol{x}) = \int_\Omega K_G(\boldsymbol{x}, \boldsymbol{\xi})\phi(\boldsymbol{\xi})\, d\boldsymbol{\xi}. \tag{4.5}$$

If the filter kernel vanishes sufficiently fast, (4.5) can be locally approximated taking truncated Taylor series of $\phi(\boldsymbol{\xi})$ near $\boldsymbol{x}$.Thus, one gets explicit polynomial approximations to kernel filters (see [22]):

$$\hat{\phi}(\boldsymbol{x}) \simeq \phi(\boldsymbol{x}) + \sum_{i_1+i_2+i_3=1}^{i_1+i_2+i_3=p} \frac{\partial^p \phi}{\partial^{i_1}\xi_1 \partial^{i_2}\xi_2 \partial^{i_3}\xi_3}(\boldsymbol{x}) \frac{\int_\Omega K_G(\boldsymbol{x}, \boldsymbol{\xi}) \xi_1^{i_1} \xi_2^{i_2} \xi_3^{i_3} d\boldsymbol{\xi}}{i_1! i_2! i_3!}. \tag{4.6}$$

As convolution filters are a subspace of kernel filters, (4.6) can also be applied to approximate those. It is common in all the models considered so far to take filter kernels with vanishing odd moments. Then, only elements with even $i_1 + i_2 + i_3$ remain in (4.6). In such case, higher-order differential approximations improve "scales" separation (the scales concept is developed in Section 4.3.8) as it is shown in [30]. However, as higher-order differential operators can be built by composition and linear combination of the second-order ones, we restrict our analysis on differential filters to those of second order. Thus,

$$\hat{\phi}(\boldsymbol{x}) = (1 + \left(\mathsf{A}(\boldsymbol{x})\bar{\Delta}(\boldsymbol{x})^2\nabla^2\right))\phi(\boldsymbol{x}). \tag{4.7}$$

When $\mathsf{A} \succeq 0$, i.e., it is a positive semidefinite matrix, and $\mathsf{A}(\boldsymbol{x})\bar{\Delta}^2(\boldsymbol{x})$ is limited to take into account the 2nd law of thermodynamics, this model can be regarded as a time integration step of an unsteady heat conduction problem in an anisotropic material. For the heat conduction problem, moduli of gradients of ϕ should be reduced. This is in accordance with the realizability condition on the convolution filters in [8], with what has been discussed above about the dissipation property of convolution filters for CFD and in consonance with a remark about the differential model (4.4) in [21]:"we notice that the Gaussian filter corresponds in some sense to a diffusive process of the original function (...)". In the case of (4.7) the limitation on $\mathsf{A}(\boldsymbol{x})\bar{\Delta}^2$ that makes the filter diffusive depends on the values taken by the second derivatives of ϕ or, in other words, (4.7) is conditionally diffusive. This contrasts with the fact that positive convolution filters (4.1) are dissipative for all ϕ. Moreover, "Germano's" differential filter (4.4) can not be written in the form of (4.7) and is therefore essentially different from these. "Germano's" differential filters are inconditionally diffusive because they are equal to (4.1) with exponential positive kernels.

For isotropic filters or meshes, Equation (4.7) reduces to

$$\hat{\phi}(\boldsymbol{x}) = (1 + \left(\alpha(\boldsymbol{x})\bar{\Delta}(\boldsymbol{x})^2\nabla^2\right))\phi(\boldsymbol{x}) \tag{4.8}$$

and the approximation described in Sagaut [22] is recovered. Again, a restriction on $\alpha(\boldsymbol{x})\bar{\Delta}^2(\boldsymbol{x})$ should be imposed for the sake of consistency with the 2nd law of thermodynamics.

Filters based on (4.1) can separate scales of a field better than those based on (4.4), (4.6), (4.7) or (4.8). The last three models introduce diffusion to all scales but are more flexible on complex geometries and can be easily applied on both structured and unstructured meshes. On account of this reason and the fact that higher-order filters with better scale separations properties can be built from them, in the following we study discrete versions of (4.7) and (4.8).

4.3.3 Discrete Filter Properties

Let $\mathcal{F}(\cdot) : \mathbb{R}^n \mapsto \mathbb{R}^n$ be a discrete filtering operation with $\hat{\boldsymbol{\phi}} = \mathcal{F}(\boldsymbol{\phi})$. Then, for all $\boldsymbol{\phi}$ and depending on its application, the following properties derived from the approximations (4.7) and (4.8) of (4.1) are usually required:

P-1 Filtering is a local, linear and explicit operation.

P-2 Normalization: Filters do not alter constant fields. $\mathcal{F}(\mathbf{1}) = \mathbf{1}$.

P-3 Conservation: Filtering preserves the integral of $\boldsymbol{\phi}$ on its domain.

P-4 Variations reduction: Filters reduce variations, maxima and/or minima.

P-5 Low dispersion between modes of a mesh.

From the above properties, it is remarkable that 4.3.3, 3.2.4, and 4.3.3 apply to all situations and are intimately related to the continuous concept of low-pass filter while 4.3.3 and 4.3.3 depend on the filter purpose. For example, conservation is not regarded as strictly necessary on test filters of dynamic eddy-viscosity models and low dispersion is not wanted for filters on steep gradient forces, where filtering is performed to transport magnitudes from "small scales" to "larger scales" of meshes.

In the following paragraphs, we explain each property and observe its consequences. We focus our analysis on FV discretizations, extensions to FD or Finite Elements Methods (FEM) are straightforward.

4.3.4 Filtering is a local, linear and explicit operation [4.3.3]

Filtering is not a main operation of the NSE, it appears as a CFD tool. Hence, for computer performance and analysis simplicity reasons, and according to the analytic convolution filter and all the other filter models of Section 4.3.2, linear explicit filters are preferred to others. Then, $\hat{\boldsymbol{\phi}} = \mathsf{F}\boldsymbol{\phi}$.

Since the differential operators of Equations (4.7) and (4.8) are local and have compact domains, and for computer performance reasons, filter matrices should be sparse. Accordingly, $f_{o\,p} = 0$ except for $p \in N_o = \{p_1, p_2, ..., p_m\}$ neighborhood of the o_{th} cell or for $p = o$. This property also corresponds to models of Equations (4.1) and (4.5) with compactly supported kernels.

4.3.5 Normalization: Filters do not alter constant fields [4.3.3]

In agreement with the analytical models and because other possibilities do not seem to have any interest for CFD, linear explicit filters should obey

$$(\mathsf{F} - \mathsf{I})\mathbf{1} = \mathbf{0}. \tag{4.9}$$

In such case, we say that the filter is normalized.

4.3.6 Conservation [4.3.3]

Conservation is the basic principle from which the NSE are derived and the main reason why in some applications FV discretizations are preferred over other possibilities such as FD or FEM. In some simulations, magnitudes affected by conservation equations are filtered to improve stability and/or avoid wiggles. Then, they should be conserved in order to preserve the overall method physics. For example, when filtering the body forces applied at some control volumes by an actuator line model of a turbine on a simulation of wind turbine wakes [31], non conservative filters lead to an imbalance between the turbine model power extraction and the energy change in the free stream. Conservation

$$\int_\Omega \hat{\phi}\, \delta\Omega = \int_\Omega \phi\, \delta\Omega \tag{4.10}$$

is true for analytical convolution filters and models (4.7) and (4.8).

Defining Ω as the diagonal matrix with the cell volumes at the diagonal elements, one gets the discrete version of (4.10):

$$\mathbf{1}^T \Omega \hat{\boldsymbol{\phi}} = \mathbf{1}^T \Omega \mathsf{F} \boldsymbol{\phi} = \mathbf{1}^T \Omega \boldsymbol{\phi} \tag{4.11}$$

Thus,

$$f_{o\,p} = \frac{\Omega_p}{\Omega_o} f_{p\,o} \tag{4.12}$$

This can also be written as

$$\Omega \mathsf{F} = (\Omega \mathsf{F})^T \tag{4.13}$$

Notice that the volumes of two neighbor cells are not necessarily equal on general meshes ($\Omega_o \neq \Omega_p$). Hence, for conservative filters $f_{o\,p} \neq f_{p\,o}$ at non-diagonal elements. Consequently, filter matrices have a skew-symmetric part and transport energy between "scales" of the mesh.

Conservation can be relaxed in some applications and non-conservative filters are also useful. For example, test filters used in eddy viscosity methods are not necessarily conservative to keep overall method conservation properties. Among non-conservative filters, the symmetric ones $\mathsf{F} = \mathsf{F}^T$ attract special attention because the aforementioned transport is avoided.

4.3.7 Variations reduction [4.3.3]

Roughly speaking, filtering aims at the smearing of maxima and minima and the reduction of variations. This feature has been already discussed for the analytical

filters considered in this work and should be imposed on discrete filters by means of an appropriate condition. However, to the best of our knowledge, there is not a clear general consensus about what is the exact computationally affordable condition that represents smearing of discrete fields. We also have noted that not all filters in the literature necessarily fulfill this property for all input fields. For example, the conservative filters introduced in [20] are shown to damp over a range of wavelengths but their behavior on singularity fields, i.e. fields vanishing at all cells excepting one, is not considered. Next, various variations reduction alternatives are discussed.

Local Extrema Diminishing

Local Extrema Diminishing (LED) ensures that if at a certain point $\phi_o > \phi_p \quad \forall p \in N_o$, after filtering: $\hat{\phi_o} = \phi_o + \sum f_{o\,p}(\phi_p - \phi_o) < \phi_o$. Changing the directions of inequalities, the same is true for minima. In the literature, LED is often assumed for all meshes and for all input fields because all $f_{o\,p}$ are commonly positive by construction. For normalized filters, the necessary and sufficient conditions to fulfill this property are (see [32] and [8]):

$$f_{o\,p} \geq 0 \quad \forall o\, p \tag{4.14}$$

and

$$f_{o\,o} = 1 - \sum_{p \in N_o} f_{o\,p} \geq 0 \quad \forall o. \tag{4.15}$$

LED is more restrictive than a bound on the $\mathcal{L}^\infty$ norm of fields. However, in the case of adaptative filtering with filters driven by complex combinations of variables or in the case of non-uniform meshes, LED is not restrictive enough and does not necessarily prevent filters from generating new extrema. Filters that can generate new extrema are not consistent discretizations of the physically consistent analytical models. To illustrate this, we provide the following example:

On the irregular 1D depicted in Figure 4.1, the volume of i is 1 while the volume of all the other cells is $\omega < 1$. A $\boldsymbol{\phi}$ field evaluating $\phi_i = 1$, and 0 elsewhere is filtered with a one-neighbor stencil LED conservative filter. Since the filter is conservative, according to (4.12), the values of the filtered field are $\hat{\phi}_i = 1 - 2f$, $\hat{\phi}_{i\pm1} = f/\omega$ and $\hat{\phi}_q = 0$ for other cells, where the scalar f is the filter strength parameter. LED (4.14), (4.15) imposes $f \geq 0, 1 - 2f \geq 0$ and $1 - f/\omega \geq 0$. Then, $0 \leq f \leq min(1/2, \omega)$.

With $\omega = 0.25$ as in the figure, for example, the maximum f allowed by LED is $f = 0.25$. Using it, the values of the filtered field are $\hat{\phi}_i = 0.5$ and $\hat{\phi}_{i\pm1} = 1$. In such case, $\hat{\phi}_{i\pm1} > \hat{\phi}_i$, so the filter would increase the number of maxima (2 after filtering 1 before filtering). This result would break the heat equation interpretation

of (4.8) and (4.7). For consistency with the 2nd law of thermodynamics, we impose $\hat{\phi}_i \geq \hat{\phi}_{i\pm1}$. Then, the condition $1 - 2f \geq f/\omega$ is obtained, so $0 \leq f \geq \omega/(2\omega + 1) > min(1/2, \omega)$. Unfortunately, the initial field had to be known prior to establishing the inequality direction of $\hat{\phi}_i \geq \hat{\phi}_{i\pm1}$. In order to be robust and practical, filters should not depend on the field they are applied to.

In the present example, consistency with the 2nd law of thermodynamics can be attained from another point of view. If the total of the variations of the whole field is restricted, i.e. $\sum_{o\,p} |\phi_p - \phi_o| \leq \sum_{o\,p} |\hat{\phi}_p - \hat{\phi}_o|$, the condition for $\hat{\phi}_i$ and $\hat{\phi}_{i\pm1}$ is $2 \leq 2\hat{\phi}_{i\pm1} + 2|\hat{\phi}_i - \hat{\phi}_{i\pm1}|$. This inequality provides 2 possible bounds for f. One is $f < \omega/2(\omega + 1)$ and is dismissed because it violates LED. The other, leads to $f \leq \omega/(2\omega + 1)$. TVD_1, has coincided, in this example, with the restriction obtained imposing $\hat{\phi}_i \geq \hat{\phi}_{i\pm1}$, i.e. it has been equivalent to imposing consistency with the dissipation properties of the analytical models. LED has not. Hence, it becomes apparent that a further condition limiting the growth of maxima and minima is to be imposed, together with LED, on discrete filters in general. TVD_p is discussed next.

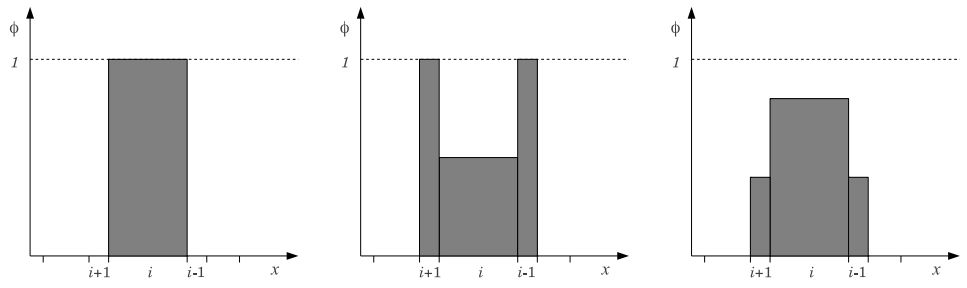

Figure 4.1: Left: Field values before filtering. Center: Filtered field values obtained with a conservative LED filter. Right: Filtered field values obtained with a conservative, TVD_1 and LED filter.

Total Variations Diminishing

TV_p has been introduced above. It allows a quantification of the amount of wiggles/oscillation tat a field contains. Diminishing TV_1 with can be related to the to the differential filter models dissipation properties. In the field of compressible flows simulations, TVD_1 was identified as a sufficient property to construct numerical schemes that do not produce wiggles. First, Harten et al. [33] introduced TVD_1 as an equivalent condition to monotonicity preservation for 1D schemes. The extension

of the concept to multiple dimensions was described, for example, in [34]. This extension was made by locally separating the multidimensional problem into various one-dimensional ones by means of a linearization of the equations and enforcing TVD_1 in each direction. This straightforward strategy does not resolve the extension of TVD_1 into multidimensional unstructured grids. Apart from the compressible flow community, TV_1 bounding was also used in image processing technologies (e.g. [35]). However, in filtering literature for CFD it is not explicitly imposed. In our opinion, it is generally accepted that good local approximations of the TVD_1 continuous filters enforce discrete filters to be TVD_1, but according to the results of Section 4.5 and previous experiences, this assertion is not necessarily true. We consider hereby imposition of the TVD_1 property together with LED on low-pass discrete filters to force consistency with the properties of (4.8) and (4.7).

In the compressible flow literature, the usual TV_p norm is the $\mathcal{L}^1$ norm of the graph gradient of a field $||\mathsf{G}\boldsymbol{\phi}||_1$. Where $\mathsf{G} \in \mathcal{M}_{nf\times n}$ (nf is the number of interfaces between cells) is defined as

$$g_{\underline{op}\,r} = \begin{cases} 1 & \text{if} \quad r = p \\ -1 & \text{if} \quad r = o \\ 0 & \text{if} \quad r \neq o \text{ and } r \neq p. \end{cases} \tag{4.16}$$

The TVD_1 condition on a discrete filter establishes that, for all discrete field $\boldsymbol{\phi}$,

$$||\mathsf{G}\hat{\boldsymbol{\phi}}||_1 = \sum_{\underline{op}} |\hat{\phi}_o - \hat{\phi}_p| \leq \sum_{\underline{op}} |\phi_o - \phi_p| = ||\mathsf{G}\boldsymbol{\phi}||_1. \tag{4.17}$$

Working with absolute values is cumbersome. Hence, we use the square of the $\mathcal{L}^2$ norm to measure oscillations as it can be written in matrix notation. We obtain

$$2(||\mathsf{G}\hat{\boldsymbol{\phi}}||_2)^2 = \sum_o \sum_{p\in N_o} (\hat{\phi}_o - \hat{\phi}_p)^2 \leq \sum_o \sum_{p\in N_o} (\phi_o - \phi_p)^2 = 2(||\mathsf{G}\boldsymbol{\phi}||_2)^2. \tag{4.18}$$

We remark that (4.17) $\not\Rightarrow$ (4.18) and (4.18) $\not\Rightarrow$ (4.17). Now, writing (4.18) in bilinear form,

$$\boldsymbol{\phi}^T\mathsf{F}^T\mathsf{L}\mathsf{F}\boldsymbol{\phi} \leq \boldsymbol{\phi}^T\mathsf{L}\boldsymbol{\phi}. \tag{4.19}$$

Where $\mathsf{L} = \mathsf{G}^T\mathsf{G}$ is the graph Laplacian matrix whose elements are:

$$l_{o\,p} = \begin{cases} -1 & \text{if} \quad o \neq p \quad \Omega_p \in N(\Omega_o) \\ 0 & \text{if} \quad o \neq p \quad \Omega_p \notin N_o \\ \overline{\overline{N_o}} & \text{if} \quad o = p. \end{cases} \tag{4.20}$$

Where $\overline{\overline{\cdot}}$ is the size of a set. In this work, we call L the graph Laplacian matrix or simply the Laplacian matrix. A study of its eigenspace in Section 4.3.8 shows that it

is a good basis for the analysis of the effect of filtering on oscillations.

Condition (4.19) is also equivalent to

$$\mathsf{K} = \mathsf{L} - \mathsf{F}^T \mathsf{L} \mathsf{F} \succeq 0. \tag{4.21}$$

Forcing or checking (4.21) is cumbersome and computationally costly. In 4.B, its elements are calculated for a general case. Also in in 4.B, the simpler situation when $f_{o\,p} = \mathcal{O}(\varepsilon)$ with $\varepsilon \to 0$ is studied by means of the Gershgorin circle theorem. Surprisingly to the authors, we could not demonstrate the positive definiteness of K even in this limit case, so the result of the analysis is not conclusive. Nonetheless, inequality (4.19) can b imposed to the $\boldsymbol{f}_i$ eigenvectors of F. This is equivalent to impose $|\varphi_i| \leq 1$ for all φ_i eigenvalues of F. This can be done applying the Gershgorin circle theorem.

The Gershgorin circle theorem states the eigenvalues of a B matrix lie in $\mathcal{S}_\mathcal{R} \cap \mathcal{S}_\mathcal{C}$ the intersection of the unions of the circles on the complex plane defined as

$$\mathcal{S}_\mathcal{R} = \bigcup_i \mathcal{R}_i \qquad \mathcal{R}_i = \left\{ z \in \mathbb{C} : \, |z - b_{i\,i}| \leq \sum_{j \neq i} |b_{i\,j}| \right\}; \tag{4.22}$$

$$\mathcal{S}_\mathcal{C} = \bigcup_i \mathcal{C}_i \qquad \mathcal{C}_i = \left\{ z \in \mathbb{C} : \, |z - b_{i\,i}| \leq \sum_{j \neq i} |b_{j\,i}| \right\}. \tag{4.23}$$

In this case, $|\varphi_i| \leq 1$ is true if, for all o rows of F

$$f_{o\,o} + \sum_{p \in N_o} f_{o\,p} \leq 1 \tag{4.24}$$

and

$$f_{o\,o} - \sum_{p \in N_o} f_{o\,p} \geq -1. \tag{4.25}$$

For normalized filters, (4.24) is always true and (4.25) is equivalent to (4.15) because $f_{o\,o} = 1 - \sum_{p \in N_o} f_{o\,p}$.

Conditions (4.25) and (4.24) on a filter matrix are necessary but not sufficient to guarantee (4.18) for all $\boldsymbol{\phi} = \sum_i x_i \boldsymbol{f}_i$. In general, inequality (4.19) becomes

$$\sum_{i\,j} x_i x_j \boldsymbol{f}_i^T \mathsf{F}^T \mathsf{L} \mathsf{F} \boldsymbol{f}_j \leq \sum_{i\,j} x_i x_j \boldsymbol{f}_i^T \mathsf{L} \boldsymbol{f}_j, \tag{4.26}$$

which we could not impose for all $\boldsymbol{x}$. However, for filters verifying inequalities (4.24) and (4.25) we can speculate that $\exists D \subset \mathbb{R}^n$ such that for $\boldsymbol{x} \in D$ inequality (4.26) is true. Results in Section 4.5 confirm its existence.

Entropy Consistency

It seems that TVD_p is a good candidate to control variations of filtering operations to prevent the creation of new maxima and minima. However, the difficulty to ensure it restricts its practical use. To overcome this issue, we propose the Entropy Consistency (EC) condition to achieve variations reduction. To explain this condition, we recall that the studied filters are linear and the superposition principle applies. Now, let $\boldsymbol{e^o}$ be a vector of the canonical basis of fields on a mesh with periodic boundary conditions, i.e. $\boldsymbol{e^o}$'s oth coordinate equals 1 and the rest equals 0. Let F be a filter, hence $\hat{\boldsymbol{e}}^{\boldsymbol{o}} = \mathsf{F}\boldsymbol{e^o}$. If F is such that $0 \leq \hat{e}^o_p \leq 1$ for all p, and all $\hat{e}^o_p$ decrease with some geometric distance to Ω_o so $\hat{e}^o_o \geq \hat{e}^o_p$ for all $p \neq o$, we say that F is EC for $\boldsymbol{e^o}$. If F is EC for all o, we say that F is EC. Applying the superposition principle, EC filters respect the 2nd law of thermodynamics and reproduce a heat conduction problem. Consequently, EC filters smear fields. For a filter to be EC for a $\boldsymbol{e^o}$ vector of the canonical basis it is sufficient that the oth row of F verifies inequalities (4.27)

$$f_{o\,o} \geq \sum_{p \in N_o} f_{o\,p} \tag{4.27}$$

and

$$f_{o\,p} \geq 0 \quad \forall p. \tag{4.28}$$

The interest is on filters that control oscillations for all input fields, i.e. EC filters for which (4.27) and (4.28) are true for all o. This is accomplished with positive semidefinite filter matrices with all elements positive. Then, for normalized filters, EC reads

$$1 \geq 2 \sum_{p \in N_o} f_{o\,p} \qquad \forall o, \tag{4.29}$$

and (4.28), which is more restrictive than LED. It is straightforward that EC imposes $f_{o\,o} \geq 0.5$. After these conditions and applying the Gershgorin circle theorem, all φ eigenvalues of an EC filter verify $0 \leq \mathbb{R}(\varphi) \leq 1$. On the example of Figure 4.1, EC gives $0 \leq f \leq min(\omega/2,\, 1/4) \Rightarrow \phi_i \geq \hat{\phi}_i \geq \hat{\phi}_{i\pm1}$.

4.3.8 Low dispersion between the modes of a mesh [4.3.3]

Given a mesh and a spatial discretization, if there was a $\mathcal{B} = \{\boldsymbol{b_1}, \boldsymbol{b_2}, ...\boldsymbol{b_n}\}$ orthonormal basis with respect to the euclidean product of $\mathbb{R}^n$ such that it represented oscillations modes of the mesh on which the fields and operators are defined and $i > j \Rightarrow oscillations(\boldsymbol{b_i}) \geq oscillations(\boldsymbol{b_j})$, the oscillations of a vector $\boldsymbol{\phi} = \sum_i x_i \boldsymbol{b_i}$ would be be related to its coordinates on that base. On Cartesian meshes, it is a common practice to use the $\mathcal{B}$ of the Fourier modes. This can not be done on non-uniform meshes where, to the best of our knowledge, there is not an established

consensus about which $\mathcal{B}$ is the best solution to account for oscillations. The choice of $\mathcal{B}$ is even less standardized on unstructured meshes because the relation between Fourier modes and mesh modes is unclear.

A candidate basis that can represent oscillations whatever the mesh is $\mathcal{B}_l = \{\boldsymbol{l_1}, \boldsymbol{l_2}, \boldsymbol{l_3}, ...\boldsymbol{l_n}\}$: the basis of the normalized eigenvectors of the graph Laplacian matrix L defined in (4.20). Indeed, $\mathsf{L} \succeq 0$ measures oscillations of a field $\boldsymbol{\phi}$ on a spatial discretization and defines a norm on $\mathbb{R}^n$. Taking a pair of eigenvectors $\boldsymbol{l_i}$ and $\boldsymbol{l_j}$ of L corresponding to the eigenvalues λ_i and λ_j, if $|\lambda_i| \geq \lambda_j$, $\boldsymbol{l_i}$ contains more oscillations than $\boldsymbol{l_j}$ and $\boldsymbol{l_i} \cdot \boldsymbol{l_j} = 0$ if $i \neq j$, $\boldsymbol{l_j} \cdot \boldsymbol{l_j} = 1$. Hence, the vectors of $\mathcal{B}_l$ represent of the modes of a mesh. To show this relationship, eigenvectors of L on an structured and an unstructured meshes are depicted, respectively, in Figures 4.3 and 4.4. Eigenvalues of L for the same meshes are shown in Figure 4.2.

Other symmetric positive-definite matrices can be used as a basic norm for measuring oscillations and computing a useful basis to represent mesh modes. Mainly, candidates are expected among discrete differential Laplacian operators or graph Laplacians matrices with volume weightings. Our experience during this work shows that the operator defined in equations (9a-9c) of [36] with centroid as field points also contains information about the mesh distortion and the ϕ fields maxima and minima can be masked by cell volumes changes.

Now, given an endomorphism (a filter matrix) $\mathsf{F} : \mathbb{R}^n \mapsto \mathbb{R}^n$, the effect it produces on the oscillations can be studied by means of the images of each of the vectors of the modes basis. If F was such that $\mathsf{F}\boldsymbol{b_i} = \beta_i \boldsymbol{b_i}$, with $\beta_i \in \mathbb{R}$, we would say that F does not produce dispersion because variations on oscillations modes would be independent. Unfortunately, F generally projects $\boldsymbol{b_i}$ on more vectors of $\mathcal{B}$ than itself. This could be resolved changing the basis on which the analysis is performed, but then the basis might not represent oscillations. Changing the coordinates with the $\Omega^{-1/2}$ matrix, one gets a symmetric filter matrix from a conservative filter. Then, the corresponding change on L would break its symmetry and its capacity to measure oscillation would be lost. Still, one could use $\mathsf{F}' = \Omega^{1/2}\mathsf{F}\Omega^{-1/2}$ the symmetric filter matrix on the new basis as oscillations norm. Then, its eigenvectors would be mesh modes and no dispersion would occur; but these properties would be true on a space where variables have $\Omega^{-1/2}$ dimensions and returning to the physically relevant space would break them. Hence, we stick to an oscillations measuring matrix and its associated basis and we say that filters that project $\boldsymbol{b_i}$ on other vectors of $\mathcal{B}$ than itself are dispersive. Note that if F is symmetric in the physically relevant space, then it can define the oscillations norm and $\mathcal{B}$, so dispersion would not occur.

Regarding the analytical filter models of Section 4.3.2 and taking Fourier series, adaptative filters are dispersive while non adaptative ones are not. Still, we consider that transporting oscillations from low modes to high modes is a negative filtering behavior but, as we could not deduce proper constraints to avoid it and it does not disagree with adaptative filters, no further actions than observations are taken in this sense.

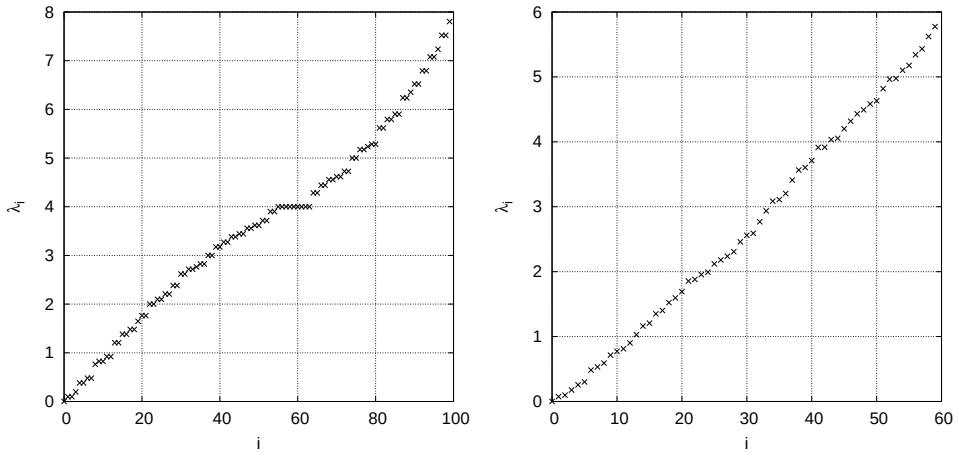

Figure 4.2: Eigenvalues of L on the structured mesh1 (left) and the unstructured mesh2 (right) of Section 4.5.

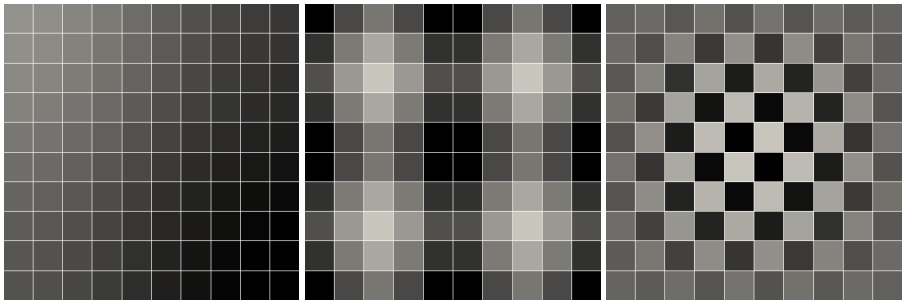

Figure 4.3: Eigenvectors of the Laplacian matrix on the structured "mesh1" of Section 4.5. From left to right: 2, 15, 99.

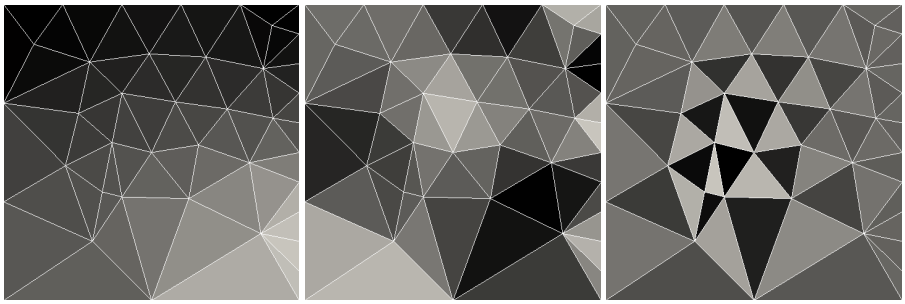

Figure 4.4: Eigenvectors of the Laplacian matrix on the unstructured mesh "mesh2" of Section 4.5. From left to right: 2, 12, 59.

4.4 Limited Filters for CFD

In this section, a set of filters accomplishing some of the conditions introduced in Section 4.3 on cell-centered FV discretizations are presented. Extensions to other discretizations can be envisaged.

4.4.1 Conservative Limited Filter (CLF)

A normalized conservative filter F for $\phi \in \mathbb{R}^n$ has $\sum_o \overline{\overline{N_o}}/2$ independent dimensionless $f_{o\,p}$ elements. As it has been shown in Section 4.3.6, $\check{\mathsf{F}} = \Omega\mathsf{F}$ is symmetric. We write $f_{o\,p} = \check{f}_{o\,p}/\Omega_o = g_{o\,p}\Omega_{\underline{op}}/\Omega_o$ where $\Omega_{\underline{op}}$ is a function of the volumes of cells o and p. For consistency, $\Omega_{\underline{op}}(\Omega_o, \Omega_p) = \Omega_{\underline{po}}(\Omega_p, \Omega_o)$. There is laterality in the definition of $\Omega_{\underline{op}}$. For example, Trias et al. [16] chose $\Omega_{\underline{op}}$ to be the volume of the staggered cells. We use $\Omega_{\underline{op}} = \sqrt{\Omega_o \Omega_p}$ for simplicity and the freedom to use vertex-connected neighbors, which cannot be easily done with staggered cells constructions.

Now, supposing an input set of $g_{o\,p} \geq 0$ for all o and p, LED or EC can be granted by means of two different procedures: The first procedure consists of scaling the $g_{o\,p}$ input values only if

$$Sg_o = \sigma \sum_{p \in N_o} f_{o\,p} = \sigma \frac{1}{\Omega_o} \sum_{p \in N_o} \Omega_{\underline{op}} g_{o\,p} > 1. \tag{4.30}$$

In that case all $\{g_{o\,p} : p \in N_o\}$ are divided by Sg_o. The second procedure consists of

bounding all $g_{o\,p}$ with

$$g_{o\,p} \leq min\left(\frac{\Omega_o}{\sigma\Omega_{\underline{op}}\overline{\overline{N_o}}}, \frac{\Omega_p}{\sigma\Omega_{\underline{op}}\overline{\overline{N_p}}}\right). \tag{4.31}$$

Here, σ is a number that can evaluate 1 or 2. LED is obtained with $\sigma = 1$ while EC is obtained with $\sigma = 2$. Approximation (4.30) is less restrictive than (4.31).

Finally, using the normalization equation, $f_{o\,o} = 1 - \sum_{p\in N_o} f_{o\,p}$.

4.4.2 Differential Limited Filters

Both the Laplacian and the box 2nd order filters from [22] can be expressed, according to equation (4.8) as

$$\hat{\phi} = \phi + \frac{(\epsilon\Delta)^2}{24}\nabla^2\phi + \mathcal{O}(\Delta^4) \tag{4.32}$$

where Δ is the characteristic length of a CV and ϵ the dimensionless parameter controlling the filter width. We apply the model of equation (4.7) instead because it allows adapting Δ and ϵ to each interface. Then, depending on the chosen approximation to the Laplacian operator, conservation and symmetry can be imposed.

We propose a Conservative Differential Limited Filter (CDLF) which is a particularization of CLF:

$$f_{o\,p} = \frac{\epsilon_{\underline{op}}^2(\Omega_o\Omega_p)^{1/3}A_{\underline{op}}}{24\Omega_o(\boldsymbol{r}_{\underline{op}}\cdot\boldsymbol{n}_{\underline{op}})} \quad \text{if } o \neq p \quad ; \quad f_{o\,o} = 1 - \sum_{p\in N_o} f_{o\,p}. \tag{4.33}$$

And a Symmetric Differential Limited Filter (SDLF):

$$f_{o\,p} = \frac{\epsilon_{\underline{op}}^2 A_{\underline{op}}}{24(\Omega_o\Omega_p)^{1/6}(\boldsymbol{r}_{\underline{op}}\cdot\boldsymbol{n}_{\underline{op}})} \quad \text{if } o \neq p \quad ; \quad f_{o\,o} = 1 - \sum_{p\in N_o} f_{o\,p}. \tag{4.34}$$

For both cases, $\boldsymbol{r}_{\underline{op}}$ is the vector that goes from the center of cell o to the center of cell p, $\boldsymbol{n}_{\underline{op}}$ is the unit vector normal to the interface between the cells directed towards p, $A_{\underline{op}}$ is the area between the two cells, and Ω_o is the volume of cell o. The filter width parameter $\epsilon_{\underline{op}}$ is evaluated at interfaces.

To accomplish LED or EC, the elements of the filter matrix should verify $\sigma\sum_{p\in N_o} f_{o\,p} \leq 1$ with $\sigma = 1$ for LED or $\sigma = 2$ for EC. This condition can be attained limiting $\epsilon_{\underline{op}}$

in a similar fashion to what has been done for CLF. Again, there are two different procedures to impose the mentioned limitations: The first, less restrictive than the other, is applied only in the case that $S_o = \sigma \sum_p f_{o\,p} > 1$ at some o cell. If this occurs, using

$$(\epsilon^*_{\underline{op}})^2 = \frac{\epsilon^2_{\underline{op}}}{S_o} \tag{4.35}$$

instead of $\epsilon^2_{\underline{op}}\ \forall p \in N_o$ resolves the problem. The second possibility is to limit all $\epsilon^2_{\underline{op}}$ for all o and for all p so that

$$\epsilon^2_{\underline{op}} \leq \left\{ \frac{1}{\sigma \overline{\overline{N_o}}} \sum_{p \in N_o} \frac{A_{\underline{op}}}{24(\Omega_o \Omega_p)^{1/6}(\boldsymbol{r}_{\underline{\boldsymbol{op}}} \cdot \boldsymbol{n}_{\underline{\boldsymbol{op}}})}, \frac{1}{\sigma \overline{\overline{N_p}}} \sum_{q \in N_p} \frac{A_{\underline{pq}}}{24(\Omega_p \Omega_q)^{1/6}(\boldsymbol{r}_{\underline{\boldsymbol{pq}}} \cdot \boldsymbol{n}_{\underline{\boldsymbol{pq}}})} \right\}. \tag{4.36}$$

Both schemes approximate $\nabla \cdot (\mathsf{A} \nabla(\cdot))$. As stencils with all vertex-neighbors are not straightforward, we propose a methodology to do this in the following paragraphs.

4.4.3 Filters with Vertex-Neighbors Stencils

In FV discretizations, the divergence theorem is the most common tool to obtain discrete operators. Least squares approximations of the values of the fields at interfaces would allow the use of vertex-neighbor stencils, but this results in the loss of control on preservation of operator symmetries. To overcome this problem, we propose the use of ghost surfaces connecting each cell to each of its vertex-neighbors and to apply the divergence theorem straightforwardly.

Let $\mathsf{L_g}$ be the discrete geometric Laplacian matrix of a given mesh. Then, for a cell p sharing a face with cell o, $lg_{o\,p} = A_{\underline{op}}/(\Omega_o ds_{\underline{op}})$, with $ds_{\underline{op}} = \boldsymbol{r}_{\underline{\boldsymbol{op}}} \cdot \boldsymbol{n}_{\underline{\boldsymbol{op}}}$. To extend this formula to a "q" cell , vertex neighbor of o, i.e., sharing one v vertex with it, we propose to use

$$A_{\underline{oq}} = \frac{\Omega_o + \Omega_q}{h_{\underline{vo}} + h_{\underline{vq}}} \tag{4.37}$$

and

$$\boldsymbol{n}_{\underline{\boldsymbol{oq}}} = \begin{cases} \frac{(\boldsymbol{r}_{\underline{\boldsymbol{vo}}} \wedge \boldsymbol{r}_{\underline{\boldsymbol{vq}}}) \wedge (\boldsymbol{r}_{\underline{\boldsymbol{vo}}} + \boldsymbol{r}_{\underline{\boldsymbol{vq}}})}{||(\boldsymbol{r}_{\underline{\boldsymbol{vo}}} \wedge \boldsymbol{r}_{\underline{\boldsymbol{vq}}}) \wedge (\boldsymbol{r}_{\underline{\boldsymbol{vo}}} + \boldsymbol{r}_{\underline{\boldsymbol{vq}}})||} & \text{if} \quad \boldsymbol{r}_{\underline{\boldsymbol{vo}}} \wedge \boldsymbol{r}_{\underline{\boldsymbol{vq}}} \neq \boldsymbol{0} \\ \frac{\boldsymbol{r}_{\underline{\boldsymbol{vo}}}}{||\boldsymbol{r}_{\underline{\boldsymbol{vo}}}||} & \text{if} \quad \boldsymbol{r}_{\underline{\boldsymbol{vo}}} \wedge \boldsymbol{r}_{\underline{\boldsymbol{vq}}} = \boldsymbol{0} \end{cases} \tag{4.38}$$

Where $\boldsymbol{r}_{\underline{\boldsymbol{vq}}}$ is the vector from the v vertex to the centroid of cell q and $h_{\underline{vq}}$ is the volumetric height of the o cell that passes through vertex v, $\boldsymbol{r}_{\underline{\boldsymbol{vo}}}$ and $h_{\underline{vo}}$ are their equivalents for cell o. The value of volumetric heights depends on the polyhedron types of the cells they are referred to. For example, if o is a tetrahedron, $h_{\underline{vo}} = h_v/3$, with h_v

the distance between v and the face of opposed to v. Other polyhedra induce some laterality in the values of $h_{\underline{vo}}$ and $h_{\underline{vo}}$ but satisfactory casuistic solutions can be found.

Equations (4.37) and (4.38) are used to extend the introduced filters to vertex neighbors stencils. LED and EC limitations are imposed in the same way as for their face neighbor stencils equivalents.

4.5 Tests

There is a large variety of tests for filters available in the literature but the properties they are designed to quantify differ appreciably between authors, so comparison of filters developed in different works is not straightforward. For example, the test described in Marsden et al. [6] is designed to study the filter commutation error while tests in Sagaut et al. [22] are designed to compare the discrete filters to their analytic models. Another factor that makes comparisons more difficult is that authors often test 3D filters on full CFD simulations, not isolatedly, so the performance of filters can be accidentally concealed. Following the ideas exposed in the introduction, the tests conducted and reported in this document focus on global properties characterizing filtering. Namely, we propose tests to check the accomplishment of conservation, variations evolution and dispersion properties introduced and developed in Section 4.3. After that, we conduct tests on a singularity and on an isentropic vortex to study the performance of filter on situations more similar to CFD simulations.

In order to analyze dispersion and to clarify conservation and variations evolution we use the basis of the graph Laplacian matrix according to Section 4.3.8. In software terms, we used the `gsl_eigen_symmv` routine of the `gsl` library [37] to calculate the eigenvectors of L.

The tested filters are: a Laplacian approximation to a convolution Gaussian filter, a box based filter and the filters developed in Section 4.4. The Laplacian filter is identified as “Laplacian” and the box as “Box”. Both of them are detailed in 4.A.

For the tests on the introduced properties, all filters are tested with both adaptative and constant filter width parameters (filter drivers) on two different meshes. We specify the following names code to identify the performed tests:

XXXX(V)-Y-Z

Here, ”XXXX“ stands for the filter name; ”V“ expresses that the filter uses vertex-neighbor stencils (face-neighbors stencils are assumed by default), ”Y“ indicates how the filter driver has been computed and ”Z“ identifies the mesh used for the test. The

"Y" parameter can be Constant (C) when the parameter equals 1.5 at all cells, Maxima (M) when it is computed as $|\mathsf{L}\boldsymbol{\phi}|$ or Random (R) when it is has a probability of 0.2 to be different to zero, in which case it is a random number between 0 and 4. The constant filters parameters are common within LES, (M) filter parameters can be used to filter inserted body forces like in [31] and (R) represents situations similar to shock wave detection and conservative fields filtering (see [20]). Two different 2D meshes respectively identified with 1 and 2 have been used: a uniform structured mesh with 100 CV "mesh1" and an unstructured mesh with 60 CV "mesh2", both have been created with the `ANSYS ICEM CFD` software. These meshes are in practice 3D and 1 CV thick. The thickness of mesh1 is 0.1 while the thickness of mesh2 is $60^{-0.5}$. These thicknesses equalize the characteristic lengths of volumes in all dimensions. All boundary conditions are Neumann: the tested fields evaluate the same at the boundary face nodes than in the cell they are in contact with. Hence, boundary face nodes are neither included in L nor in any F. On mesh1, CDLF and SDLF are identical by construction but results of both are represented in all plots to confirm this statement.

For the tests on singularity fields and the isentropic vortex, only the filter names are necessary and the other parameters are specified in the corresponding sections.

The physical interpretation of the filter strength differs between the studied filters and so does the filtering strength parameters. In order to achieve better comparisons, relationships between filter strength parameters have been deduced so that, for "C" and on uniform meshes, all filters with face stencils produce very similar outputs. These same parameters are also used on the vertex stencils filters counterparts. These relations are also applied on situations with nonuniform meshes or adaptative filters. Further details on filter strengths relationships are in 4.C.

Filter strength parameters of the filters proposed in Section 4.4 can be limited using a cell based methodology like in equation (4.31) or an interface based methodology like in equation (4.30). Tests on the filters properties have been conducted with both limiting methodologies but, as results are almost indistinguishable, only those with the cell based methodology are included in this paper. Otherwise, tests on the isentropic vortex and the singularity have been conducted with the cell based methodology only.

4.5.1 Total Variations Evolution Tests

The main objective of a filter is to damp oscillated fields without affecting those with few oscillations. In the basis of the Laplacian matrix, it is damping the $\boldsymbol{l}_i$ with high

λ_i while not damping much the others. We denote $\boldsymbol{\lambda} \uparrow$ the vector of eigenvalues of L in increasing order. In Section 4.3.7 several approximations to damping measurements have been considered. We provide here representations of $||\mathsf{G}\hat{\boldsymbol{l}}_{\boldsymbol{i}}||_1/||\mathsf{G}\boldsymbol{l}_{\boldsymbol{i}}||_1$ vs. i (where each $\boldsymbol{l}_{\boldsymbol{i}}$ corresponds to a λ_i) as a measure of filter damping performance. For the sake of conciseness and because they are very similar, we only show results obtained with the LED condition and we only comment differences with EC at the end of the analysis.

Overall, after the results obtained with the constant filter driver, all filters damp as pretended: filtering effect grows with i. Focusing on results with mesh1 shown in Figure 4.5, it appears that, after scaling filter drivers according to 4.C, all filters except Box give indistinguishable results. Differences between Box and all the other filters come from the filter driver scaling process, where we did not take into account that boundary cells have lower number of neighbors. Besides, on results with mesh2 shown in Figure 4.6, it is observed that all filters damp in a similar fashion. In consonance with their formulations, though, results are not equal. However, differences between Box or Laplacian with respect to the newly developed filters are not much bigger than those between Box and Laplacian. Therefore, we consider that the developed filters damp similarly to the previously existing ones provided that the filter parameters are scaled. Finally, for a given filtering parameter, filters with vertex neighbors introduce more damping. This is because of the larger size of vertex stencils is not taken into account when scaling them.

Figures 4.7 and 4.8 show the results obtained with "M" filter parameters. All filters give similar results, specially on mesh1. Their transfer functions do not damp for the low oscillated modes ($i \to 0$) and become gradually more aggressive for more oscillated ones ($i \to n$). This behavior fits pretty well with the commonly expected transfer function of low-pass filters. However, none of the studied filters reaches the total elimination of the high modes on any of the tested meshes. With regards to the differences between faces stencils and vertices stencils, what has been described for "C" applies.

Results with the random filter driver are shown in Figures 4.9 and 4.10 show that CLF, CDLF and SDLF increase oscillations on both meshes at low i. This negative effect is more evident on mesh 2 and with vertices stencils. As the probability to filter activation is relatively low compared to "C" and to "M" with high i, the damping is lesser. However, all filters tend to reduce oscillation at high i, which is a positive behavior. Among them, CLF, CDLF and SDLF cause the highest damping on most i.

Filters limited with LED are more damping than those limited with EC when the

limitation is active. However, damping behaviors are qualitatively the same. The most relevant quantitative differences have been found on the case with mesh2 and "R" pictured on Figure 4.11 for EC. In this situation, EC approaches better to the reduction of total variations at all modes. Still, at some low modes, total variations increased on the order of 10^{-3} instead of 10^{-2} achieved with LED. Further experiences have been carried with random fields and other settings of the "R" filter driver. The conclusion is that total variations growth has only been observed in situations where the filter driver equals zero at most of the cells while takes values as high as to activate LED or EC at some of them and the base field is a low oscillated mode. This setting is the most effective in the transport of fields from large (test field) to small scales (filter activation field) but it does not correspond to CFD. Some tests without LED nor EC restrictions have been also conducted. Oscillation growth is observed for some $\boldsymbol{b_i}$ with all filters and all meshes when the filter strength parameter is higher than the permitted by LED. We include Figure 4.12 as an example.

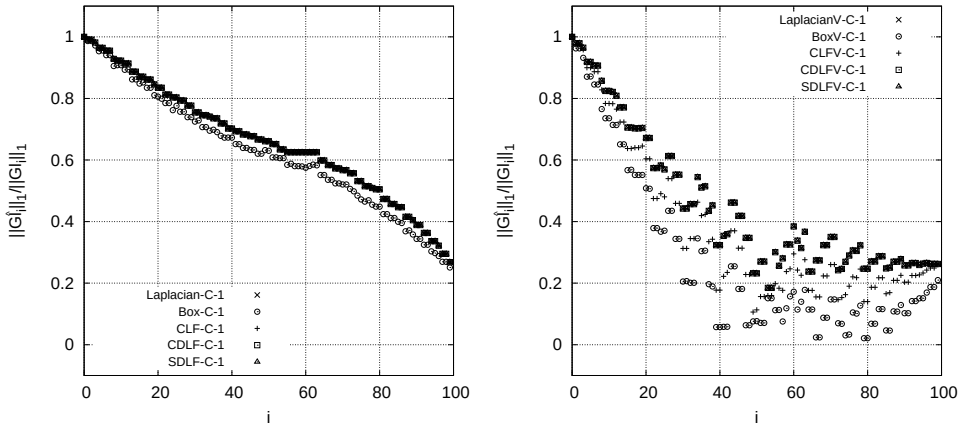

Figure 4.5: $||G\hat{\boldsymbol{I}_i}||_1/||G\boldsymbol{I_i}||_1$vs. i with the "C" filter driver, mesh1 and LED. Left: faces stencils. Right: vertices stencils.

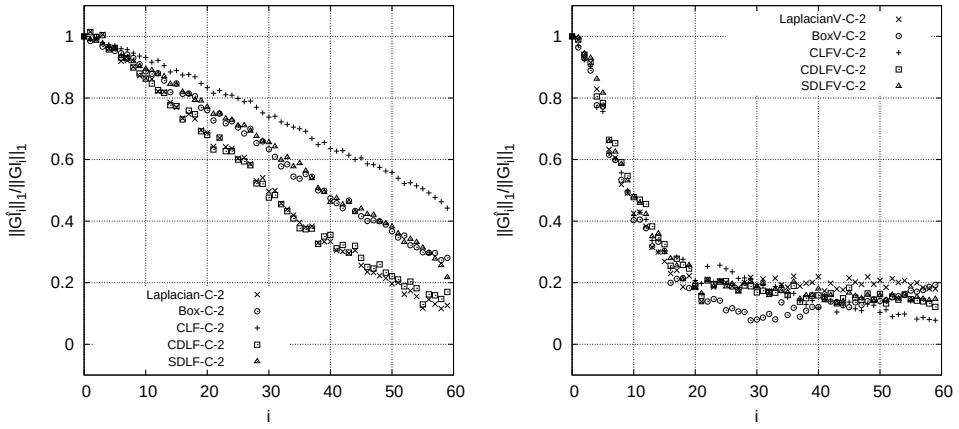

Figure 4.6: $||G\hat{I}_i||_1/||GI_i||_1$ vs. i with the "C" filter driver, mesh2 and LED. Left: faces stencils. Right: vertices stencils.

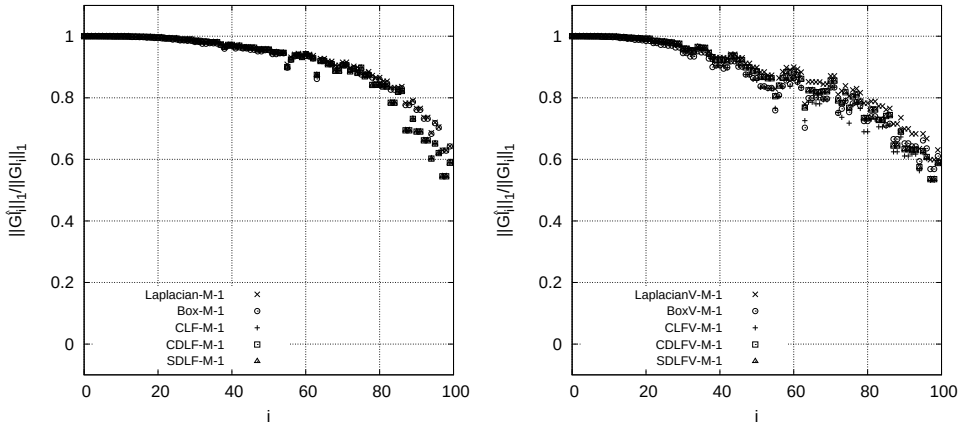

Figure 4.7: $||G\hat{I}_i||_1/||GI_i||_1$ vs. i with the "M" filter driver, mesh1 and LED. Left: faces stencils. Right: vertices stencils.

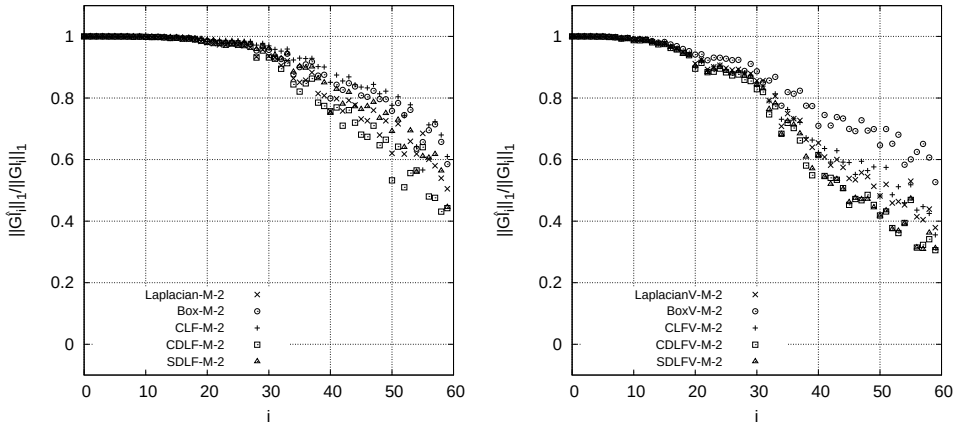

Figure 4.8: $||G\hat{I}_i||_1/||GI_i||_1$ vs. i with the "M" filter driver, mesh2 and LED. Left: faces stencils. Right: vertices stencils.

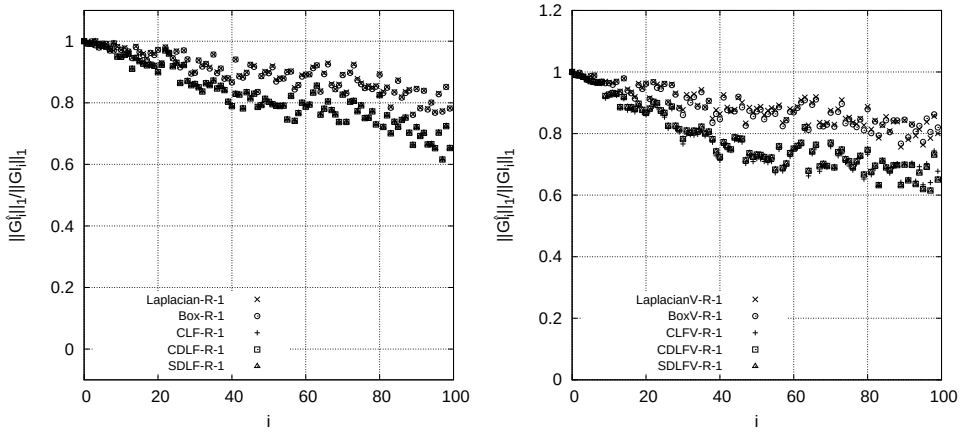

Figure 4.9: $||G\hat{I}_i||_1/||GI_i||_1$ vs. i with the "R" filter driver, mesh1 and LED. Left: faces stencils. Right: vertices stencils.

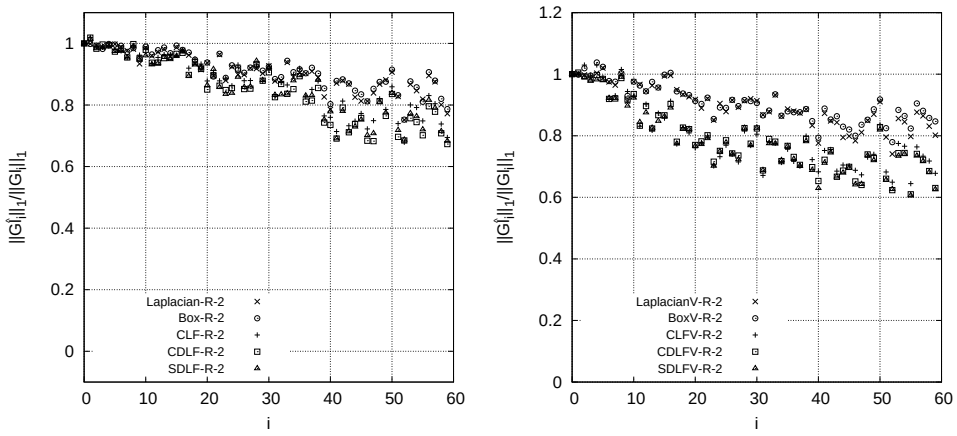

Figure 4.10: $||G\hat{I}_i||_1/||GI_i||_1$ vs. i with the "R" filter driver, mesh2 and LED. Left: faces stencils. Right: vertices stencils.

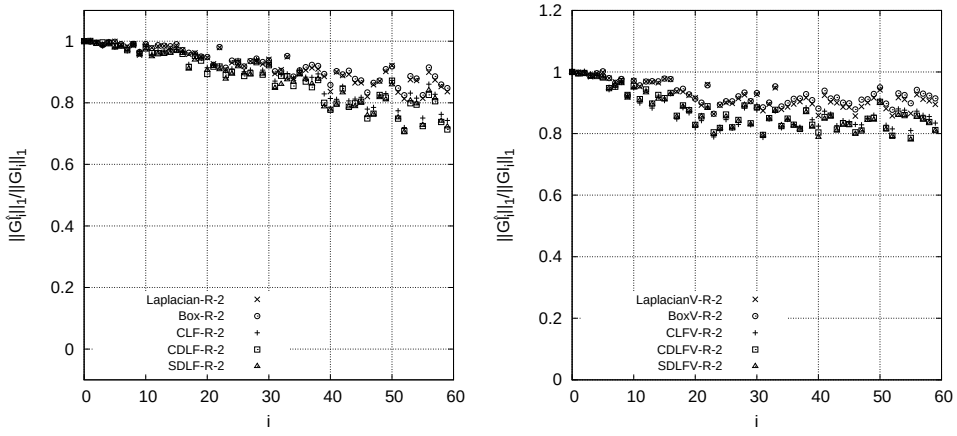

Figure 4.11: $||G\hat{I}_i||_1/||GI_i||_1$ vs. i with the "R" filter driver, mesh2 and EC. Left: faces stencils. Right: vertices stencils.

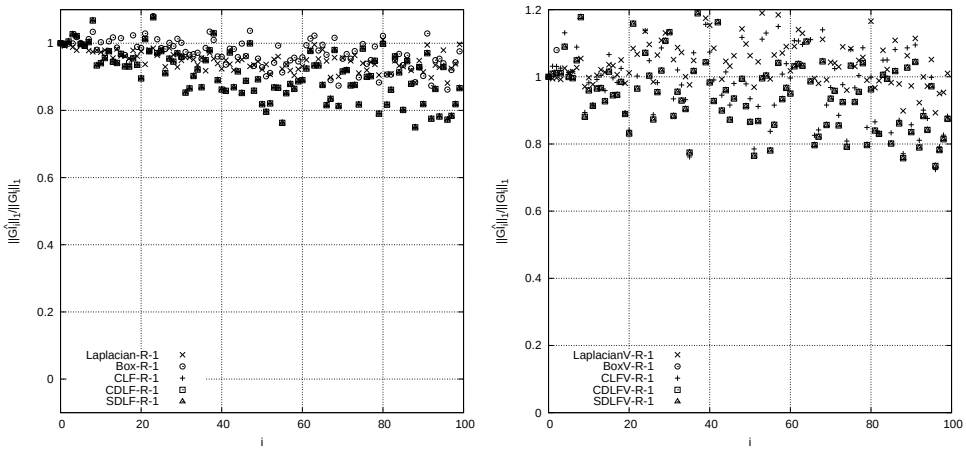

Figure 4.12: $||G\hat{\boldsymbol{l}}_i||_1/||G\boldsymbol{l}_i||_1$ vs. i with the "R" filter driver, mesh1 and no filter strength limit. Left: faces stencils. Right: vertices stencils.

4.5.2 Conservation Tests

For a conservative filter, the magnitude $\mathbf{1}^T\Omega(\boldsymbol{l}_i - \hat{\boldsymbol{l}}_i)$ equals zero. Here, its resulting value calculated with the considered filters configurations is analyzed to study possible relations on the oscillations present in the test field. Results with the "C" filter driver are plotted on Figures 4.13 and 4.14. On mesh1, only Box is not conservative while on mesh2, only CLF and CDLF conserve the integral of $\boldsymbol{\phi}$ in the domain. It is also observed that vertex-stencils filters are less conservative, probably because they have a greater effect when the filter strength parameter is the same. Results of tests with the "M" filter driver are plotted in Figures 4.15 and 4.16. On mesh1, CLF, CDLF and SDLF are conservative for all $\boldsymbol{l}_i$ while Laplacian and Box are remarkably non conservative. On mesh2, SDLF is not conservative anymore but it is closer to it than Laplacian or Box. Again, vertex stencils reduce conservation of non-conservative filters. In all cases, a dependence of $\mathbf{1}^T\Omega(\boldsymbol{l}_i - \hat{\boldsymbol{l}}_i)$ with respect to i is observed with "M". This can be attributed to the growth of the filter width with i for mesh2, while for mesh1 $\mathbf{1}^T\Omega(\boldsymbol{l}_i - \hat{\boldsymbol{l}}_i)$ is higher for i around 60. Results of tests with "R" are not reproduced. They differ from those with "M" because there is not a dependence on i.

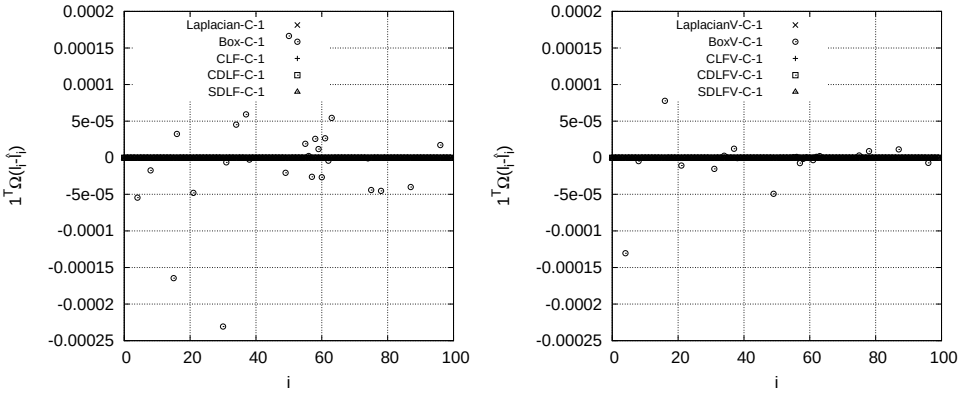

Figure 4.13: $\mathbf{1}^T\Omega(\boldsymbol{l_i} - \hat{\boldsymbol{l}}_{\boldsymbol{i}})$ vs. i with the "C" filter driver, mesh1 and LED. Left: faces stencils. Right: vertices stencils.

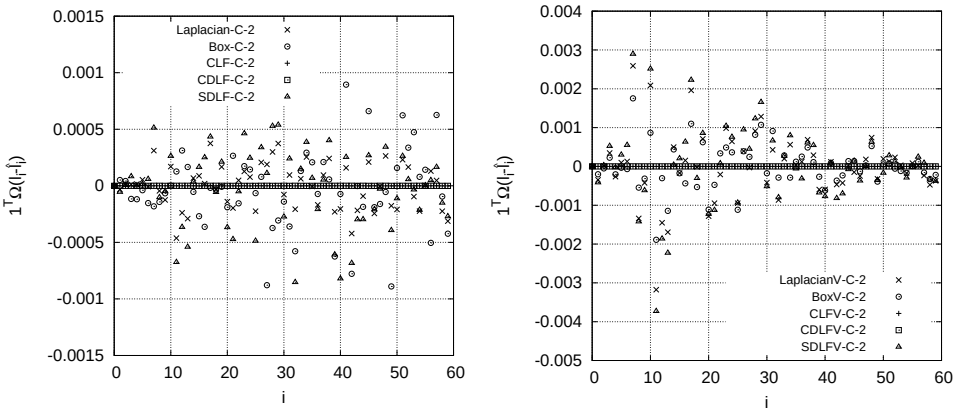

Figure 4.14: $\mathbf{1}^T\Omega(\boldsymbol{l_i} - \hat{\boldsymbol{l}}_{\boldsymbol{i}})$ vs. i with the "C" filter driver, mesh2 and LED. Left: faces stencils. Right: vertices stencils.

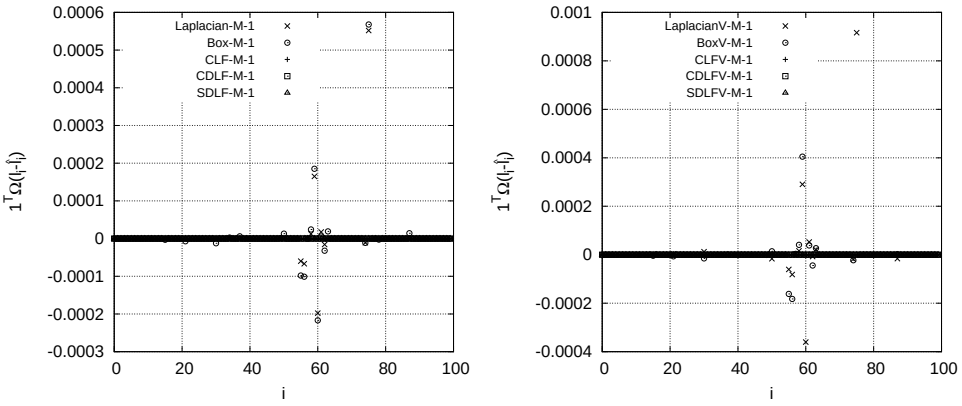

Figure 4.15: $\mathbf{1}^T\Omega(\boldsymbol{l_i} - \hat{\boldsymbol{l}}_{\boldsymbol{i}})$ vs. i with the "M" filter driver, mesh1 and LED. Left: faces stencils. Right: vertices stencils.

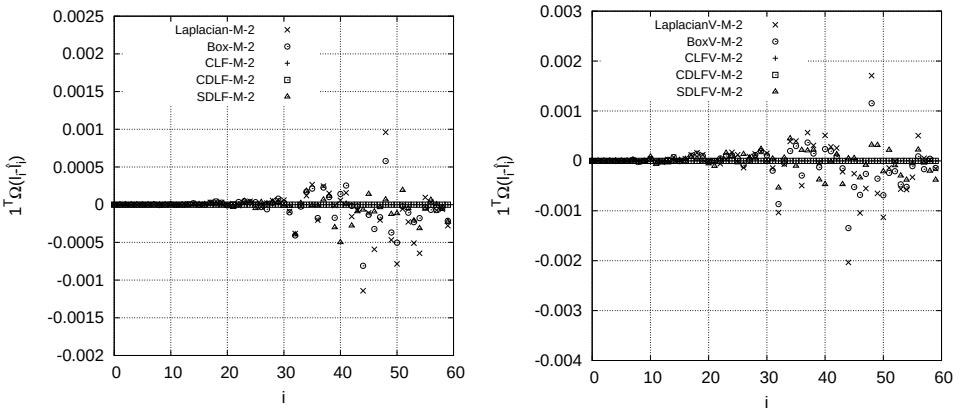

Figure 4.16: $\mathbf{1}^T\Omega(\boldsymbol{l_i} - \hat{\boldsymbol{l}}_{\boldsymbol{i}})$ vs. i with the "M" filter driver, mesh2 and LED. Left: faces stencils. Right: vertices stencils.

4.5.3 Dispersion Tests

An analysis focused on the study of the dispersion that a filter produces on each $\boldsymbol{l_i}$ has also been conducted. 2D grayscale plots of the moduli of coordinates of $\hat{\boldsymbol{l}}_{\boldsymbol{i}}$ in the basis $\mathcal{B}_l$ represent the dispersion produced by each filter. For a position $i\,j$ of the graphs in Figures 4.17-4.20, the ordinate i represents the filtered mode $\boldsymbol{l_i}$, the abscissa value j represents the index of the coordinate j in $\mathcal{B}_l$ basis, and the gray intensity represents the absolute value of $(\hat{l}_i)_j$ in logarithmic scale. Accordingly, non-dispersing filters produce dark gray in the diagonal and white elsewhere. However, filters transporting energy from higher to lower modes are also considered satisfactory. In the present test, such behavior would cause a dark gray diagonal, a lighter dark gray on the lower right corner and a lighter gray at the other positions. Other criteria like dispersing to close modes (gray only near the diagonal, white at the rest) can also be useful for CFD purposes. Most of the figures that included here contain data obtained with EC restricted filters only. Differences between EC and LED are described at the end of the section.

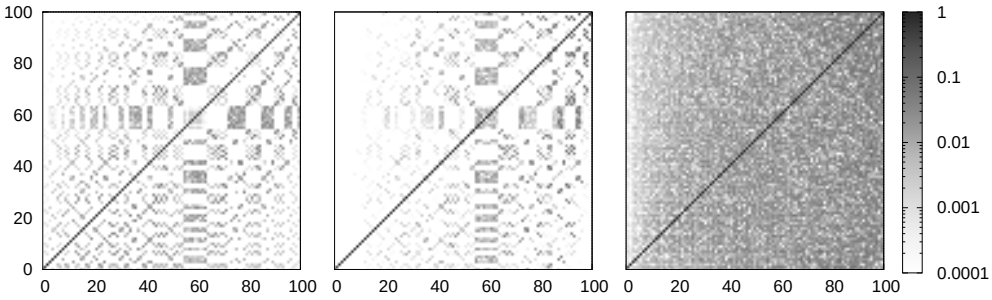

Figure 4.17: Dispersion tests on mesh1 with faces stencils and EC. Top: CDLF, bottom: Box. Columns, from left to right: C, M, R.

Results show that the mesh, the filter driver and the stencil have a noticeable influence on the dispersion properties of the filters. Regarding the difference between meshes for a given set of filter, driver and stencil, we notice that, for all situations excepting "R" drivers, filters produce remarkably more dispersion on mesh2 than on mesh1. On mesh1 and given an stencil, Gauss, CLF, CDLF and SDLF are equal. With this mesh, (Figures 4.17 and 4.18) and after the results obtained with the "C" and "M" filter drivers, $(\hat{l}_i)_j$ take values different to zero for most i and some j around 60 and for some i around 60 and j. So, the graphs are mostly white and exhibit ordered gray patterns symmetric respect to the diagonal. The eigenvectors $\hat{\boldsymbol{l}}_{\boldsymbol{i}}$ for which more dispersion is observed are the same than those towards which the test fields

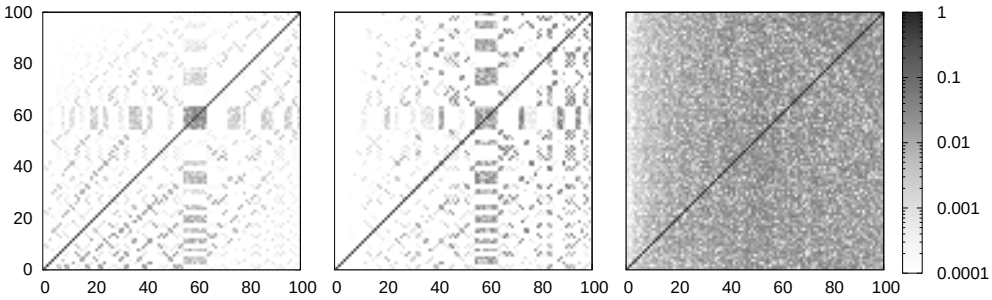

Figure 4.18: Dispersion tests on mesh1 with vertices stencils and EC. Top: CDLF, bottom: Box. Columns, from left to right: C, M, R.

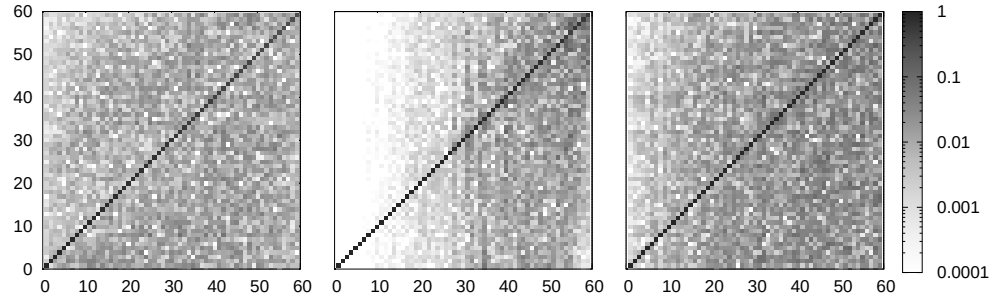

Figure 4.19: Dispersion tests on mesh2 with faces stencils and EC. Top: CDLF, bottom: Box. Columns, from left to right: C, M, R.

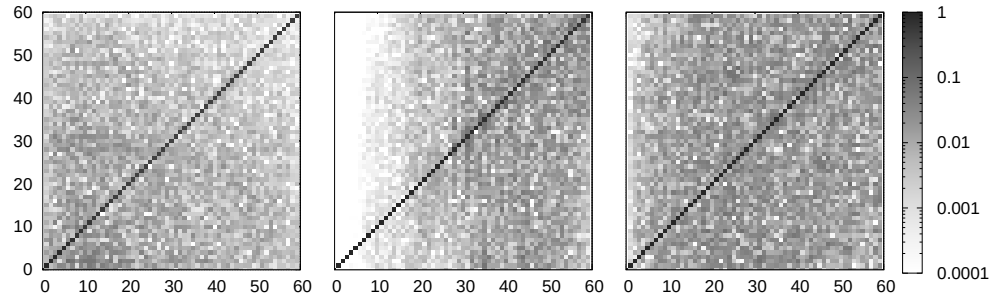

Figure 4.20: Dispersion tests on mesh2 with vertices stencils and EC. Top: CDLF, bottom: Box. Columns, from left to right: C, M, R.

are mostly projected. They are also the lesser conservative ones with "M" and mesh1 in the conservation test. Figures 4.19 and 4.20 show results on mesh2. Only CDLF and Box are represented because differences with other filters are irrelevant in this test. No ordered patterns are distinguishable and the effect of the stencil is almost irrelevant regardless of the mesh.

Finally, in Figure 4.21, a dispersion comparison between EC and LED is shown. Dispersion is qualitatively equal but EC keeps, for all j, $(\hat{l}_i)_j/(\hat{l}_i)_i$ relatively lower than LED, so dispersion is lower. Such behavior has been observed with all meshes and filter drivers. It is attributed to the lower filter strength limit of EC.

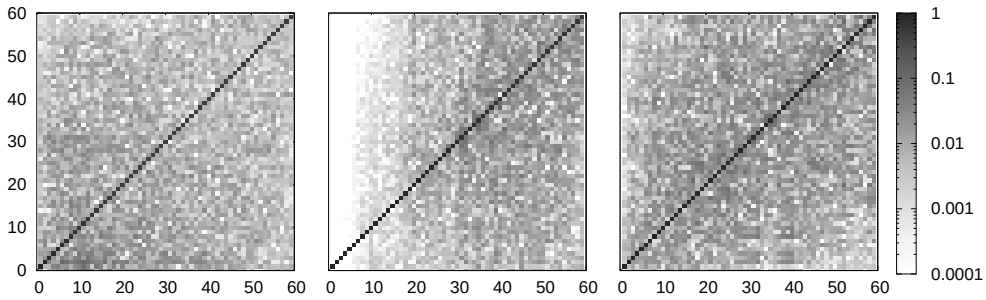

Figure 4.21: Projection tests on mesh2 with CLF with vertices stencils. Top: LED condition, bottom: EC condition. Columns, from left to right: C, M, R.

4.5.4 Tests on a singularity

Filtering of a singularity field has been carried out in order to compare EC to LED variations reduction constraints. This test consists on filtering a field evaluating 0 in all CV but one near the center of the mesh where it evaluates 1. Tests are performed on mesh1 and mesh2 with constant filter strength parameters. The value of the filter parameter is 2 for the reference Laplacian filter while for the other filters it has been adapted as detailed in 4.C. The variations reduction limit on the filter strength parameter has been imposed with Inequality (4.31) on CLF, with Inequality (4.36) on CDLF and SDLF and as it is described in 4.A for Box and Laplacian. Figures 4.22 and 4.23 show the filtered fields. With the LED constraint, the neighbors of the singularity become maxima after filtering while, as it has been predicted in Section 4.3.7, EC avoids it. After the results, EC filters seem more appropriate for cases with singularities or elements with very sharp gradients like the body forces of the Actuator Line Method (see, e.g. [31]) and the Immersed Boundary Methods (see, e.g. [19]). It also

seems that vertex stencils are better fitted for these cases as they spread singularities on areas with rounder shapes, better approaching analytic filtering in continuous spaces.

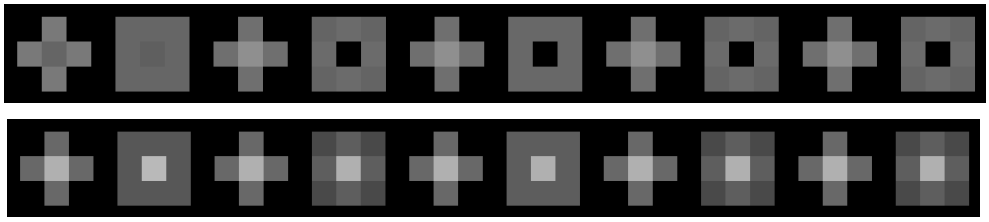

Figure 4.22: Filtered singularity on mesh1, brighter gray shades are higher values. LED (top) vs. EC (bottom) restrictions. From left to right: Box, BoxV, Laplacian, LaplacianV, CLF, CLFV, CDLF, CDLFV, SDLF, SDLFV.

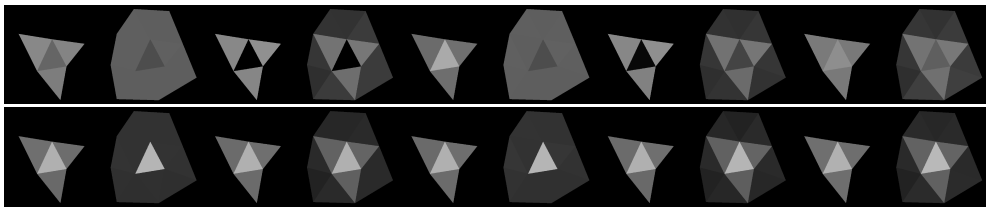

Figure 4.23: Filtered singularity on mesh2, brighter gray shades are higher values. LED (top) vs. EC (bottom) restrictions. From left to right: Box, BoxV, Laplacian, LaplacianV, CLF, CLFV, CDLF, CDLFV, SDLF, SDLFV.

4.5.5 Tests on a 2D isentropic vortex

Vortices are the simplest flow structure in cases without sources or sinks and one of the basic flow elements of inviscid potential flow approximations. We filter a 2D isentropic vortex to study the effect of the introduced filters on a typical configuration with physical relevance. The vortex velocity field is:

$$\mathbf{u} = u_a \exp\left(\frac{1-r^2}{2}\right)\left\{\begin{array}{c}\eta\\-\xi\end{array}\right\}. \tag{4.39}$$

with $\xi = (x - x_0)/b$, $\eta = (y - y_0)/b$ and $r^2 = \xi^2 + \eta^2$, b is a parameter determinative of the vortex size and u_a determines the vortex intensity. We use $u_a = 1$ and

$b = 0.2/\sqrt{\log(2)}$ on the unitary square sided 2D meshes, where the vortex is centered.

The analytic filtered vortex field is, according to Equation (4.8):

$$\hat{\mathbf{u}}^* = u_a \exp\left(\frac{1-r^2}{2}\right) \left\{ \begin{array}{c} \eta + \frac{\varepsilon^2}{24b^2}(-1 - 2\eta + \xi^2\eta + \eta^2) \\ -\xi + \frac{\varepsilon^2}{24b^2}(-1 + 2\xi - \xi\eta^2 + \xi^2) \end{array} \right\}. \tag{4.40}$$

We perform two different tests: the first aims to provide data for comparison of filters and the second aims to evaluate the accuracy of the filters on similar meshes with appreciably different numbers of cells, i.e. cell sizes. For both of them, we use the EC variations reduction condition for all computations and the constant input filter parameter $\epsilon = \sqrt{2}$.

In the first test, various relevant magnitudes are calculated from the filtered fields obtained with the filters introduced in former sections. These magnitudes are circulation, error with respect the analytical solution, total variations with respect to the unfiltered field and average, maximum and minimum horizontal velocity. Circulation is computed as

$$\Gamma = \frac{\sum_o \Omega_o (uy - vx)_o}{\sum \Omega_o}, \tag{4.41}$$

TV as

$$TV = \frac{1}{2}\left(\frac{\sum_{\underline{op}} |\hat{u}_o - \hat{u}_p|}{\sum_{\underline{op}} |u_o - u_p|} + \frac{\sum_{\underline{op}} |\hat{v}_o - \hat{v}_p|}{\sum_{\underline{op}} |v_o - v_p|}\right), \tag{4.42}$$

and the error as

$$Err = \frac{1 + V_{in}/V_{bound}}{V_{in} + V_{bound}} \frac{\sum_{o \in in} ||\hat{\mathbf{u}}_o - \hat{\mathbf{u}^*}_o|| \Omega_o^{1/3}}{\sum \Omega_o}, \tag{4.43}$$

upon which some considerations follow.

Since the effective filtering effect is proportional to $(\epsilon\Delta)^2$ and so is $||\hat{\mathbf{u}^*}_o - \hat{\mathbf{u}}_o|| = ||(\hat{\mathbf{u}^*}_o - \mathbf{u}_o) - (\hat{\mathbf{u}}_o - \mathbf{u}_o)||$, we scale the volume averaged error dividing it by the square of local characteristic lengths, i.e., $\Omega_o^{2/3}$. Doing thus, the filtering strength dependence on the mesh is prevented from blurring the results. Furthermore, as at cells next to boundaries the filters are far from reproducing Laplacians, the total error would be dominated by the error on these cells if they were taken into account. Hence, only cells with no boundary faces are included in the sum of Equation (4.43). After this, the error gets blurred again by the difference of volumes of the meshes without boundary cells. We define V_{in} as the sum of the volumes of all cells without

boundary faces and V_{bound} as the sum of the volumes of all cells with boundary faces to add an scaling factor that resolves the problem. After all these considerations, the error is only due to differences between filters spatial discretizations and analytic Laplacians. It is expected to increase with coarser meshes as the discrete representation of the vortex becomes less accurate.

Results of the first test on mesh1 are shown on Table 4.1. Laplacian, CLF, CDLF and SDLF are the same filter on this mesh. Filters with vertex stencils cause a more noticeable reduction of extrema of the horizontal velocity than those with face stencils. This was already observed and explained in tests on variations evolutions. It is also relevant that the error committed with respect to the analytic filter with vertex stencils is orders of magnitudes higher than the error committed with face stencils. This shows that the method developed in Section 4.4.3 to extend filters to vertex stencils does not accurately approximate the Laplacian operator. However, as stated before, we do not consider this a determinative criterion when designing filters. Comparing filters with face stencils, all excepting Box give the same results because the filter parameters were adjusted to do this. The discrepancies of the Box filter on all magnitudes but *Err* is because the different number of neighbors of boundary cells is not taken into account when calculating filter strength parameters. This was already observed in previous tests. We also remark that the Box filter does not reduce Γ and BoxV increases it. Finally, it is noticeable that non-conservative filters can change the average of the horizontal velocity on its order of magnitude.

Results with mesh2 are on Table 4.2. Vertices stencils produce larger errors than faces stencils but they are on the same order of magnitude. Actually, on this 2D test, they keep a ratio next to $10/3$. This can be related to the ratio of the numbers of neighbor cells that each stencil involves. The conservation behavior is the expected. Again, non conservative filters change $\overline{U}$ on its order of magnitude. Circulation is not reduced by LaplacianV and it is significantly increased by Box, showing the difficulty of filtering on unstructured meshes.

There are no remarkable accuracy differences between the developed filters and the previously existing ones.

The objective of the second test is to compare the accuracy of the different filters on uniform and unstructured meshes with significantly different numbers of cells. To do it, two structured Cartesian meshes with 25 and 225 CV respectively and two unstructured meshes with 25 and 177 CV are additionally employed. Volumes thickness is set with the same criterion as it has been done with mesh1 and mesh2 so the characteristic length of mesh cell equals ${N_{cells}}^{-0.5}$. The Error calculated with Equa-

Filter	Γ	Err	TV	$\overline{U}$	U_{max}	U_{min}
noFilter	0.215	2.67	1	-1.24e-10	0.977	-0.977
Analytic	0.211	0	0.955	-3.84e-11	0.936	-0.936
Laplacian	0.214	0.114	0.948	7.23e-11	0.938	-0.938
LaplacianV	0.213	2.67	0.89	5.79e-10	0.897	-0.897
Box	**0.215**	1.19	0.914	-3.44e-10	0.919	-0.919
BoxV	**0.217**	2.97	0.867	-1.18e-10	0.892	-0.892
CLF	0.214	0.114	0.948	-1.24e-10	0.938	-0.938
CLFV	0.212	2.97	0.887	-1.24e-10	0.892	-0.892
CDLF	0.214	0.114	0.948	-1.24e-10	0.938	-0.938
CDLFV	0.213	2.67	0.893	-1.24e-10	0.897	-0.897
SDLF	0.214	0.114	0.948	1.71e-10	0.938	-0.938
SDLFV	0.213	2.67	0.893	4.95e-10	0.897	-0.897

Table 4.1: Results of some relevant parameters after filtering vortex on mesh1.

tion (4.43) is plotted as a function of the number of cells of the meshes on Figure 4.24. With structured meshes, the error tends to zero as the number of cells increases when using faces stencils while it does not vary with a recognizable trend with vertex stencils. A clear trend is not observed for any stencil or filter on the unstructured meshes plot. The only clear conclusion from the vertex stencils plot is that vertex stencils produce larger errors than face stencils. Finally, we highlight that the dependence on meshes of the results obtained with filters developed in section 4.4 is not significantly different to that of the the corresponding Box or Laplacian filters.

Filter	Γ	Err	TV	$\overline{U}$	U_{max}	U_{min}
noFilter	0.219	2.61	1	-0.00644	0.999	-0.986
Analytic	0.211	0	0.926	-0.00191	0.936	-0.87
Laplacian	0.218	0.913	0.901	-0.00651	0.932	-0.891
LaplacianV	**0.219**	3.44	0.801	-0.00405	0.855	-0.777
Box	**0.223**	2.06	0.898	-0.015	0.921	-0.864
BoxV	0.216	5.42	0.789	-0.0141	0.835	-0.731
CLF	0.218	1.36	0.943	-0.00644	0.959	-0.933
CLFV	0.211	4.46	0.808	-0.00644	0.836	-0.784
CDLF	0.218	1.12	0.904	-0.00644	0.929	-0.899
CDLFV	0.214	3.78	0.838	-0.00644	0.837	-0.856
SDLF	0.218	0.897	0.905	-0.00582	0.936	-0.886
SDLFV	0.211	3.98	0.826	0.0092	0.837	-0.794

Table 4.2: Results of some relevant parameters after filtering vortex on mesh2.

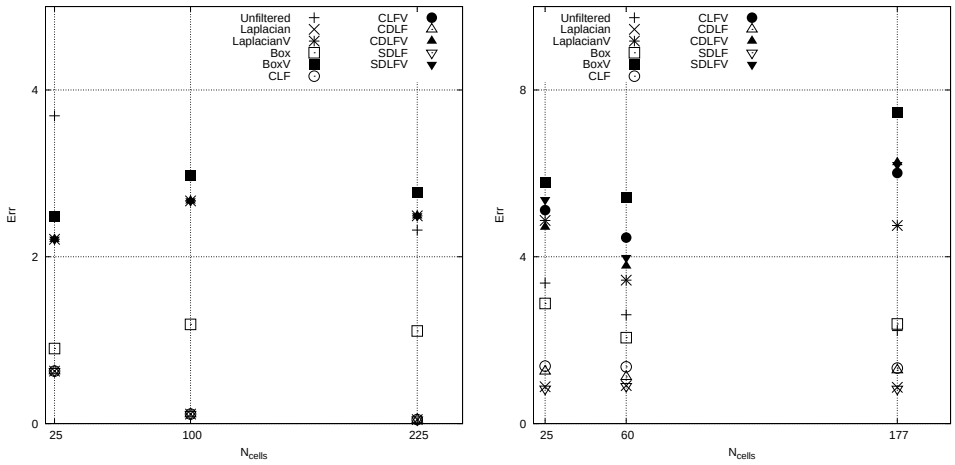

Figure 4.24: Error with respect to analytical filtering computed with equation (4.43) as a function of the number of cells. Left: Cartesian meshes. Right: Unstructured meshes. The average characteristic cell length is $N_{cells}{}^{-0.5}$

4.6 Conclusions and future work

The properties of the analytical convolution filter have been revised together with other analytical filter models used in CFD have been revised. The properties of the

convolution filter that we have considered more characteristic of filtering have been adapted to discrete operators. Then, constraints enforcing them have been derived. Vreman [23] related normalization and conservation to the conservation of momentum and dissipation of kinetic energy in the context of LES. We have derived and successfully imposed these properties without need of relating filters to specific applications. It has been shown, by means of an example, that LED (positivity in [8]) is not sufficient to reproduce the diffusivity of the analytic models. Total Variation Diminishing of order 1 has been suggested as an objective diffusivity enforcing restriction but we could not theoretically impose it. We could not impose it TVD_2 for all input fields either. Diffusivity, however, has been approached with two different conditions: LED and EC. LED has been found to lead to the same condition as preventing the growth of the square of the Euclidean norm of the gradient for eigenvectors of the filter operator. EC mimics the second law of thermodynamics in heat transfer problems and is more restrictive than LED.

Three filters have been designed to satisfy one of the variations restrictions, normalization and conservation or symmetry. These filters have been implemented with faces-neighbors and vertex-neighbors stencils.Then, they have been tested alongside with a Laplacian and a Box filters.

Tests on the basic properties have been conducted using the eigenvectors of the graph Laplacian matrix of meshes as the tested fields because they are a good basis to represent oscillations scales. Results show TV_1 on most cases even when EC or LED (instead of TVD_1) is imposed. Still, low oscillated fields and filters active only on some cells result on relative TV_1 growths of 10^{-3} in the case of EC and 10^{-2} in the case of LED. Since the pathological settings (smooth fields and sharp variations of filtering intensity) are not usual in CFD, we consider the proposed variations restrictions surprisingly satisfactory. Tests also show that filters for which conservation is not imposed are not conservative. Dispersion tests show that LED and EC are also useful to bound the amount of dispersion that filtering produces between the modes of meshes and that lesser dispersion is obtained with EC because it is more constraining. In summary, tests results confirm that the developed filters are good candidates to be used in most of the CFD applications and that LED and EC conditions can restrain TV_1 growth in almost all relevant CFD cases.

The proposed and the previously existing filters have been also tested on singularity fields providing results that show the advantage of EC over LED in cases with very steep gradients. While LED allows dislocation of extrema, EC does not. Thereby, it is in better consonance with the properties of the introduced analytic filters.

Further tests on an isentropic vortex show that the introduced filters, compared to existing ones, do not increase local errors. However, it has been seen that the local inaccuracy with respect to the analytical explicit differential second order models in Sagaut and Grohens [22] of the studied filters increases with unstructured meshes and vertex stencils. We do not believe this is a major inconvenience as we consider that operators should be first approximated in their characterizing global properties and later provided with local accuracy. For example, the introduced CDLF with vertex stencils leads to high local errors with respect to the analytic model it's based on but it is conservative and normalized. These are properties of the analytic model that Least Squares approximations to Laplacians do not respect.

Tests on the isentropic vortex have also shown that the Box, BoxV and Laplacian filters can increase vortex circulation even when the EC constraint is imposed. This could cause a malfunction to LES models that use them, so our opinion is that further research on filters effect to this kind of simple relevant configurations should be performed.

The proposed restrictions are expected to be a good starting point for filter design. Then, specific applications require further conditions that should be compatible with those developed here. For example, commutation with differentiation is characteristic of convolution but not of all other analytical filter models and this is why we did not consider it a filter characterizing property. Meanwhile conservation is equivalent to normalization in convolution and characterizing of most of the analytical models presented in this work, so we recommend to impose is not always imposed on discrete filters in the literature. To us, after the results on the isentropic vortex where it is shown that non-conservative filters can increase circulation, an effort should be made to clarify if relaxing conservation allows for physically consistent filters. Low dispersion and TVD_1 remain objective properties as we could not explicitly impose them. However, smoothing of any input field, which is the most basic consequence of filtering, has been practically attained for compact supported explicit filters with the EC condition.

We emphasize the capabilities of the proposed testing techniques introduced in this document to better separate and identify the performance of filters on each field mode for all types of meshes. We consider that research on filters should try to find better tests to isolate, as much as possible, filter behavior from any other operation. In this sense, substituting the eigenvectors of the graph Laplacian matrix by those of some volume-weighted symmetric semidefinite matrices with physical relevance could improve the oscillations measurements performed here. This would take into

account spatial variables while avoiding the inconveniences of the differential operators on unstructured meshes.

Most of the paper is focused on FV and finite discrete space, but all the theories and properties studied can be easily extended to general Hilbert spaces or other discretizations.

Future work will focus on the use of the proposed filters in actual CFD simulations.

Acknowledgments

Fred Wubs and Maurits Silvis from the University of Groningen are kindly acknowledged for their advices. This work has been financially supported by the Spanish Ministerio de Economía y Competitividad through the grant BES-2010-032414, the research program ENE-2012-36910 and the Ramón y Cajal postdoctoral contract RYC-2012-11996.

References

[1] A. Báez Vidal, O. Lehmkuhl, F. X. Trias, and C. D. Pérez-Segarra. On the properties of discrete spatial filters for CFD. *Journal of Computational Physics*, 326:474–498, 2016.

[2] R.S. Rogallo and P. Moin. Numerical simulation of turbulent flows. *Annual Review of Fluid Mechanics*, 16:99–137, 1984.

[3] T. S. Lund. The Use of Explicit Filters in Large Eddy Simulation. *Computers and Mathematics with Applications*, 46:603–616, 2003.

[4] S. Ghosal and P. Moin. The Basic Equations for the Large Eddy Simulation of Turbulent Flows in Complex Geometry. *Journal of Computational Physics*, 118(1):24–37, 1995.

[5] O.V. Vasilyev, T.S. Lund, and P. Moin. A general class of commutative filters for LES in complex geometries. *Journal of Computational Physics*, 146:82–104, 1998.

[6] A. L. Marsden, O. V. Vasilyev, and P. Moin. Construction of Commutative Filters for LES on Unstructured Meshes. *Journal of Computational Physics*, 175:584–603, 2002.

[7] A. Haselbacher and O. V. Vasilyev. Commutative discrete filtering on unstructured grids based on least-squares techniques. *Journal of Computational Physics*, 187(1):197–211, 2003.

[8] B. Vreman, B. Geurts, and H. Kuerten. Realizability conditions for the turbulent stress tensor in large-eddy simulation. *Journal of Fluid Mechanics*, 278:351, 1994.

[9] M. Germano. Turbulence - The filtering approach. *Journal of Fluid Mechanics*, 238, 1992.

[10] M. Germano, U. P., P. Moin, and W. H. Cabot. A dynamic subgrid-scale eddy viscosity model. *Physics of Fluids A: Fluid Dynamics*, 3(7):1760–1765, 1991.

[11] Noma Park, Sungwon Lee, Jungil Lee, and Haecheon Choi. A dynamic subgrid-scale eddy viscosity model with a global model coefficient. *Physics of Fluids*, 18(12):125109, 2006.

[12] Donghyun You and P. Moin. A dynamic global-coefficient subgrid-scale eddy-viscosity model for large-eddy simulation in complex geometries. *Physics of Fluids*, 19(6):1–8, 2007.

[13] T.J.R. Hughes, L. Mazzei, and K.E. Jansen. Large Eddy Simulation and the variational multiscale method. *Computing and Visualization in Science*, 3:47–59, 2000.

[14] A.W. Vreman, B. Geurts, and H. Kuerten. Large-eddy simulation of the turbulent mixing layer. *Journal of Fluid Mechanics*, 339:357–390, 1997.

[15] R. W. C. P. Verstappen. On restraining the production of small scales of motion in a turbulent channel flow. *Computers & Fluids*, 37:887–897, 2008.

[16] F. X. Trias, a. Gorobets, a. Oliva, and C. D. Pérez-Segarra. DNS and regularization modeling of a turbulent differentially heated cavity of aspect ratio 5. *International Journal of Heat and Mass Transfer*, 57(1):171–182, 2013.

[17] F. X. Trias and R. W C P Verstappen. On the construction of discrete filters for symmetry-preserving regularization models. *Computers and Fluids*, 40(1):139–148, 2011.

[18] M. Calaf, C. Meneveau, and J. Meyers. Large eddy simulation study of fully developed wind-turbine array boundary layers. *Physics of Fluids*, 22(2010):015110, 2010.

[19] R. Mittal and G. Iaccarino. Immersed Boundary Methods. *Annual Review of Fluid Mechanics*, 37:239–261, 2005.

[20] C. Bogey, N. de Cacqueray, and C. Bailly. A shock-capturing methodology based on adaptative spatial filtering for high-order non-linear computations. *Journal of Computational Physics*, 228(5):1447–1465, 2009.

[21] M. Germano. Differential filters for the large eddy numerical simulation of turbulent flows. *Physics of Fluids*, 29:1755, 1986.

[22] P. Sagaut and R. Grohens. Discrete filters for large eddy simulation. *International Journal for Numerical Methods in Fluids*, 31(1997):1195–1220, 1999.

[23] A. W. Vreman. The adjoint filter operator in large-eddy simulation of turbulent flow. *Physics of Fluids*, 16(6):2012–2022, 2004.

[24] B. Engquist, P. Lotstedt, and B. Sjogreen. Nonlinear filters for efficient shock computation. *Mathematics of Computation*, 52(186):509–537, 1989.

[25] R. W. C. P. Verstappen and A. E. P. Veldman. Symmetry-preserving discretization of turbulent flow. *Journal of Computational Physics*, 187:343–368, 2003.

[26] W. Rozema, J. C. Kok, R.W.C.P. Verstappen, and A.E.P. Veldman. A symmetry-preserving discretisation and regularisation model for compressible flow with application to turbulent channel flow. *Journal of Turbulence*, 15(March 2015):386–410, 2014.

[27] F. X. Trias, O. Lehmkuhl, A. Oliva, C. D. Pérez-Segarra, and R.W.C.P. Verstappen. Symmetry-preserving discretization of Navier-Stokes equations on collocated unstructured grids. *Journal of Computational Physics*, 258:246–267, 2014.

[28] O. Lehmkuhl, I. Rodríguez, R. Borrell, and A. Oliva. Low-frequency unsteadiness in the vortex formation region of a circular cylinder. *Physics of Fluids*, 25(8):85109, 2013.

[29] P. Sagaut. *Large eddy simulation for incompressible flows: an introduction*. Springer Science & Business Media, New York, 2006.

[30] J. S. Mullen and P. F. Fischer. Filtering techniques for complex geometry fluid flows. *Communications in Numerical Methods in Engineering*, 15:9–18, 1999.

[31] N. Troldborg, J. N. Sørensen, and R. Mikkelsen. Actuator Line Simulation of Wake of Wind Turbine Operating in Turbulent Inflow. *Journal of Physics: Conference Series*, 75:12063, 2007.

[32] B. P. Leonard. A stable and accurate convective modelling procedure based on quadratic upstream interpolation. *Computer Methods in Applied Mechanics and Engineering*, 19(1):59–98, 1979.

[33] A. Harten. High Resolution Schemes for Hyperbolic Conservation Laws. *Journal of Computational Physics*, 135:260–278, 1983.

[34] H. C. Yee. Nasa technical memorandum 101088: A class of high-resolution explicit and implicit shock-capturing methods. Technical report, NASA, 1989.

[35] L. I. Rudin, S. Osher, and E. Fatemi. Nonlinear total variation based noise removal algorithms. *Physica D: Nonlinear Phenomena*, 60:259–268, 1992.

[36] B. J. Perot. Discrete Conservation Properties of Unstructured Mesh Schemes. *Annual Review of Fluid Mechanics*, 43(1):299–318, 2011.

[37] M. Galassi, J. Davies, B. Gough, G. Jungman, P. Alken, and R. Ulerich. GNU Scientific Library, 2015.

Appendix 4.A Tested filters

Adaptative filters are controlled at each o cell by a filter ratio ϵ_o parameter or a characteristic cut-off $\epsilon_o\Delta_o$ length. To ensure the accomplishment of conditions of Section 4.3, limitations on ϵ_o are imposed. Descriptions of filters used in 4.5 and the bounds imposed on their filter ratios are included in this appendix.

4.A.1 The Laplacian filter

The Laplacian filter used in this work is an adaptation to any mesh of the differential filter that approximates convolution filters in [22]. It reads:

$$\hat{\phi}_o = \phi_o + \frac{(\epsilon_o \Omega_o^{1/3})^2}{24\Omega_o} \sum_{p \in N_o} (\phi_p - \phi_o) \frac{A_{\underline{op}}}{\boldsymbol{n}_{\underline{\boldsymbol{op}}} \cdot \boldsymbol{r}_{\underline{\boldsymbol{op}}}} \tag{4.44}$$

Where $A_{\underline{op}}$ is the area of the interface between the o and p control volumes, $\boldsymbol{n}_{\underline{\boldsymbol{op}}}$ is the unitary vector normal to the interface oriented from o to p and $\boldsymbol{r}_{\underline{\boldsymbol{op}}}$ is the vector from the cell center of o to the cell center of p. Here, the characteristic $\Delta_o = \Omega_o^{1/3}$, and Ω_o is the volume of the o cell. LED or EC criteria can be imposed with:

$$\epsilon_o^2 \leq \frac{24\Omega_o^{1/3}}{\sigma \sum_{p \in N_o} \frac{A_{\underline{op}}}{\boldsymbol{n}_{\underline{\boldsymbol{op}}} \cdot \boldsymbol{r}_{\underline{\boldsymbol{op}}}}} \tag{4.45}$$

Where $\sigma = 1$ to impose LED and $\sigma = 2$ to impose EC. Tests in Section 4.5 have been conducted using this limitations.

4.A.2 The Box filter

The Box filter is computed as an averaging of the values of a neighborhood of a CV. It is the adaptative version of the filter in [23].

$$\hat{\phi}_o = \frac{1}{\epsilon_o}\left(\phi_o + \frac{(\epsilon_o - 1)}{\sum_{p\in N_o}\Omega_p}\sum_{p\in N_o}\phi_p\Omega_p\right) \tag{4.46}$$

LED is imposed with $1 \leq \epsilon_o$ and EC with $1 \leq 2$. This restrictions have been applied on tests described in Section 4.5.

Appendix 4.B Filter TVD analysis on the infinitesimal filter limit

Conditions (4.19) and (4.21) in Section 4.3.7 are equivalent. For a general filter, the elements of K of equation (4.21) read:

$$k_{o\,o} = \overline{\overline{N_o}} - f_{o\,o}^2\overline{\overline{N_o}} - \sum_{p\in N_o} f_{p\,o}\left(\overline{\overline{N_p}}f_{p\,o} - 2f_{o\,o} - \sum_{q\in N_o\cap N_p} f_{q\,o}\right) \tag{4.47}$$

$$\begin{aligned} k_{o\,p} \overset{*}{=}\ & -1 - f_{o\,p}\left(\overline{\overline{N_o}}f_{o\,o} - \sum_{q\in N_o} f_{q\,o}\right) - f_{p\,p}\left(\overline{\overline{N_p}}f_{p\,o} - f_{o\,o} - \sum_{q\in N_o\cap N_p} f_{q\,o}\right) - \ldots \\ & \ldots - \sum_{q\in No\cap N_p} f_{q\,p}\left(\overline{\overline{N_q}}f_{q\,o} - f_{o\,o} - \sum_{r\in N_o\cap N_q} f_{r\,o}\right) + \sum_{\substack{q\in N_p \\ q\notin N_o}} f_{q\,p}\sum_{r\in N_o\cap N_q} f_{r\,o} \end{aligned} \tag{4.48}$$

$$k_{o\,q} \overset{**}{=} -1 + \sum_{p\in N_o\cap N_q}\left[f_{p\,o}f_{q\,q} - f_{p\,q}\left(N_p f_{p\,o} - f_{o\,o} - \sum_{r\in N_o\cap N_p} f_{r\,o}\right)\right] \tag{4.49}$$

Equality (4.48) stands for $p \in N_o$ while equality (4.49) stands for $q \in N_p$ with $p \in N_o$ and $q \notin N_o$. Now, we perform an analysis for normalized filter matrices F with $f_{o\,p} = \varepsilon f^*_{o\,p}$ and $f_{o\,o} = 1 - \varepsilon\sum_{p\in N_o} f^*_{o\,p}$. Parameter $\varepsilon \ll 1$ is positive and $f^*_{o\,p} \sim$

1 $\forall o \neq p$. We write $S_o = \sum_{q \in N_o} f^*_{o\,q}$, $R_o = \sum_{q \in N_o} f^*_{q\,o}$ and $T_{o\,p} = \sum_{q \in N_o \cap N_p} (f^*_{q\,o} + f^*_{q\,p})$. With them, we get:

$$\lim_{\varepsilon \to 0^+} k_{o\,o} = \lim_{\varepsilon \to 0^+} 2\varepsilon \left(\overline{\overline{N_o}} S_o + R_o \right) + \mathcal{O}(\varepsilon^2) \simeq 0^+ \tag{4.50}$$

$$\lim_{\varepsilon \to 0^+} k_{o\,p} \overset{*}{=} \lim_{\varepsilon \to 0^+} -\varepsilon \left(\overline{\overline{N_o}} f^*_{o\,p} + S_o + \overline{\overline{N_p}} f^*_{p\,o} + S_p - T_{o\,p} \right) + \mathcal{O}(\varepsilon^2) \simeq 0^- \tag{4.51}$$

$$\lim_{\varepsilon \to 0^+} k_{o\,q} \overset{**}{=} \lim_{\varepsilon \to 0^+} \varepsilon \sum_{p \in N_o \cap N_q} \left(f^*_{p\,q} + f_{p\,o} \right) + \mathcal{O}(\varepsilon^2) \simeq 0^+ \tag{4.52}$$

Now, for K to be $\succeq 0$, it should be Diagonal Dominant, so

$$\begin{aligned} \sigma_o = \lim_{\varepsilon \to 0^+} k_{o\,o} - \sum_{p \neq o} |k_{o\,p}| \simeq 2\varepsilon \left(\overline{\overline{N_o}} S_o + R_o \right) - ... \\ - \varepsilon \sum_{p \in N_o} \left(\overline{\overline{N_o}} f^*_{o\,p} + S_o + \overline{\overline{N_p}} f^*_{p\,o} + S_p - T_{o\,p} \right) + ... \\ ... + \varepsilon \sum_{\substack{q \in N_p \\ q \notin N_o \\ p \in N_o}} \sum_{p \in N_o \cap N_q} \left(f^*_{p\,q} + f^*_{p\,o} \right) \end{aligned} \tag{4.53}$$

should be greater or equal to zero for all control volumes. We have studied various common situations on uniform 1D, 2D and 3D meshes. It has been found that only 1D filtering with only one neighbor leads to TVD filters for all input fields fields. Hence, K is not always diagonally dominant and we can not proof its positive definiteness. In conclusion, filters are not necessarily TVD at the infinitesimal limit. We remark that this result has been obtained with $||\mathsf{G}(\boldsymbol{\phi})||_2$ instead of $||\mathsf{G}(\boldsymbol{\phi})||_1$, which is the common TVD norm in the compressible flow literature.

Appendix 4.C Equivalences between filter strength parameters

The relationships between the filter widths, filter strength and filter ratios that, for constant meshes and filters, make the weights of neighbor cells equal are:

$$\varepsilon_B = \left(1 - \frac{\varepsilon_L^2 \overline{\overline{N}}}{24} \right)^{-1} \tag{4.54}$$

$$\varepsilon_{CLF} = \frac{\varepsilon_L^2}{24} \tag{4.55}$$

Where ε_B is the filter ratio of the Box filter, ε_{CLF} is the filter strength of the CLF filter, ε_L is the filter width of the Laplacian filters and $\overline{\overline{N}}$ is the average number of neighbors of the stencil. These relations apply for every cell of a constant mesh.

However, f_{oo} and f_{op} elements of the Box filters can not be equal to those of differential filters and the same time at cells near boundaries or cells with a number of neighbors in the stencil different to $\overline{\overline{N}}$. In any case, in order to compare filters with parameters "as equivalent as possible", we use relation (4.54).

5

Filtering on Numerical Schemes for Compressible Flows

5.1 Introduction

This chapter is focused on the analysis of the effects of the filters developed in chapter 4 on the simulation of compressible turbulent flow with the Symmetry Preserving (SP) schemes for compressible flows expounded in chapter 2. The primary purpose of filtering in these simulations is to cure the solutions from wiggles. Wiggles (artificial numerical oscillations on the solutions) appear in simulations when energy is injected faster than it is evacuated to the smallest flow scales. Then, the small scales modes keep growing in amplitude until they affect the overall solution. Eliminating wiggles or preventing their appearance in flows with shocks has been a common research topic since the first years of numerical simulations of transport equations, especially in compressible flow. Bram van Leer gives a historical account of this in [1]. From a spectral point of view, a shock is a Heaviside step in the shock-normal velocity component u_n. Thus, in the Fourier space,

$$\widetilde{u_n} = \frac{1}{2}\left(\frac{1}{i\pi\xi} + \delta(\xi)\right),$$

which is not $\mathcal{L}^1$ and does not converge everywhere because it has too much energy at high frequencies. Because of this, flows with discontinuities like shock waves produce wiggles. Indeed, most of the numerical schemes for compressible flow are

designed with the primary aim of counteracting wiggles. For example, the famous JST method [2] detects, at each time iteration, zones where instabilities/wiggles are produced and then applies local artificial diffusion to locally eliminate them while the rest of the flow is treated with a lesser diffusive methodology. But the most common way to prevent wiggles growth is numerical flux splitting and using upwind-biased solutions of the Riemann problem at interfaces. Some examples of this type of approximation are Godunov, [3], Harten et al. [4], Roe [5] and the ENO Scheme [6]. Finally, others like Engquist et al. [7] and, more recently, Bogey et al. [8] have also developed shock-capturing schemes based on isotropic (not direction-depending) filters.

But in LES simulations wiggles can also slowly and steadily grow in flows without discontinuities. In this case, this happens because the discretizations admit solutions that lie in the kernels of the fundamental operators of the equations. Thus, when energy is injected to these modes (flow scales), there are no mechanisms that can return it to the subspace of flow scales that lie on the pre-image of the operators. Energy then piles up in the kernel flow scales and, at a slow pace, it makes them grow and distort the solutions until the boundaries are affected or some value grows too much, turning the simulations unstable. This mechanism can be cured by filtering the solutions or adding artificial diffusion because neither filtering nor diffusion operators have non-trivial kernels. Furthermore, as diffusion and diffusive filtering are more aggressive with small scales, their effect is more noticeable on the targeted flow scales and lesser to the big flow scales. Actually, Eddy Viscosity LES methods do essentially the same that has been described here in simulations where convection sends an excess of energy to the smallest mesh scales that the molecular diffusion alone can not dissipate [9, 10]. For this reason, even in schemes that can handle discontinuity-caused wiggles, it is also common to apply some degree of artificial diffusion or filtering in smooth regions. This is done, for example, in [8] and [11].

In this chapter I only apply filtering in regions with oscillations, keeping most of the fluid domain unaffected. With this approach, the large flow scales should be less affected by the introduced diffusion. The numerical methodology to include filtering in the compressible flow scheme is detailed in section 5.2. Next, in section 5.3, the methodology is assessed with the 2D isentropic vortex already studied in chapter 2. Additionally, the effect of the discrete filtering with the filters developed in chapter 4 when simulating the Taylor-Green vortex using eddy viscosity with test filtering is also reported. To show how the methodologies developed here can also be useful in the simulation of compressible flows with shocks, simulations of the described methodology on the Sod shock tube case are reported in section 5.5. Finally, the

chapter is closed with conclusions.

5.2 Numerical Method

There are multiple possibilities to combine Symmetry Preserving numerical schemes and explicit filtering methodologies. They are summarized alongside with the specific choices made for the tests in this chapter in table 5.1.

Table 5.1: Table : Parameters when filtering SP schemes.

Parameter	Present tests	Reference
SP scheme	KEP, RZM and $MRZM$	chap. 2
Time int. scheme	TVD Runge-Kutta 3	chap. 2
Discrete filter	$CDLF$	chap. 4
Filtering frequency	Every Runge-Kutta sub-step	alg. 1
Filter driver parameter(s)	$\{\rho \quad \rho u^1 \quad \rho u^2 \quad \rho u^3 \quad \rho E_t\}$	chap.4
Filter driver Operator	$FR_o = AbsExt_o(\phi_\bullet)$	eq. 5.1
Variations growth limit	EC	chap. 4

The filter driver is calculated with the oscillations detector defined hereby:

$$AbsExt_o(\phi_\bullet) = \begin{cases} 1 & \text{if} \quad (\phi_o - \phi_p)(\phi_o - \phi_q) > 0 \quad \forall\{p, q\} \in N_o \\ 0 & \text{otherwise} \end{cases} , \quad (5.1)$$

which only activates filtering at points where ϕ is strictly a local maximum or minimum. This reduces the number of points where filtering is applied with respect to the methodologies of chap. 4, achieving a lesser dissipative overall method. If filtering was applied too often, this would result in early and excessive dissipation of kinetic energy into internal energy. A mechanism to turn the dissipated kinetic energy into internal energy has not been explicitly provided in the present methodology, but the First Principle of Thermodynamics is respected after the conservation of the filters applied on $(\rho E_t)_\bullet$. Therefore, all dissipated kinetic energy is transformed into internal energy. The filtering intensity parameter described here is locally binary. For a certain mesh element (control volume) it applies full filtering (with the EC restriction) or it does not filter at all. In the compressible flow literature, this is not a common procedure and the intensity of filtering or artificial dissipation is done according to some scaling factor. For example, Ducros et al. [12] used a scaling factor based on the Laplacian of pressure multiplied by the ratio between the local

divergence of velocity and the sum of the local vorticity and the local divergence of velocity. I do not include this kind of analysis here.

Altogether, the algorithm to include filtering in the numerical scheme implemented and tested here reads:

Algorithm 1 Time iteration including filtering

procedure EXPLICIT TIME ITERATION
  for each s Runge-Kutta substep $\in \{1, 2, 3...N_{RK}\}$ **do**
    for each $\phi \in \{\rho \quad \rho u^1 \quad \rho u^2 \quad \rho u^3 \quad \rho E_t\}$ **do**
      for each o from 1 to N_{nodes} **do**
        $\phi_o \leftarrow \sum_k \alpha_{sk} \phi_o^{n(+k)} + \Delta t \sum_k \beta_{sk} L(\phi_\bullet^{n(+k)})$
      end for
      for each o from 1 to N_{nodes} **do**
        $FR_o \leftarrow AbsExt_o(\phi_\bullet)$
      end for
      for each o from 1 to N_{nodes} **do**
        $\mathsf{F}_o \leftarrow \mathsf{CDLF}(EC)_o(FR_\bullet)$
      end for
      $\phi_\bullet^{n(+s)} \leftarrow \mathsf{F}_\bullet(\phi_\bullet)$
    end for
  end for
  $\phi_\bullet^{n+1} \leftarrow \phi_\bullet^{n(+N_{RK})}$
end procedure

where $\mathsf{L}(\phi_\bullet^{n(+k)})$ accounts for the sum of all the numerical fluxes (or spatial differential operators in the case of finite differences).

5.3 2D Isentropic Vortex

The 2D Isentropic Vortex case has been already studied for several different SP schemes is chapter 2 and it was found that RZM and MRZM schemes are significantly more stable in time than JST, KOK and KEP. Furthermore, it was seen that unstructured meshes trigger early blow-ups. Filtering significantly delays these blow-ups (see table 5.2), specially in the unstructured meshes, where filtering is more likely to be activated because local maxima or minima are more prone to appear. The simulations in coarse meshes also appear to be more stable when applying filtering because it is more prone to be activated and more diffusion is added.

Table 5.2: : Blow-Up times for the 2D Isentropic Stationary Vortex case. Unfiltered (upper) and filtered (lower) algorithms values.

Mesh	*JST*	*KEP*	*KOK*	*RZM*	*MRZM*
str80	38	26	26	529	277
	323	223	817	> 1000	706
str200	20	34	33	358	282
	331	385	386	472	810
uns80	5.8	9.3	13	76	137
	> 1000	> 1000	> 1000	> 1000	> 1000
uns200	16	33	25	64	67
	16	33	25	433	> 1000

But enhancing stability by means of diffusion destroys kinetic energy and the numerical errors increase. Figures 5.1 and 5.2 show how this happens for the different studied meshes and a selection of the studied schemes. These figures are complemented with plots of the vertical velocity profiles over the same line at the same simulation time to show that filtering smears the vortex but it still persists (Figs. 5.3 and 5.4).

Structured meshes with RZM or MRZM allow the simulations to match the analytic values of both magnitudes very well. In the case of unstructured meshes, it seems that the truncation error associated with them plays a density diffusion role for all schemes (Fig. 5.2) which is in the same order of the diffusion associated with the applied filtering. However, in terms of velocity fields on unstructured meshes (Fig. 5.4), diffusion associated with filtering is clearly higher than that associated with truncation errors for KEP and MRZM. Rozema's scheme, however, behaves differently and the specific combination of filtering and scheme tested here is not so severe. This effect can be caused by the non-reflecting output boundary conditions (BBCC) that have been imposed for the reasons given in chapter 2. If a scheme produces oscillations near the boundaries, these BBCC allow mass outflow, resulting in what looks like a higher diffusion caused by the overall scheme. This would explain the apparent high diffusion on unstructured meshes and that MRZM and KEP were much more diffusive in terms of mass than RZM. Other kind of BBCC would help to alleviate this problem, but then the tests would not be comparable to those performed in chapter 2. Therefore, I avoid to perform this analysis here and only Fig. 5.5 is included to show how the periodic boundary conditions reduce the "apparent dissipation".

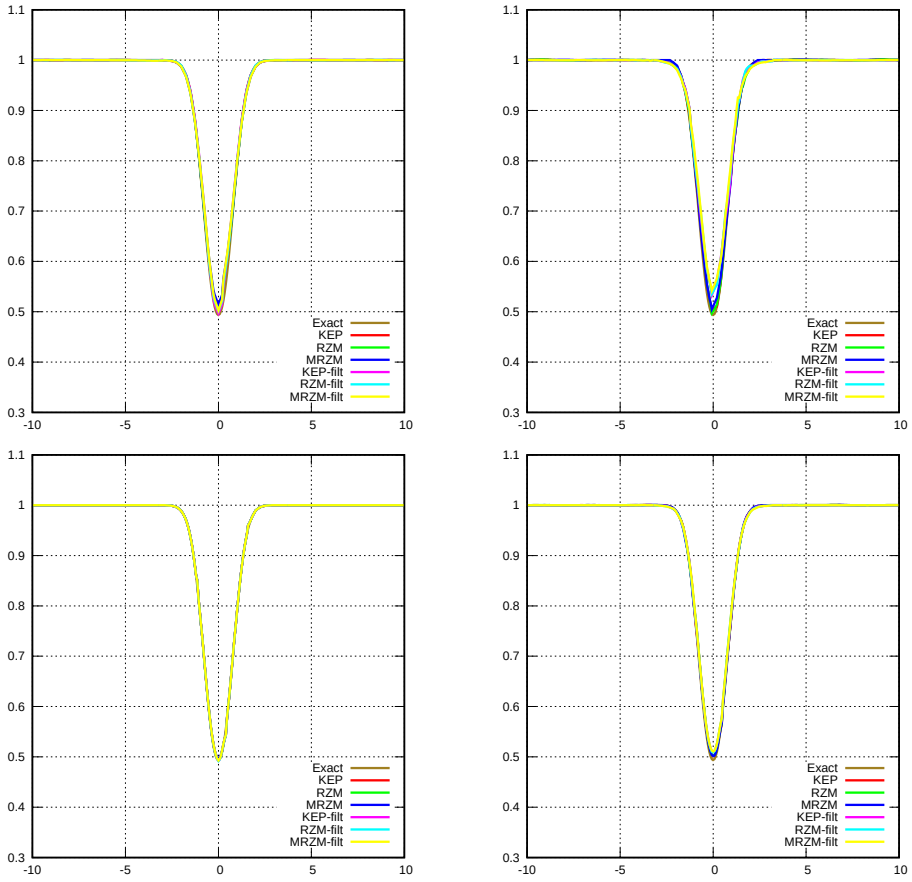

Figure 5.1: Density ρ over line $x \in [-10, 10]$; $y = 0$ at $t = 3$ in the 2D isentropic vortex case with different SP schemes on various meshes. From left to right and from top to bottom: str80, unstr80, str200 and unstr200.

5.4 Taylor-Green Vortex

Some of the simulations on the Taylor-Green Vortex reported in section 2.4 are performed including the filtering algorithm described in section 5.2 to observe the effects of filtering in the simulation of turbulent flow with the present schemes. In homogeneous turbulent flows like this, filtering would prevent wiggle growth and improve stability and accuracy of long-period simulations at the cost of some punc-

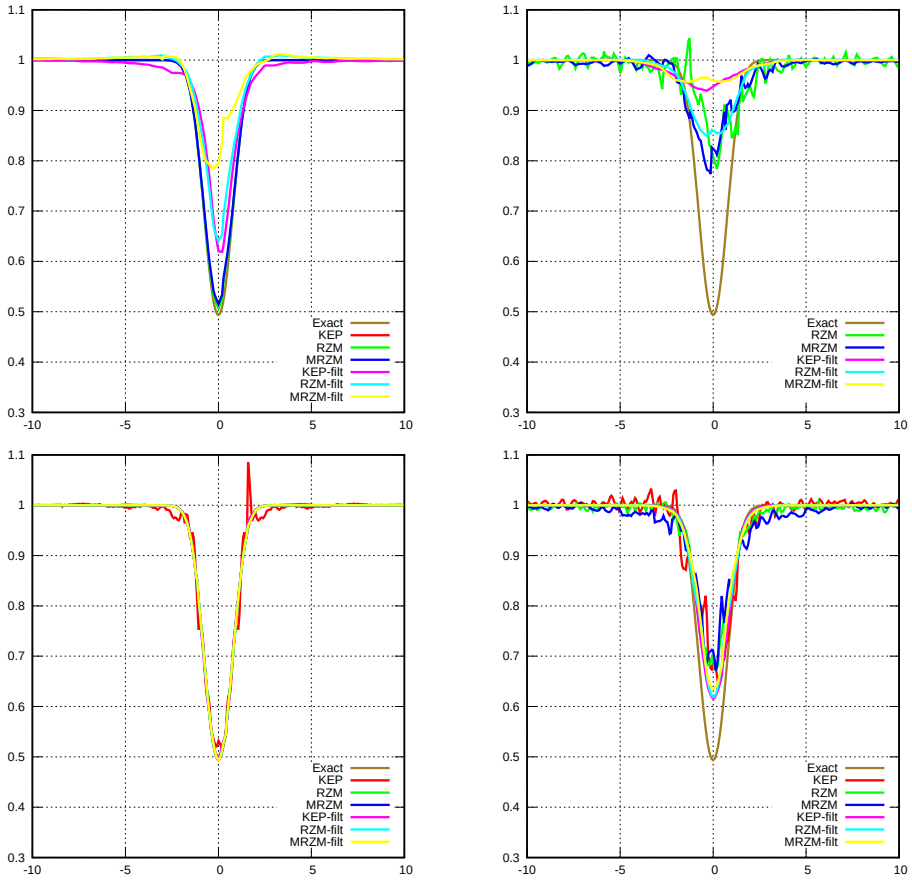

Figure 5.2: Density ρ over line $x \in [-10, 10]$; $y = 0$ at $t = 30$ in the 2D isentropic vortex case with different SP schemes on various meshes. From left to right and from top to bottom: str80, unstr80, str200 and unstr200.

tual numerical diffusion. This test allows to qualitatively observe the effect the evolution of kinetic energy. I want to stress here that the boundary conditions used for this test are periodic and not of outlet-type like in the isentropic vortex.

Figure 5.6 shows the effect of filtering in a set-up with RZM, WALE and Cartesian meshes. The finer the mesh, the lesser the effect of filtering. In all cases, filtering increased the dissipation peak. Moreover, appears earlier with cart32. With this mesh,

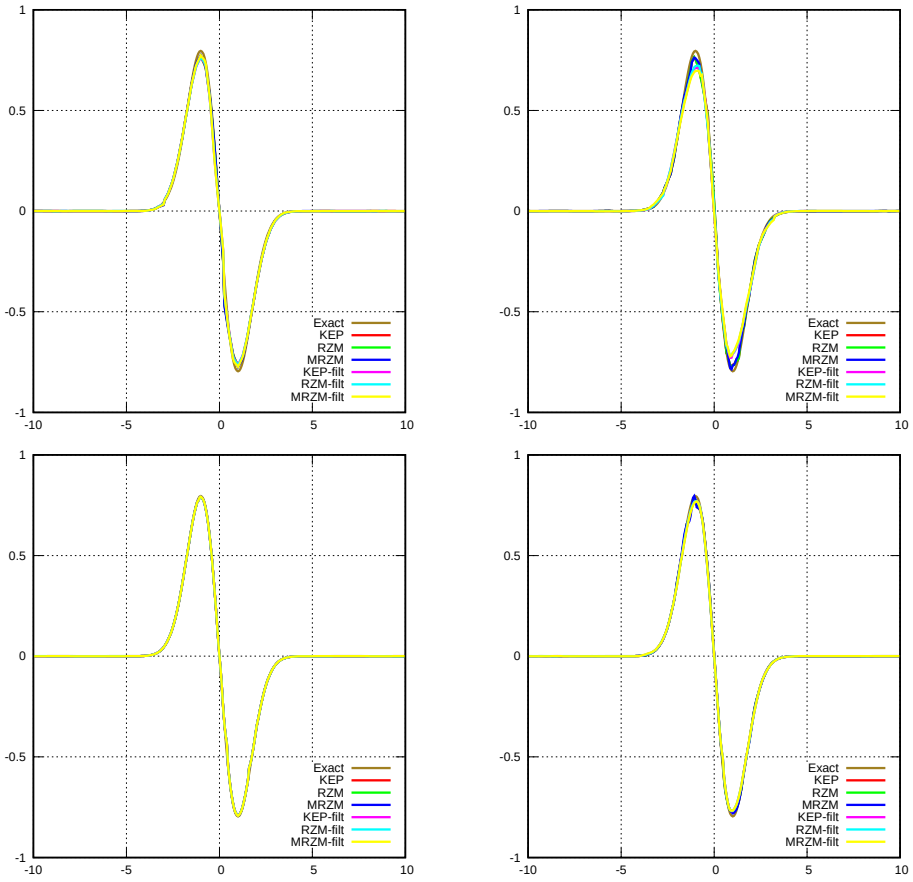

Figure 5.3: Vertical velocity v over line $x \in [-10, 10]$; $y = 0$ at $t = 3$ in the 2D isentropic vortex case with different SP schemes on various meshes. From left to right and from top to bottom: str80, unstr80, str200 and unstr200.

it seems that the major source of error is early transition to turbulence and its associated dissipation growth triggered by the lack of accuracy in the initial solution, which becomes more unstable than in finer meshes. In Figure 5.7 the results with the cart32 with a time shift of 1.44 have been plotted alongside the reference results of [13]. The time shift was chosen to make the plots coincide at the point where $dK/dt = 0.002$, i.e., the instant when dissipation starts to steeply increase following, approximately, a straight line. I consider this is the instant of turbulent transition.

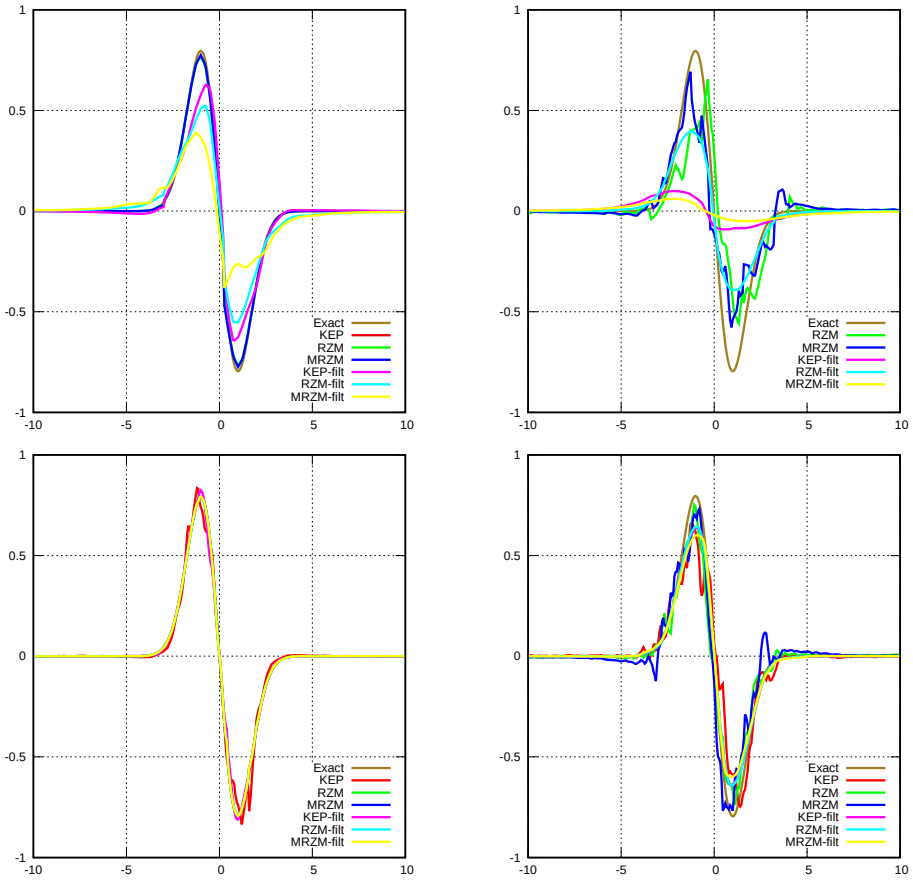

Figure 5.4: Vertical velocity v over line $x \in [-10, 10]$; $y = 0$ at $t = 30$ in the 2D isentropic vortex case with different SP schemes on various meshes. From left to right and from top to bottom: str80, unstr80, str200 and unstr200.

Overall, filtering slightly modified the results but does not seem to spoil the simulations.

Figure 5.8 compares the filtered and unfiltered results of RZM and MRZM on unstr64. RZM was stable regardless of filtering while MRZM shown an early blow-up when not applying the filter. Filtering does not spoil the results and enhances stability, allowing the use of MRZM. Figure 5.10 shows the effect of filtering on un-

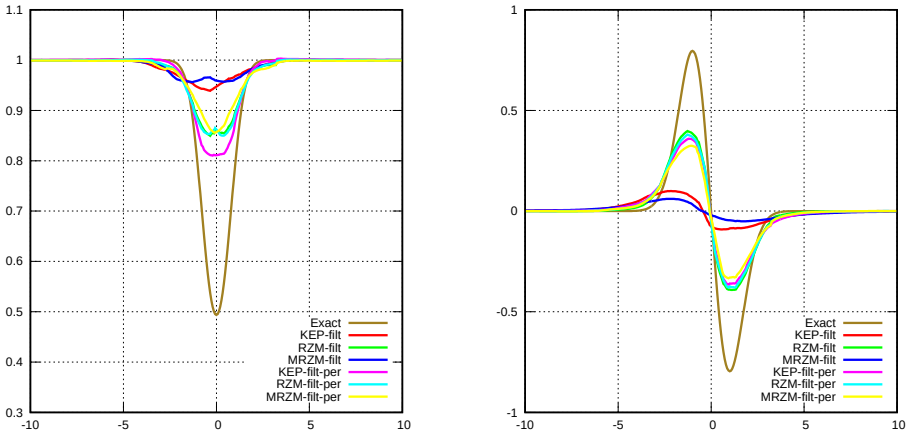

Figure 5.5: Density *rho* (left) and Vertical velocity v over line $x \in [-10, 10]$; $y = 0$ at $t = 3$ in the 2D isentropic vortex case with different SP schemes on unstr80 using filtering. Outlet and periodic boundary conditions.

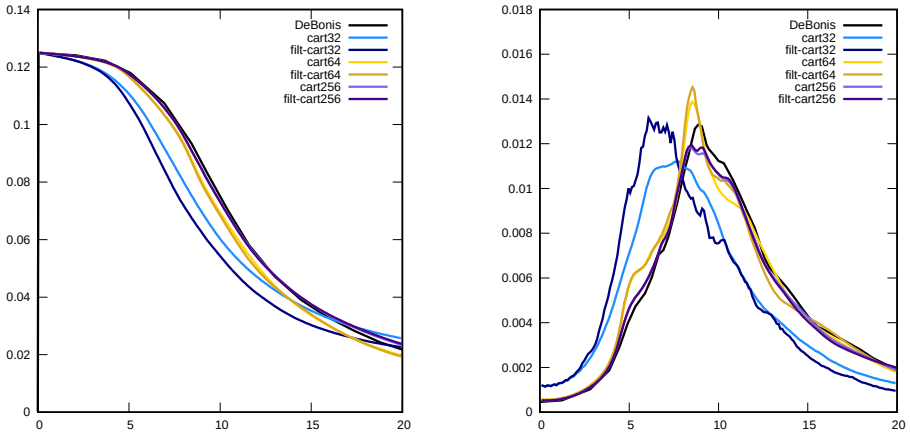

Figure 5.6: Evolution in time of magnitudes of the Taylor-Green case with RZM, WALE and various cartesian meshes. Comparison of unfiltered and filtered algorithms. Left: Kinetic energy evolution. Right: Dissipation $\frac{dK}{dt}$.

structured meshes with RZM. The finer the mesh, the lesser is the effect of filtering. One could not easily determine if filtered solutions are more or less accurate than the

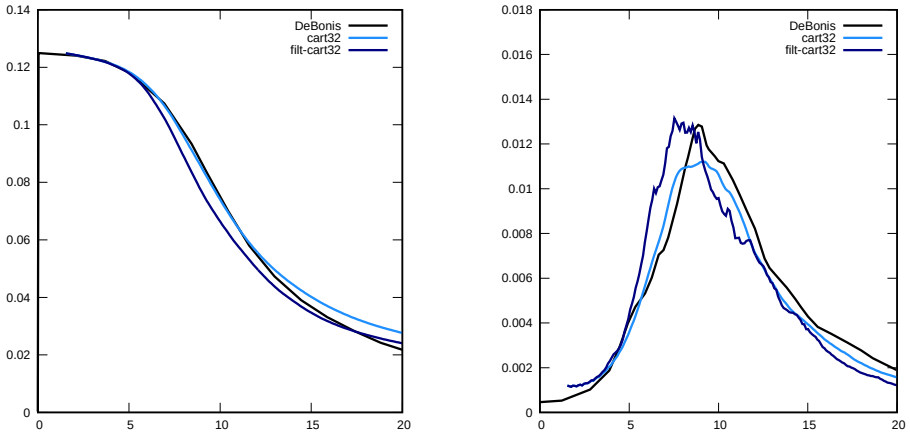

Figure 5.7: Evolution in time of magnitudes of the Taylor-Green case with RZM, WALE and various cart32 mesh. Time shift of 1.44 in simulated results. Comparison of unfiltered and filtered algorithms. Left: Kinetic energy evolution. Right: Dissipation $\frac{dK}{dt}$.

unfiltered. Shifting the results 1.71 time units for the same reasons given before, one gets Figures 5.9 and 5.11. Unstructured meshes trigger early instabilization of flows as it happens with the cart32 mesh. A study with much finer meshes would allow to determine if they end up by reproducing the initial flow evolution with enough accuracy as to prevent this early instabilizations with unstructured discretizations. Filtering does not seem to have any remarkable effect on this phenomenon with the present settings.

5.5 Flows with shocks

The present methodology has also been used to stabilise the simulations of a shock tube. The case studies the evolution of an ideal gas in a 1D pipe with adiabatic and no shear stress boundary conditions at the walls. In the beginning, all the gas is at rest with two distinct regions at different pressure and density. These regions are separated by a membrane until the time starts to run. Then, it vanishes causing a shock-wave travelling from the high-pressure to low-pressure (left to right) and an expansion wave travelling in the opposite direction (right to left). Because there is a shock wave, simulations with numerical schemes without dedicated shock capturing methodologies blow up. For further details about the shock tube test see [14].

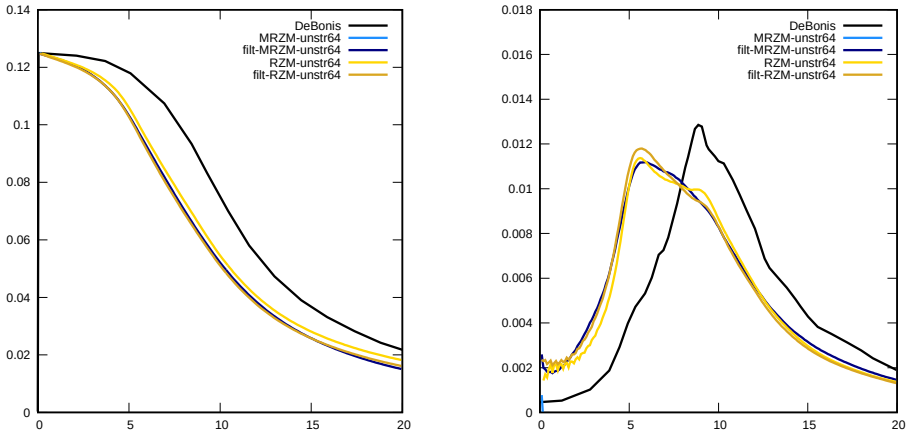

Figure 5.8: Evolution in time of magnitudes of the Taylor-Green case with RZM and MRZM, WALE and unstr64. Comparison of unfiltered and filtered algorithms. Left: Kinetic energy evolution. Right: Dissipation $\frac{dK}{dt}$.

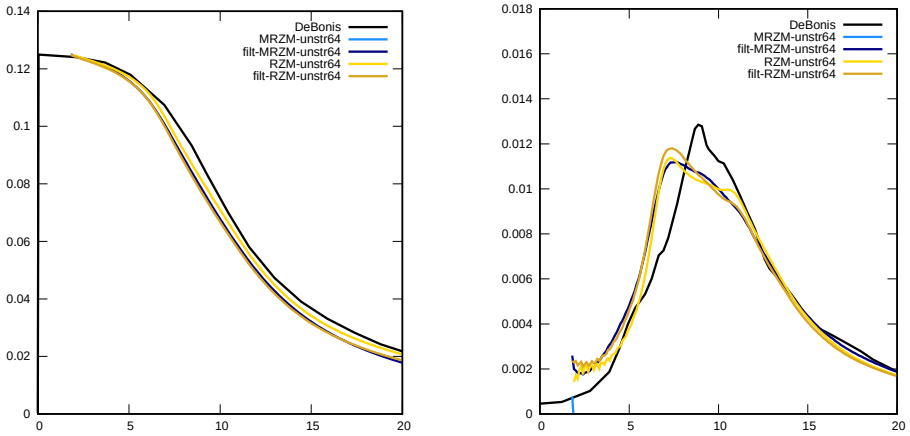

Figure 5.9: Evolution in time of magnitudes of the Taylor-Green case with RZM and MRZM, WALE and the unstr64 shifted 1.71 t.u. .Comparison of unfiltered and filtered algorithms. Left: Kinetic energy evolution. Right: Dissipation $\frac{dK}{dt}$.

The section of the pipe is a square $L \times 0.1L \times 0.1L$ in the test reported here. Table

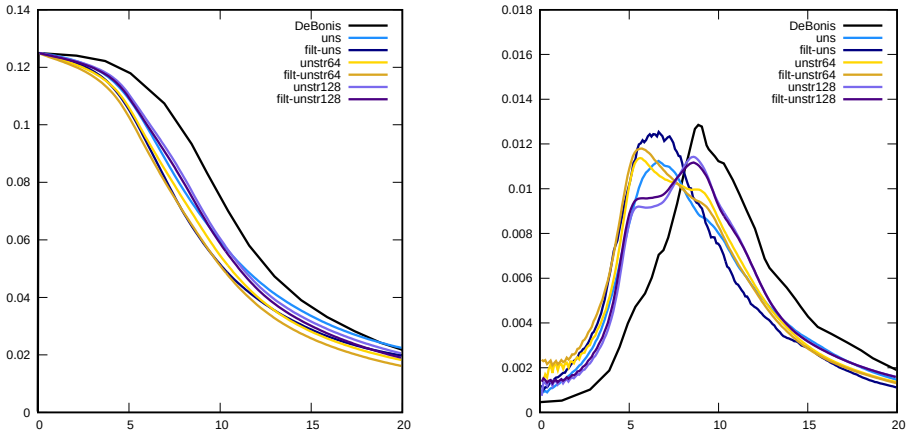

Figure 5.10: Evolution in time of magnitudes of the Taylor-Green case with RZM, WALE and the unstructured meshes. Comparison of unfiltered and filtered algorithms. Left: Kinetic energy evolution. Right: Dissipation $\frac{dK}{dt}$.

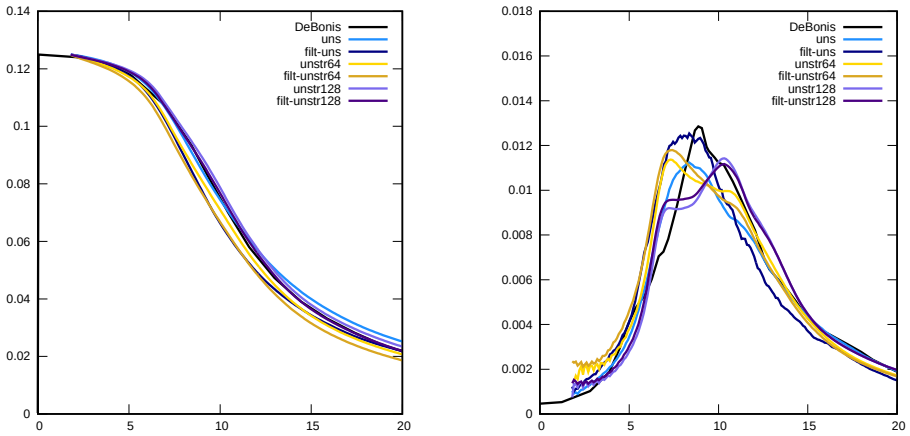

Figure 5.11: Evolution in time of magnitudes of the Taylor-Green case with RZM, WALE and the unstructured meshes. Simulated results shifted 1.71 t.u. in time. Comparison of unfiltered and filtered algorithms. Left: Kinetic energy evolution. Right: Dissipation $\frac{dK}{dt}$.

5.3 summarizes the meshes employed in these simulations. The unstructured mesh is produced from a surface seed of nearly equilateral triangles whose edge length is 0.01 times the length of the tube on the pipe walls, inlet an outlet.

Table 5.3: : Meshes in the shock tube case.

Name	Description	Cells
1d100	1D uniform hexa.	100
1d1000	1D uniform hexa.	1000
cart100	3D cartesian hexa.	10000
utube	3D unstruct. tetra.	93129

The results in Figure 5.12 compares the results with the present methodology with the evaluation of the exact solution at 100 equally spaced points. It shows how filtering on SP schemes allows the stable simulation of the 1D shock at the cost of slightly smearing both the shock and expansion waves. Since the flow is 1D, the instability detector implemented here does not activate with the Cartesian mesh cart100 as there are no control volumes where $AbsExt_o \neq 0$ (see equation 5.1). The shock reaches at the same time all the CV in a square section and there are no absolute extrema. Hence, the oscillations in the result with this mesh are because the shock is not well detected. Implementing shock-specific filter activators like in Ducros et al. [15] would resolve this problem. The research related with this topic is out of the scope of this thesis.

5.6 Conclusions

An algorithm for the application of filtering on numerical simulations of compressible flow has been reported and tested on the isentropic vortex and the Taylor Green vortex cases.

From these tests, it has been shown that the proposed methodology improves stability in the isentropic vortex case. However, it seems that the interference of the methodology with the outlet boundary conditions necessary to reproduce the test in chapter 2 distorts the comparisons. This has been shown with a specific test in which results obtained with periodic boundary conditions have been contrasted with results using outlet boundary conditions.

The tests on the Taylor Green Vortex show how the applied filtering does not seem to spoil the results obtained without filtering. This result is interesting because this case encompasses the destabilization of a laminar flow into turbulence and the

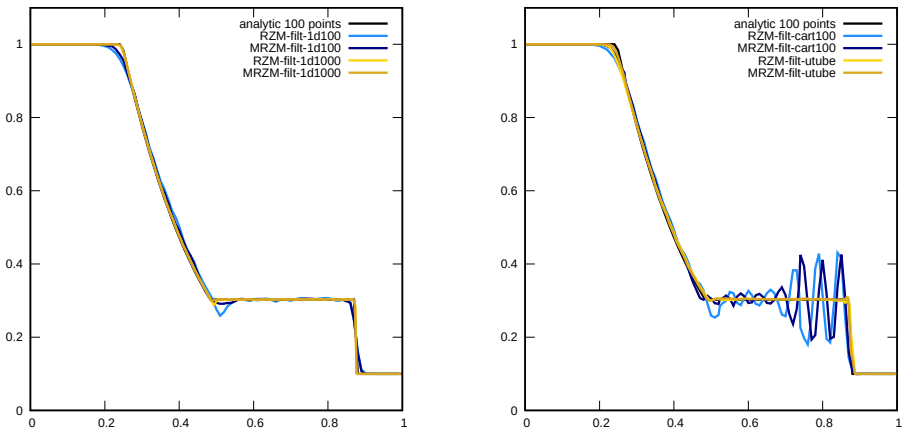

Figure 5.12: Pressure along longitudinal axis of the shock tube problem at $t = 0.2136$ with various meshes. The reference solution consists of the evaluation of the analytical solution at 100 equally spaced points. Left: 1D meshes. Right: 3D meshes.

ulterior dissipation of the kinetic energy. Strongly diffusive methodologies prevent the simulations from reproducing this behaviour as kinetic energy is dissipated too fast. Poorly represented initial conditions due to a coarse discretization have been shown to trigger early transition to turbulence. However, a shift in the time variables of the simulated results shows how, once the transition has occurred, the presented schemes reproduce reasonably well, even in very coarse meshes, the reference solution. These results show that the principal objective of the thesis has been reached.

The results on the shock tube show that the developed methodology can also be used for shock-capturing. However, to this end, the instability detector implemented here is not satisfactory as shocks do not cause individual maxima or minima but rather create strong gradients on connected control volumes. There are several shock-dedicated detectors that would give better results than the one implemented here. Despite this, the rest of the methodology (i.e. the algorithm and filtering) enables simulations with shocks, even in unstructured meshes.

References

[1] B. Van Leer. Upwind and High-Resolution Methods for Compressible Flow : From Donor Cell to Residual-Distribution Schemes. *Communications in Computational Physics*, 1(2):192–206, 2006.

[2] Antony Jameson, Wolfgang Schmidt, and Eli Turkel. Numerical solution of the euler equations by finite volume methods using runge kutta time stepping schemes. In *14th fluid and plasma dynamics conference*, page 1259, 1981.

[3] S. K. Godunov. A difference method for numerical calculation of discontinuous solutions of the equations of hydrodynamics. *Math. Sbornik*, 47(89):271–306, 1959.

[4] A. Harten. High Resolution Schemes for Hyperbolic Conservation Laws. *Journal of Computational Physics*, 135:260–278, 1983.

[5] P. Roe. Characteristic-Based Schemes for the Euler Equations. *Annual Review of Fluid Mechanics*, 18(1):337–365, 1986.

[6] A. Harten, B. Engquist, S. Osher, and S. R. Chakravarthy. Uniformly high order accurate essentially non-oscillatory schemes. III. 47:3–47, 1987.

[7] B. Engquist, P. Lotstedt, and B. Sjogreen. Nonlinear filters for efficient shock computation. 52(186):509–537, 1989.

[8] C. Bogey, N. de Cacqueray, and C. Bailly. A shock-capturing methodology based on adaptative spatial filtering for high-order non-linear computations. *Journal of Computational Physics*, 228(5):1447–1465, 2009.

[9] R. Verstappen. How much eddy dissipation is needed to counterbalance the nonlinear production of small, unresolved scales in a large-eddy simulation of turbulence? *Computers & Fluids*, 2016.

[10] F. X. Trias, A. Gorobets, M. H. Silvis, R. W.C.P. Verstappen, and A. Oliva. A new subgrid characteristic length for turbulence simulations on anisotropic grids. *Physics of Fluids*, 29(11), 2017.

[11] J. C. Kok. A high-order low-dispersion symmetry-preserving finite-volume method for compressible flow on curvilinear grids. *Journal of Computational Physics*, 228(18):6811–6832, 2009.

[12] F. Ducros, F. Laporte, T. Soulères, V. Guinot, P. Moinat, and B. Caruelle. High-Order Fluxes for Conservative Skew-Symmetric-like Schemes in Structured Meshes: Application to Compressible Flows. *Journal of Computational Physics*, 161:114–139, 2000.

[13] J. DeBonis. Solutions of the Taylor-Green Vortex Problem Using High-Resolution Explicit Finite Difference Methods. 51^{s}t *AIAA Aerospace Sciences Meeting including the New Horizons Forum and Aerospace Exposition*, (February):1–9, 2013.

[14] G. A. Sod. A survey of numerical methods for compressible fluids. Technical report, Courant institute of mathematical science, New York University, New York, 1977.

[15] F. Ducros, V. Ferrand, F. Nicoud, C. Weber, D. Darracq, C. Gacherieu, and T. Poinsot. Large-eddy simulation of the shock/turbulence interaction. *Journal of Computational Physics*, 152(2):517–549, 1999.

6

Conclusions, Discussion and future work

Each of the chapters of the thesis contains its own conclusions section. Hence, the concluding remarks and conclusion here address the combination of the different parts and the follow-up work.

Firstly, the objectives of the thesis have been fulfilled: a methodology that couples filtering with SP simulations of compressible flow has been described and tested in chapter 5. As a result of this thesis, there is now a new methodology that prevents wiggle growth and enhances stability without significantly altering the accuracy of the numerical simulations of compressible flow.

But as the reader may have already noticed, this primary goal is not what has in the end required more innovation or effort. Quite unexpectedly, when I first tried to couple filtering and SP schemes, I realised that filtering was rather poorly described or understood in the literature. It forced me to improve the definition of filtering in CFD.

This detour from the initial planning in which I expected to close the coupling methodology in one chapter and then to report the results of simulations with complex phenomena was far from straightforward. At first, I programmed a coupling methodology. Then, the results I obtained with different filters made me question the properties of the discrete filters. At this point, I became aware that I did not know what properties were the filters should have. I decided to study them and I wrote the research peer-reviewed article of chapter 4 with my findings. Then, while studying the properties, I realized that the tests to compare filters reported in the literature were always coupled with other parts of a numerical simulation of fluid flow, entangling the study of filter properties with other matters that remained uncontrolled.

Consequently, I developed original tests that allow comparing their properties independently. During this process, I decided to use the eigenvectors of the Graph-Laplacian instead of the Laplacian matrix of a mesh as the test functions. I think that this idea may have influenced Trias et al. [1] and part of the following development of discretizations methodologies in the CTTC. Such a rather lateral contribution to the work of other researchers is another positive outcome of my work. Furthermore, I developed a technique to include vertex neighbours to operators derived from the Gauss theorem and a family of discrete filters that I have later used in some simulations.

During that period I also noticed that I could not find, in the literature, a justification in the analytical filter models to impose Total Variations Diminishing to discrete filters even when this property seemed necessary for proper discrete filter behaviour. So I decided to take another detour to better organise the properties of the analytical filter models reported in the literature.

In that study I revisited concepts of pure and applied mathematics to clarify the line that defines spatial filtering and reported it in chapter 3. I think that the discussion in that chapter (i.e., section 3.6) constitutes an important step forward in the understanding of the consistency of the LES models. It remarks the relevance of what I have called diffusive properties of filters and, even when I failed to reach an absolutely clear and unique fefinition of Extrema Diminishing in Appendix 3.A, I have shown how this property is necessary for an operator to be considered a filter in a space of representation. Furthermore, I have identified its mathematical context and the ideas that may lead others with a more solid knowledge in functional analysis to find the exact constraints that establish it.

Focusing on the other main branch of the thesis, that regarding SP schemes, I did not plan to conduct a comparison of existing schemes. I thought that Jameson's KEP scheme [2] was good enough for my purposes. But I did not find the reasoning behind the methodology to discretise the pressure gradient satisfactory, so I tried to derive a SP scheme. Shortly after, I got notice about the developments of Rozema [3], which seemed more consistent to me. Actually, seeing Rozema's scheme made me abandon my own research in this field because I thought that I could not improve his well-founded work. So once there were two different schemes to choose among, it followed that I needed a criterion to decide which one produced lesser wiggles and, for this reason, I conducted the comparisons in chapter 2. The result is that Rozema's is more stable than any other. In that chapter, I slightly modified Rozema's scheme, achieving a new scheme that performs better in unstructured meshes. I suspect that the improvement comes from the reduction of the dispersion error.

After all this, I think that this thesis points out to several lines of future work. First, the research in the comparison of SP schemes for compressible flow should be extended to other configurations to take into account near-wall behaviour, sound production and propagation, shear layer transitions and computing cost. Second, some pure mathematics work should be done to more precisely define the diffusive properties of filters and the consequences of not fulfilling them regarding existence and unicity of LES equations solutions. Third, the filter properties should also be imposed on explicit and implicit filters to evaluate the costs and benefits of using one or the other approach. The filters developed in chapter 4 should be tested on Eddy Viscosity methods with adaptive viscosity on both compressible and incompressible flows. Finally, the methodology developed in chapter 5 can capture shocks. There is a vast range of situations where this methodology should be tested in combination with shock/instability detectors.

References

[1] F. X. Trias, A. Gorobets, M. H. Silvis, R. W.C.P. Verstappen, and A. Oliva. A new subgrid characteristic length for turbulence simulations on anisotropic grids. *Physics of Fluids*, 29(11), 2017.

[2] A. Jameson. Formulation of kinetic energy preserving conservative schemes for gas dynamics and direct numerical simulation of one-dimensional viscous compressible flow in a shock tube using entropy and kinetic energy preserving schemes. *Journal of Scientific Computing*, 34:188–208, 2008.

[3] W. Rozema, J. C. Kok, R.W.C.P. Verstappen, and A.E.P. Veldman. A symmetry-preserving discretisation and regularisation model for compressible flow with application to turbulent channel flow. *Journal of Turbulence*, 15(March 2015):386–410, 2014.